3-1-94
E-7549

Engine Materials Characterization and Damage Monitoring by Using X-Ray Technologies

George Y. Baaklini

NASA

Engine Materials Characterization and Damage Monitoring by Using X-Ray Technologies

George Y. Baaklini
Lewis Research Center
Cleveland, Ohio

Page intentionally left blank

Contents

Chapter 1

Introduction

High-temperature engine materials (e.g., ceramics, intermetallic matrix composites (IMC's), metal matrix composites (MMC's), and ceramic matrix composites (CMC's)) are being developed mainly for aeronautic propulsion components. High-temperature materials offer good oxidation resistance, low density, and high-temperature strength and operate at significantly higher temperatures than metals and superalloys. Using these composites reduces engine cooling requirements, engine weight, and consequently fuel consumption. Payoffs in engine performance and cost savings are expected. MMC's and IMC's can be used over the temperature range 800 to 1370 °C (1475 to 2500 °F). CMC's can be used over the range 1100 to 1650 °C (2000 to 3000 °F). IMC's and MMC's are targeted as compressor and turbine disk materials, whereas CMC's are targeted for extreme high-temperature applications, such as turbine vanes, blades, and disks.

Monolithic structural ceramics are limited by detrimental inherent defects (Evans et al., 1977; Evans, 1984) and by low fracture toughness, low strain tolerance, and reliability assurance (Harper, 1983; Baaklini, 1987; Structural Ceramics, 1986). In order to overcome the limitations of monolithic structural ceramics, CMC development is being pursued aggressively to improve fracture toughness and strength and to minimize sensitivity to detrimental flaws.

Limiting factors for IMC's include mismatch in fiber and matrix coefficients of thermal expansion (CTE's), analytical modeling in conjunction with composite development, and the ductility or toughness of the matrix. Limiting factors for CMC's include the fiber-matrix interface, development of high-strength and small-diameter fibers, and analytical modeling for life prediction. In addition to developing high-CTE fibers for IMC's and small-diameter, high-strength fibers for CMC's, one critical issue is to identify failure and damage mechanisms so that better modeling and life prediction can be done on these emerging composites.

Progress in the processing of high-temperature materials has not been matched by the detailed mechanical and nondestructive testing efforts that are needed to support the design of new materials and related generic components. A definite need exists for experiments that identify the failure mechanisms and follow the damage progression. Upgrading the capabilities of existing nondestructive evaluation (NDE) techniques for characterizing density variations and recognizing detrimental defects in the new material systems is also needed. Innovative experiments that monitor specimens under loading must be done before mechanical models can be fully developed.

The processing of new and innovative high-temperature materials requires concurrent development of new and innovative NDE technologies. Sanders and Baaklini (1988) demonstrated that nondestructive materials characterization and proper feedback help optimize the processing procedures. Nondestructive quality inspection where specific American Society for Testing and Materials (ASTM) standards are applied assures materials reliability. Vary (1991) suggested that new NDE standards and methodologies should mature simultaneously with advancements in materials development. Similarly, manufacturing of high-temperature generic engine components calls for simultaneous development of creative NDE techniques and for upgrading of existing NDE technologies.

The purpose of this work was to develop and apply x-ray attenuation measurement systems that are capable of characterizing density variations and of monitoring damage accumulation and failure mechanisms in high-temperature materials and components. This work should accelerate the development of generic monolithic and composite components and provide greater understanding of related mechanical behavior.

Many researchers have evaluated monolithic ceramic coupon materials by using conventional and advanced NDE technologies, but little work has been done on high-temperature composites (Vary and Klima, 1991). Nuclear magnetic resonance imaging is a feasible NDE modality for quantifying organics in injection-molded green (unfired) ceramics (Ellingson et al., 1987a, 1989; Gopalsami et al., 1990). Automated visual examinations (Bowman and Batchelor, 1985) are routinely used to detect surface-connected anomalies in fired objects. Conventional film radiography and immersion scanning ultrasonics are methodically used to detect sizable

(>0.5 mm in diameter) surface and volume flaws in specimens and components. Flaws as small as 25 μm in diameter can be resolved by acoustic microscopy and microfocus radiography (Nikoonahad, 1987; Baaklini et al., 1986a, 1986b, 1987), by scanning laser acoustic microscopy (Roth et al., 1986, 1987), and by x-ray tomography (Yancey et al., 1990, 1991) under stringent conditions (e.g., moderate material thickness and good surface finish). Ultrasonic attenuation and velocity (Generazio, 1985; Generazio et al., 1988; Baaklini et al., 1989), acousto-ultrasonics (Kautz and Lerch, 1991; Kautz and Bhatt, 1991; Vary, 1978, 1988; Hemann and Baaklini, 1986), and backscatter ultrasonics (Goebbels, 1980) were successfully used to quantitatively characterize the microstructure and to experimentally deduce correlations between NDE parameters and the mechanical and physical properties of the materials.

NDE of emerging subscale engine components is limited. The Ceramic Application in Turbine Engines Programs (Byrd et al., 1981; Helms et al., 1984) included NDE applications on blades and rotors. The Advanced Gas Turbine Technology Project (AGT, 1988) and the Advanced Turbine Technology Applications Project (ATTAP, 1990) also included NDE applications for material processing optimization. NDE capabilities are being uncovered in high-temperature composite components as NDE programs are integrated early in the development programs. But the role of NDE is still not clearly defined.

NDE requirements and goals for high-temperature materials are reviewed and assessed in chapter 2. Chapter 2 also briefly describes the fabrication of selected high-temperature materials, concisely surveys candidate novel NDE techniques for characterizing emerging materials, and succinctly explores the role of NDE in materials development.

Chapter 3 describes the buildup of a point-scan digital radiography system and explains the objectives for building this system. It also defines the capabilities and limitations of this system for materials characterization.

In chapter 4 an extensive study of NDE capabilities and limitations for characterizing monolithic ceramic components is pursued. The work in this chapter is a step toward validating x-ray computed tomography (XCT) results by metallography, radiography, and ultrasonics. This effort extends the early effort (Helms et al., 1984; AGT, 1988) in NDE of ceramic monolithic components.

Chapter 5 defines the capabilities and limitations of XCT for characterizing MMC specimen and subscale engine components. This work provides new data and composite calibration data, helps identify fabrication-related problems, and guides geometric and stiffness modeling of composite constituents.

Proposed CMC components are not yet available, but related CMC specimens are obtainable and procurable. CMC mechanical behavior is not well understood. Chapter 6 shows how in situ x-ray monitoring, a new and unique capability, noninvasively monitors damage accumulation and failure sequences in a unidirectional silicon-carbide-fiber-reinforced, reaction-bonded silicon nitride matrix (SiC/RBSN). This work provides greater understanding of SiC/RBSN mechanical behavior and consequently helps in validating newly developing analytical models.

Chapter 7 binds, discusses, and concludes this work and highlights future research needed to advance state-of-the-art NDE technology in order to fulfill emerging technology requirements in high-temperature materials and advanced engine component development.

Chapter 2

NDE Requirements and Goals for Characterizing High-Temperature Materials

2.1 Introduction

This chapter describes the fabrication of selected high-temperature materials and related components, surveys selected nondestructive evaluation techniques, and explores the role of NDE in materials development.

2.2 Materials and Subscale Engine Components

2.2.1 Silicon Carbide Rotor

The turbine rotor was fabricated at Sohio by injection molding of sintered alpha silicon carbide material (AGT, 1988). Carbide injection molding involves plastic forming of mixtures of powder and organic additives (binders) that deform under pressure and heat into desired complex shapes (Richerson, 1982). The binders have low enough viscosity to allow the mixture to flow at specified temperatures and pressures. The viscous material is forced into a shaped tool cavity until the cavity is filled and the material has fused under pressure and temperature to produce the homogeneous part. The major problems in plastic-forming processes are removing the binder before firing and achieving high enough green density. Inadequate binder removal results in cracking, substantial shrinkage, bloating, and nonuniform densification. Hot isostatic pressing (HIP) was used to improve microstructural homogeneity. Pores in the large hub area of the rotor are the flaws that dominate failure.

2.2.2 Silicon Nitride Disks and Blade

The silicon nitride composition for the disks contained 5.8 wt% silicon dioxide (SiO_2) and 6.4 wt% (Y_2O_3). The disks were slurry-pressed (Sanders et al., 1989) under 9 MPa, dried, and then cold isostatically pressed under 414 MPa to increase the green density (appendix A). Thereafter, the disks were sintered (appendix B) at 2140 °C for 3 hr under 5-MPa N_2. Boron nitride setters separated the disks during sintering. X-ray diffractometer scans of polished disk surfaces show beta silicon nitride to be the only detectable crystalline phase.

The silicon nitride blade was injection molded and sintered by General Telephone and Electronics Laboratories (Byrd et al., 1981; Helms et al., 1984). The process routing outline is shown in appendix C.

2.2.3 Silicon-Carbide-Fiber-Reinforced Silicon Nitride

Silicon-carbide-fiber-reinforced silicon nitride composites were consolidated by hot pressing and reaction bonding. Fiber mats were prepared by winding the fiber at a specified spacing on a cylindrical mandrel, spraying polymer binders to reserve fiber spacing, and cutting the mats to required size. Matrix tapes were prepared by blending the silicon powder with a polymer binder and then rolling the mixture into tapes of specified thickness. Setting the fiber spacing and the matrix mat thicknesses controlled the fiber volume fraction of the composite. Alternating layers of silicon tape and fiber mat were stacked in a metal die and hot pressed in vacuum from 800 to 1000 °C for 1 hr at 50 to 100 MPa. Finally, the SiC/Si preforms were heat treated in nitrogen from 1000 to 1400 °C for as long as 100 hr to convert silicon to silicon nitride as the matrix material. Composite panels containing 9 to 24 percent fiber volume fraction were fabricated with typical dimensions of 125 by 50 by 2 mm. Only one eight-ply specimen was nitrided at 1350 °C in N_2 + 4% H_2 for 80 hr; all other specimens that were nitrided at 1200 °C in N_2 for 40 hr.

The reaction-bonded silicon nitride (RBSN) matrix was chosen because dimensional changes do not occur during nitridation (it is a matter of filling in the pores), making it an ideal matrix for complex-shaped components. Furthermore, the technique resulted in high-purity matrix material with good high-temperature properties and high creep resistance.

2.2.4 Silicon-Carbide-Fiber-Reinforced Titanium-Base Composites

The fabrication procedures for the SCS–6 fiber-reinforced rod and ring are schematically shown in appendix D (figs. D.1 and D.2). A bundle of SCS–6 (142 μm in diameter) filament was spirally wound with titanium ribbon; the filament bundle was then inserted in a titanium alloy C cylinder to fabricate the rod and in a slotted alloy C disk to fabricate the ring. Titanium caps were welded to each end of the cylinder and to the top of the slotted disk for sealing. The sealed cylinder and disk were consolidated by hot isostatic pressing. The consolidated composite cylinder and disk were then machined into a rod and a ring.

The fabrication procedures for the subscale integrally bladed rotor are schematically shown in figure D.3 of appendix D. Powder-coated SCS–6 fibers were transversely wound and consolidated in hard (graphite type) tooling to make the composite ring. Thereafter, the ring was inserted into a slotted disk, capped, and vacuum-hot-press (VHP) bonded. The bonded composite disk was then machined into an integrally bladed rotor.

2.3 Novel NDE Techniques

X-ray attenuation measurement and selected ultrasonic measurement are the only NDE techniques stressed in this section because of their ability to characterize the densified materials under consideration.

2.3.1 X-Ray Film Radiography and Microfocus Radiography

X rays (i.e., photons) are a form of electromagnetic radiation with wavelengths ranging from 10 to 0.0001 Å (appendix E). Roentgen discovered x rays in 1895. The energy E_e of a photon is proportional to the frequency f_e of the electromagnetic field by $E_e = hf_e$, where h is Planck's constant. The minimum wavelength λ_{min} of the x ray is given by $\lambda_{min} = c/f_e = ch/E_e = ch/eV$, where c is the velocity of light, e is the charge on the electron, and V is the voltage across the x-ray tube:

$$\lambda_{min} (\text{in angstroms}) = \frac{12\ 395}{V(\text{in volts})} \qquad (2.1)$$

X rays of different energies are emitted from an anode (fig. 2.1(a)), creating a continuous x-ray spectrum as shown in figure 2.2(a). The intensity (energy flux density in joules (or watts) per square meter) of x rays is defined as the number of photons per unit of area multiplied by their energy. The energy flux density is proportional to the tube current I, to the
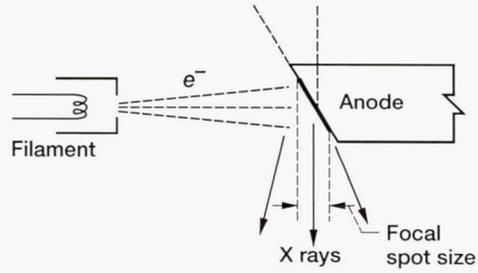
(a) Conventional tube.
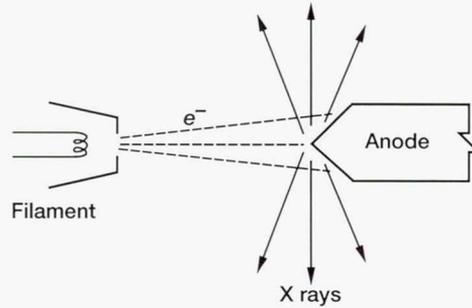
(b) Panoramic tube.
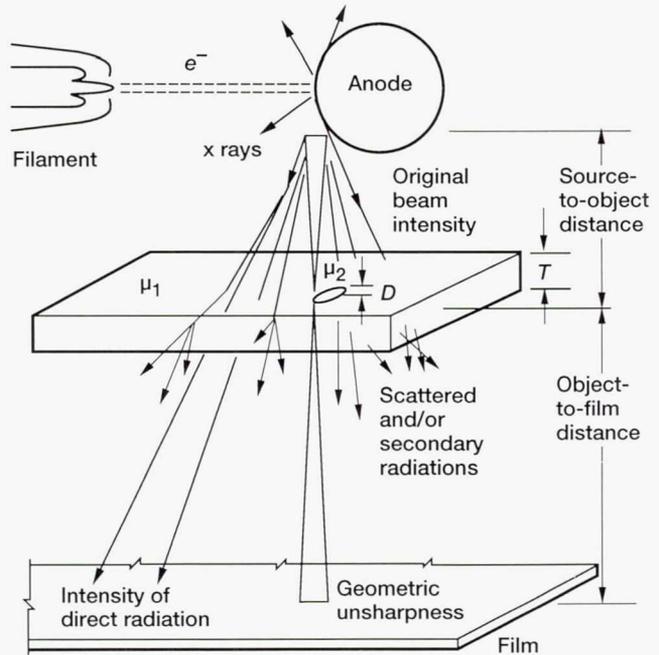
(c) Microfocus tube.

Figure 2.1.—Schematic configurations of x-ray tubes and of microfocus projection radiography (where D is the thickness of the defect, T is the thickness of the sample, μ_1 is the attenuation coefficient of the matrix, and μ_2 is the attenuation coefficient of the defect).

4

atomic number of the anode material Z, and to the square of the tube voltage V^2:

$$\psi \sim IZV^2 \qquad (2.2)$$

Figures 2.2(b) and 2.3 show the effect on x-ray intensity of the tube voltage, the tube current, the inherent filtration in the anode, and the additional filtration.

The intensity of an x-ray beam is attenuated as it interacts with matter by absorption and scattering mechanisms. The number of photons dN passing through a thin layer of matter depends on the number of incident photons N and decreases proportionally to the thickness dx of the layer and the total linear attenuation coefficient μ of the matter:

$$dN = -\mu N\, dx \qquad (2.3)$$

Dividing by N and integrating over N and x gives the exponential law of attenuation

$$N = N_0 e^{-\mu x} \qquad (2.4)$$
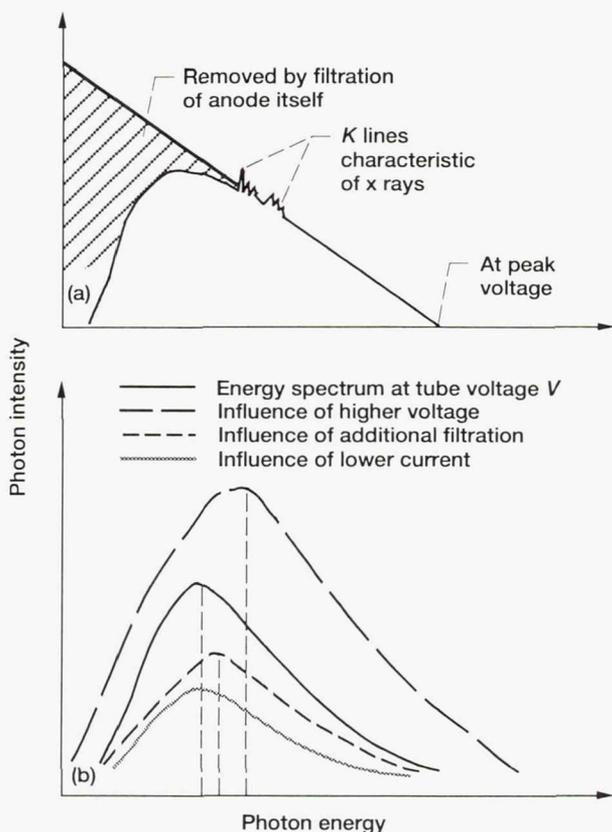
Figure 2.2.—Spectrums of x-ray energies leaving an x-ray tube.
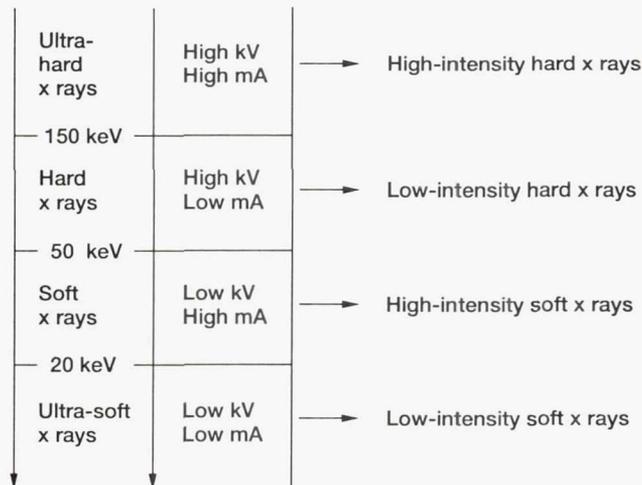
Figure 2.3.—Effects of tube potential (kV) and tube current (mA).

where N_0 is the number of incident photons, N is the number of transmitted photons, and x is the thickness of the material. In actual application a spectrum of N_0 (hf_e) exists and calls for integration over hf_e. The attenuation process is complex and includes photoelectric absorption, Rayleigh scattering, Compton scattering, and pair production as shown in figure 2.4. Detailed information on the attenuation mechanisms can be found in Halmshaw (1982). Information on linear attenuation coefficient dependency on atomic number and energy can be found in the Nondestructive Testing Handbook (Vol. 3, 1985). Briefly, the attenuation coefficient varies directly with atomic number for the Compton effect, between Z^4 and Z^5 for the photoelectric effect, and with $Z(Z+1)$ for pair production.

Linear attenuation coefficients are proportional to the material density ρ, which depends on the physical state of the material. Hence, most tables list the mass attenuation coefficient μ/ρ to eliminate the density dependence, where μ is per centimeter and ρ is in grams per cubic centimeter, making the ratio μ/ρ in square centimeters per gram. Rewriting equation (2.4) as

$$N = N_0 e^{-\mu/\rho(\rho x)} \qquad (2.5)$$

and using an equivalent attenuation law

$$N = N_0 e^{-nsx} \qquad (2.6)$$

(where n, the number of atoms per cubic centimeter, is given by $(N_A\rho)/A$, s is the total cross-sectional atomic attenuation coefficient (proportionality constant), N_A is Avogadro's number, and A is the atomic weight) shows the total mass attenuation coefficient μ/ρ to be proportional to the total photon cross section (i.e., to the sum of all the cross sections from

Photoelectric (PE) absorption effect
decreases as photon energy increases

Compton (C) scattering effect
considerable at low photon energies and
predominant at higher photon energies

Pair production (PP)
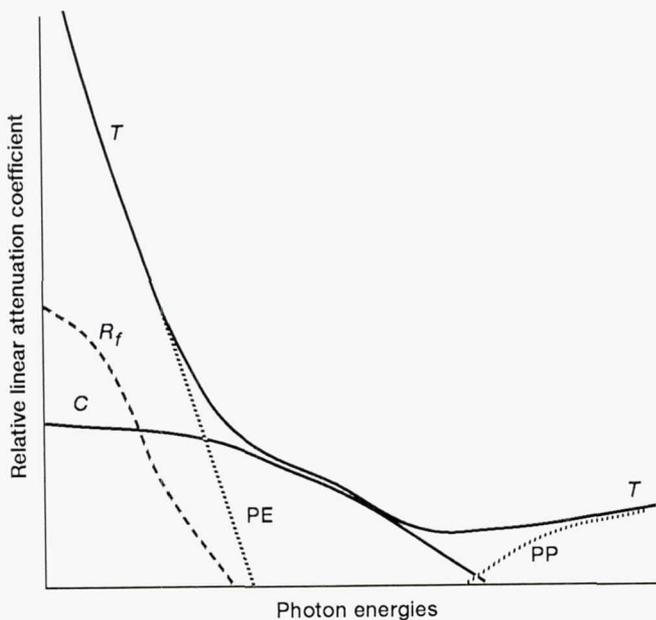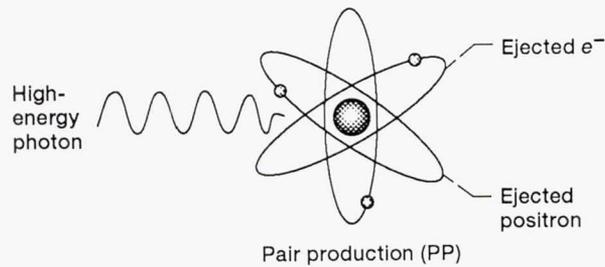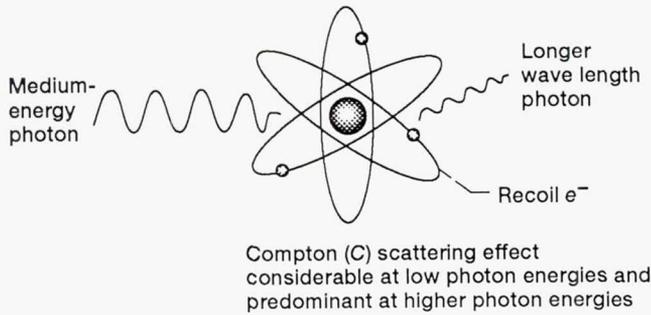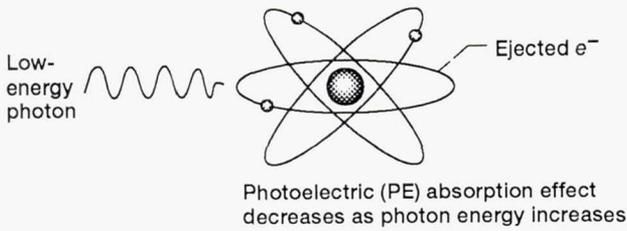
Figure 2.4.—Typical interaction of x rays with matter (where R_f is the Rayleigh scattering photon deflected in forward direction without change in energy and T is total attenuation).

the scattering and absorption mechanisms) and to Avogadro's number and to be inversely proportional to the atomic weight A:

$$\mu / \rho = \frac{N_A s}{A} \tag{2.7}$$

The total mass attenuation coefficient of a compound $(\mu/\rho)_c$ can be approximately calculated from the mass attenuation coefficients of the constituent elements μ_i/ρ_i according to their relative abundance by weight

$$(\mu / \rho)_c = \sum_i W_i (\mu_i / \rho_i) \tag{2.8}$$

where W_i is the proportion by weight of the ith constituent. For example, for SiC

$$(\mu / \rho)_{SiC} = [28.086 / (28.086 + 12.01115)](\mu / \rho)_{Si}$$

$$+[12.01115 / (28.086 + 12.01115)](\mu / \rho)_C \tag{2.9}$$

For energies above 10 keV this rule of mixtures introduces errors of less than 5 percent due to changes in the molecular, chemical, or crystalline environment of an atom (Hubbell, 1969).

Several means of detecting differentials in photon attenuation exist for x rays passing through matter. Film radiography is the most widely used technique for recording radiation as a variation in the silver deposit of an exposed and then processed film. Fluoroscopy, image intensifiers, television systems, scintillation counters, and matrix scintillator or semiconductor detectors are also used to record radiographic information.

Radiographic detectability depends on the spatial resolution and type of energy of the radiographic system and on the image contrast and its spatial resolution as recorded on the radiographic detector. In film radiography the spatial resolution is a function of the film graininess, which governs signal-to-noise ratio, and of the geometric resolution R given by

$$R \geq \frac{U}{M} \tag{2.10}$$

where M is the x-ray image magnification given by $M = (b + a)/a$, where a is the source-to-object distance and b is the object-to-detector distance (fig. 2.1(c)). The geometric unsharpness U is given by

$$U = S\left(\frac{b}{a}\right) \tag{2.11}$$

where S is the focal spot size. It follows that R can be given as

$$R = S\left(\frac{b}{a+b}\right) \tag{2.12}$$

The radiographic image contrast (Parish, 1979) is given by

$$C = \frac{0.43(\mu_1 - \mu_2)(\Delta X)G}{1 + N_s / N_p} \tag{2.13}$$

where μ_1 is the total attenuation coefficient of the matrix, μ_2 is the total attenuation coefficient of the defect, ΔX is the dimension of the defect in the direction of the x-ray beam, G is the film gradient, N_s is the number of scattered photons, and N_p is the number of primary photons (direct image-forming radiation).

In conventional radiography S is on the order of 400 μm to 3 mm and $a \gg b$. In microfocus radiography S is on the order of 10 to 50 μm and $b > a$. This implies that scattered radiation is minimal in microfocus radiography and sizable in conventional radiography. Furthermore, large S in conventional radiography limits projection capabilities because geometric unsharpness deteriorates (eq. (2.11)). As shown in equation (2.13), a smaller ratio of N_s/N_p and a larger difference $\Delta\mu = \mu_1 - \mu_2$ are needed to improve the image contrast. Microfocus radiography maximizes detectability because in general the lower atomic number of the anode increases the contrast by presenting greater differences in $\Delta\mu$ (Radiological Health Handbook, 1970), because it permits projection, which prevents scattered radiation from fogging the image, and because it has a small focal spot size.

2.3.2 Digital X Radiography

Reviews of digital radiography are available in the literature (e.g., Riederer, 1985; Arnold et al., 1981, 1982; Smathers and Brody, 1985; and Kereiakes et al., 1986). Most of the digital radiography research and applications have been in the medical community, even though digital radiography has been evolving since the late 1970's. Digital radiography has profited from the digital techniques that were developed for computerized x-ray tomography applications after its invention by Hounsfield (1973).

In digital radiography two-dimensional projection images are digitally acquired and recorded with various detector technologies and related readout procedures. Digital radiography systems include point-scan digital radiography (PSDR), line-scan digital radiography (LSDR), and area-scan digital radiography (ASDR) (fig. 2.5). The first digital radiographs were digitized x-ray films that were read by using backlighting and digitizing cameras or videocons or by using densitometric scanners. Regardless of the detector technologies and the modes of conversion from analog to digital
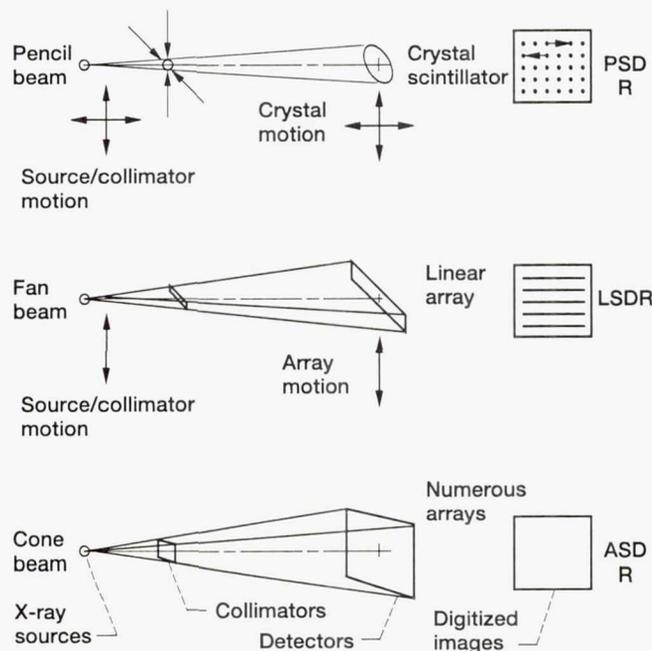
Figure 2.5.—Digital radiographic modalities (where PSDR is point-scan digital radiography, LSDR is line-scan digital radiography, and ASDR is area-scan digital radiography).

format, digital acquisitions are ideal for mass image storage (i.e., optical disks), dual energy subtraction, temporal subtraction, compensation in wide dynamic ranges, energy-selective imaging, and other functions including spatial and frequency filtering and contrast stretching. Digital image and digital signal processing can enhance and improve x-ray display capabilities (Oppenheim and Schafer, 1975; Gonzalez and Wintz, 1977; Pratt, 1978; Capellini et al., 1978, 1980; Simon et al., 1980; Macovsky, 1983).

Many critical factors that affect digital radiographic systems should be considered before any advanced digital image processing can be applied. These factors include the x-ray spectrum, energy, and intensity of the source; the quantum detection efficiency of the source-detector system; the signal-to-noise ratio (Tapiovaara and Wagner, 1985); the spatial resolution, the integration time depending on the source-detector-scanning designs, and the scatter reduction at the detector (Pfeiler et al., 1985; Macovsky, 1983).

Digital radiography images are composed of square pixels. Each pixel has coordinates and an integer value representing its brightness or photon counts. An eight-bit pixel brightness ranges from 0 to 255. A typical 1024-by-1024 image consists of approximately a million pixels. Digitization of a 14- by 17-in. continuous radiographic image film requires a digital radiographic image consisting of 4 million pixels. Pixel size and field of view limit image resolution because the highest spatial frequency that can be imaged is one cycle per two pixels according to the Nyquist criterion. Combining projection radiography (higher magnification) with a large matrix detector improves the spatial resolution region of interest. Digital

radiographic images are not inherently contrast limited because brightness levels can be digitized virtually indefinitely (e.g., 256, 512, 1024, etc.). But display contrast sensitivity is limited as in film radiography by the video display type, the subject contrast C_{sub} (ideal contrast neglecting scatter), and the scattered radiation (Rzeszotarski and Sones, 1989):

$$C_{res} = C_{sub}\left(\frac{1}{1+\text{SPR}}\right) \qquad (2.14)$$

where SPR is the ratio of the scattered radiation to the primary radiation and C_{sub} equals $\mu\Delta X$ if $\mu\Delta X \ll 1$. Equation (2.14) is a general form of the contrast equation (2.13).

The signal-to-noise ratio and contrast are interdependent

$$\text{SNR} = \frac{KC_{res}}{\sigma(x)} \qquad (2.15)$$

where K is a proportionality constant (e.g., K is $0.43G$ in eq. (2.13)), KC_{res} is the radiographic contrast of a specific feature to be imaged, and $\sigma(x)$ is the quantum noise. The Poisson distribution $\sigma(x)$ is a function of the quantum efficiency of the detector or screen n, the number of transmitted photons, and the sampling area A_s:

$$\sigma(x) = \frac{K}{\sqrt{nA_sN}} \qquad (2.16)$$

where nA_sN, a dimensionless quantity, is the effective number of photons absorbed in the sampling area A_s.

The detection quantum efficiency (DQE) is a measure of the efficiency of information transfer and is given by

$$\text{DQE} = \left(\frac{\text{SNR}}{\text{SNR}_{id}}\right)^2 \qquad (2.17)$$

where SNR_{id} is the SNR of the primary radiation N_p. Overall DQE is a product of all the components of DQE and is always between 0 and 1. The SNR from equation (2.15) can now be written as

$$\text{SNR} = C_{sub}\sqrt{N_{eff}A_s} \qquad (2.18)$$

where the effective value of the primary photons N_{eff} is the product of DQE and N_p.

PSDR has excellent scatter-elimination capabilities, low electronic noise, and high quantum detection efficiency. The beam geometry dictates spatial resolution and time of exposure. A major disadvantage of PSDR is its inefficient use of the x-ray tube flux. LSDR exhibits good scatter removal

capabilities, low electronic noise, wide dynamic range, and high contrast detectability. The disadvantages of LSDR are inefficient use of radiation and variations in sensitivity between detectors. ASDR is efficient in using the full x-ray beam and allows near-real-time acquisition. ASDR resolution is dictated by the particular readout technology used, and its contrast sensitivity is dictated by the material detector. The principal disadvantage of ASDR is its poor scatter removal capabilities.

2.3.3 X-ray Computed Tomography

Equation (2.4) can be rewritten by applying the logarithm to the ratio N_0/N as follows:

$$\ln(N_0/N) = \mu(E_e)X_m \qquad (2.19)$$

For inhomogeneous materials equation (2.19) becomes the line integral along the x-ray beam that is the sum of the linear attenuation coefficients,

$$\ln(N_0/N) = \int_0^x \mu(x,E_e)dx \qquad (2.20)$$

This line integral is the foundation of x-ray computed tomography (XCT). Sums of line integrals for a systematic series of angles and positions make up the raw XCT data. Most XCT scanners use polychromatic radiation that can be treated as a large number of monochromatic beams (Pullan et al., 1981), each with a different energy. Then, the number of photons exiting a sample is given by

$$N(X,E_e) = \int_0^{E_{max}}\left[N_0(X,E_e)e^{-\int_0^x \mu(X,E_e)dx}\right]dE \qquad (2.21)$$

where E_{max} is the maximum tube energy. However, this polychromatic radiation introduces the following complications: (1) "beam hardening," whereby the high-energy photons are less attenuated than the low-energy photons as they pass through the sample, increasing the mean beam energy in an unpredictable manner; and (2) inaccurate transmission measurement readings by XCT detectors that are in general proportional to the number of photons and their energy. Once beam-hardening corrections are made, the linear attenuation coefficient is computed on the basis of an effective transmission measurement where μ is assumed to be constant within each voxel (a three-dimensional pixel).

Cormack (1963, 1964) demonstrated the importance in x-ray tomography of finding a real function in a finite region of a plane by defining its line integrals along all straight lines intersecting the region, similar to the original mathematical problem of reconstructing a two-dimensional function from

its projected line integrals (Radon, 1917). Similarly, Hounsfield (1973) obtained the solution to an unknown x-ray attenuation coefficient in two-dimensional domains by solving a set of simultaneous equations with the assumption that the pixel value contains a percentage of the attenuated radiation. This method is depicted in the iterative reconstruction of figure 2.6. The two scientists shared the Nobel prize in 1979 for physiology and medicine. The line integral approach is valid in x-ray transmission tomography where the wavelength of the x-ray beam is much smaller than the size of the feature to be imaged, hence eliminating any x-ray diffraction complications (Azevedo, 1988).

In x-ray computed tomography, information regarding the innermost regions of an opaque object is provided by measuring the x-ray energy transmitted through that object and reconstructing individual cross sections of it. Many simplifying assumptions are used in the reconstruction processes (Herman, 1981). These reconstruction processes (e.g., the ones depicted schematically in figs. 2.6 and2.7) permit solving for the CT number for each voxel within the object given the x-ray transmission attenuation values along a large number of lines in the cross section. The CT number is related to the linear attenuation coefficient of the material,

$$CT \text{ number} = \frac{\mu_{material} - \mu_{water}}{\mu_{water}} \times 1000 \qquad (2.22)$$

A CT number of zero corresponds to water, and a CT number of -1000 corresponds to $\mu = 0$ and is taken as identical to that of air. The precision of the CT number identifies the potential of the CT value for a single voxel to represent a homogeneous object made from the exact same material. The accuracy of the CT number identifies how close the measured CT numbers are to the true value, which is the total mass attenuation coefficient of the voxel converted into a CT number. As discussed earlier in this chapter the total mass attenuation coefficient varies with the effective x-ray beam energy. This effective energy depends on the tube potential settings, on the energy spectrum of the polychromatic source, and on the attenuating materials. Consequently, in order to use CT numbers for precise and accurate representation of the total mass attenuation coefficient, phantoms (Kropas et al., 1991) that contain the same chemical elements as the material under evaluation will be used to calibrate the CT scanners.

Reconstruction algorithms are classified in two major categories: the transform algorithms, which include convolution methods, and the series expansion algorithms. Filtered backprojection using a transform algorithm is the most commonly used method. The steps are to measure the projections of $f(x,y)$, to Fourier transform them to obtain $F(u,v)$ in the frequency domain, to convolve with a weighting function, and to inverse Fourier transform to reconstruct the object. Detailed examples of the backprojection algorithm for a parallel beam, an equiangular fan beam, and an equispaced fan

Transmission measurements

Iterative reconstruction

Simple backprojection

Original   Convolution within space domain   Filtered profile

Filtered backprojection
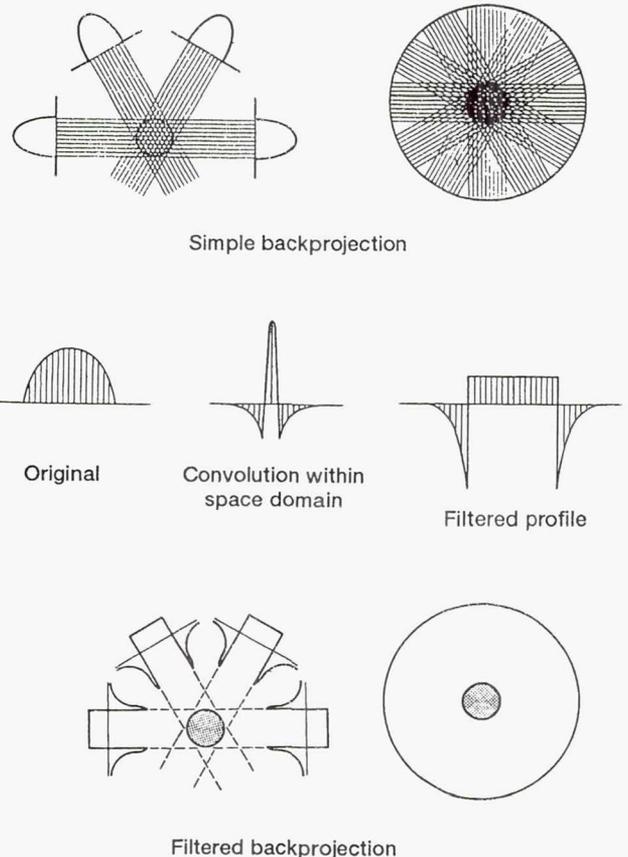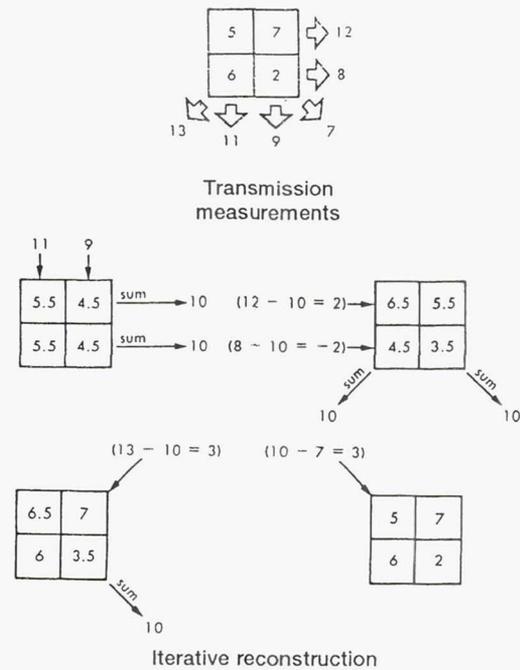
Figure 2.6.—Iterative reconstruction and backprojection representations in x-ray computed tomography. (From Zatz, 1981).

Fan beam projections
in space domain

Parallel projections
in space domain

©1983 IEEE

Via Fourier transform of
projections P_1 and P_2

Frequency domain

A pixel displayed
represents a
voxel acquired

Via inverse Fourier transform

Space domain
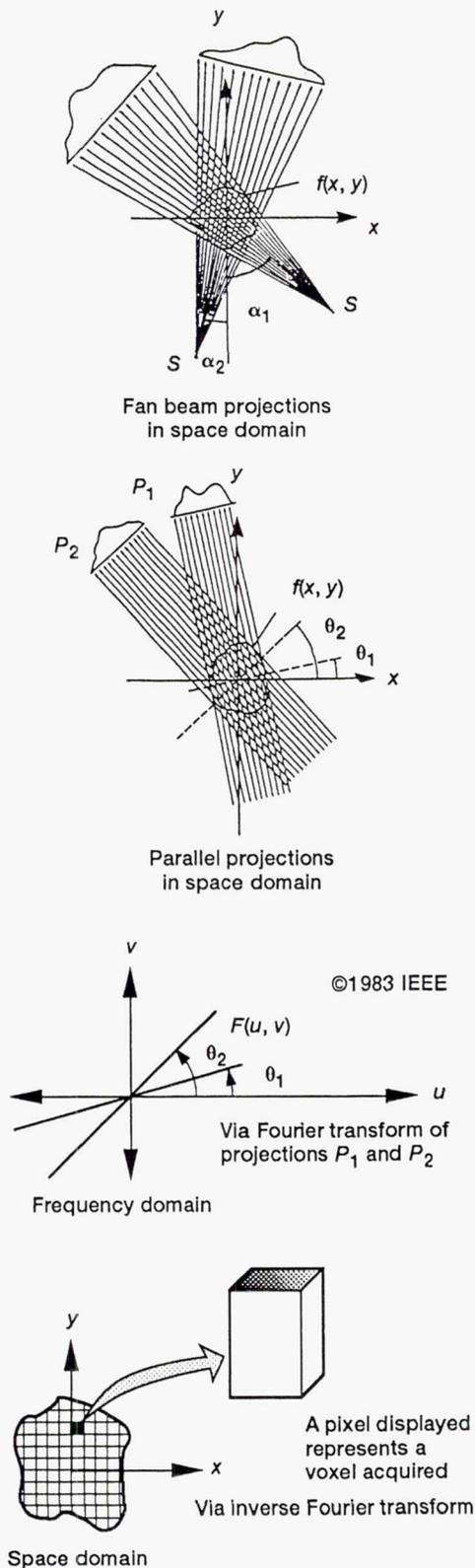
Figure 2.7.—Fourier transform of projections constructing Fourier transform of object that can be inverse Fourier transformed to reconstruct object. (Modified from Kak and Slaney, 1988).

beam are treated in Kak and Slaney (1988). Series expansion algorithms are slower than transform methods because they converge too slowly, and the availability of fast array processors makes backprojection transform much more attractive.

All algorithms have artifacts (Joseph, 1981; Azevedo, 1988) such as point spread effect, streaking, and edge enhancement (density distortion at sharp edges). Artifacts in CT are numerous and can be due to the geometry of the scanner, the nonlinearity of x-ray measurements, scatter, beam hardening, the partial volume effect, aliasing, and insufficient angular sampling. Combined with image quality limitations (Zatz, 1981) due to noise and with insufficient spatial and contrast resolution, image artifacts require a more detailed examination of the capabilities and limitations of each specific CT system relative to specific material and objects.

Extensive reviews of XCT are available in the literature (e.g., entire issues of technical journals in IEEE Transactions on nuclear medicine and medical imaging during the late 1970's and early 1980's; Newton and Potts, 1987; Kak and Slaney, 1988). Development of industrial versus medical XCT systems has been advanced by Scientific Measurement Systems Inc., Bio-Imaging Co., Innovative Imaging Systems Inc., Advanced Research and Applications Corporation, and General Electric. Considerable research effort has been mounted to apply these CT systems in characterizing advanced ceramic materials (Sawicka et al., 1986, 1987; Ellingson et al., 1987b, 1988; Yancey et al., 1990, 1991; London et al., 1990; Kinney et al., 1990, 1991). Chapters 4 and 5 will present new data on the capabilities and limitations of a particular XCT system for characterizing ceramic and metal matrix composite components.

Medical XCT scanners have evolved into four generations or types depending on the detector-source configurations. In the first generation the source and a single detector translate and rotate, in the second generation the source and a linear array detector translate and rotate, in the third generation the source and the fan beam array detector rotate, and in the fourth generation the source rotates with an encircling fixed 360° detector. For research and industrial application the source and the detector are usually fixed and the object holder translates and rotates. The system described in chapters 4 and 5 is schematically presented in figure 2.8, and a CT slice is shown depicting the CT number variations within a composite object. The magnification is on the order of 1.6 for all the scans in chapters 4 and 5. The effective spatial resolution for the system is 250 μm.

2.3.4 Ultrasonics

The emphasis in this section is on acoustic microscopy. Acoustic microscopy is a pulse-echo ultrasonic immersion technique that uses focused transducers (Lemons and Quate, 1979; Nikoonahad, 1987; Khuri-Yakub et al., 1985). The sound is focused by using curved piezoelectric material or ultrasonic lenses (e.g., a plano-concave lens glued to the

• Object translates-rotates until 180° is covered.
• Approximately 2X magnification.

Fan beam XCT

Display of reconstructed slice
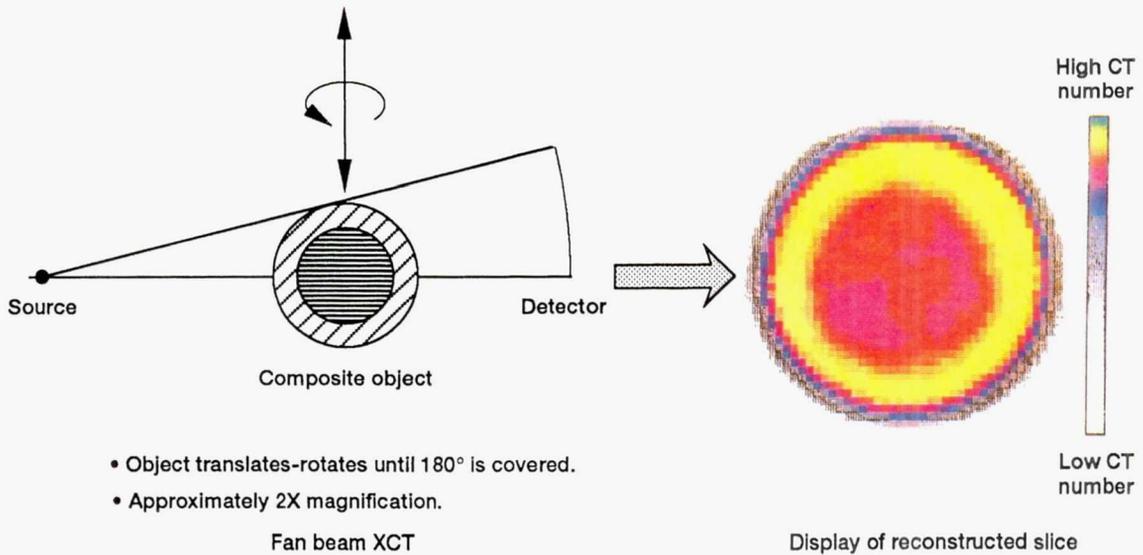
Figure 2.8.—Schematic of laminography/dual-energy scanning geometry and display of resulting CT slice.

piezoelectric crystal or a biconcave lens attached to the front of the transducer (Birks et al., 1991).

The lens concentrates the ultrasonic beam energy, and the focal plane is set within the sample to reduce the effect of surface conditions on the reflected signal. The major advantage of using focused transducers is the ability to focus at different depths in the sample by adjusting the distance between the transducer-lens and the surface of the sample. The reflected ultrasonic pulse is time gated, and changes in signal amplitude form an image of the sample volume at a preselected depth (fig. 2.9). The image is acquired in scanning acoustic microscopy (SAM) like a conventional ultrasonic C-scan that uses precision mechanical scans.

The signal amplitude will be affected by density variations, cracks, voids (Klima et al., 1986), impurities, and delaminations in laminated composite structures (Khuri-Yakub et al., 1985). Typically, a 50-MHz system can detect 20-μm voids located 1 mm below the surface in monolithic silicon nitride ceramics (Klima et al., 1986).

The system shown in figure 2.9 is used to corroborate the presence of density variations found by x-ray computed tomography (see chapter 4).

2.4 NDE Role in Materials Development and Characterization

Brittle fracture in monolithic ceramics is dominated by minute defects and microstructural artifacts. Composite fracture is dominated by fiber strength and fiber-matrix bond strength. The role of NDE in characterizing densified monolithic ceramics differs greatly from its role in characterizing


(a) System.

(b) Lens-specimen configuration.
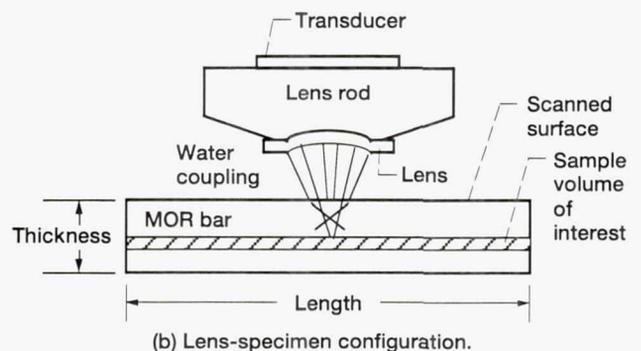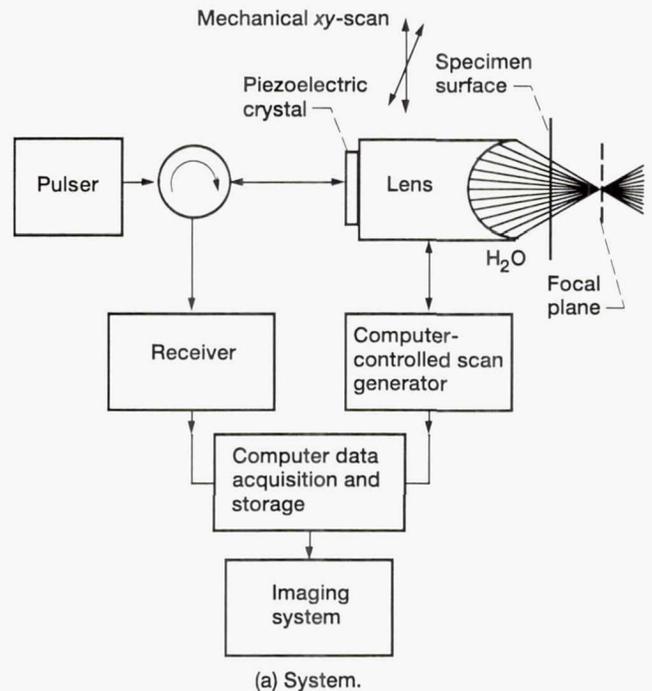
Figure 2.9.—Scanning acoustic microscopy.

11

densified metal and ceramic matrix composites. The NDE varies from defect detection and density characterization in monolithics to noninvasive failure monitoring and characterization of constituent integrity in composites.

2.4.1 Monolithic Ceramics

The strength and toughness of monolithic ceramics are degraded by the presence of minute defects (Evans, 1984; Singh, 1988). Thus, the principal role of NDE is to detect and size minute flaws, 10 to 100 µm in size (e.g., cracks, voids, high-density impurities, hard and soft agglomerates, and large grains (Klima et al., 1986; Sanders and Baaklini, 1988; Sanders et al., 1989)). It is essential to characterize the milieu of these discrete flaws because it is the surrounding material that hinders or facilitates crack growth and fracture. Subtle variations in density and in phase composition may degrade material properties (Rice et al., 1977; Nishida, 1983; McCauley, 1987).

In materials development and characterization the NDE of monolithics is well established in the green state and in the densified state. The following NDE methods are applicable to green-state bodies: nuclear magnetic resonance to measure the porosity and distribution of binders (Ackerman et al. 1987), film radiography to study green density uniformity and its effect on sintered bodies (Sanders and Baaklini, 1988) and to evaluate the reliability of flaw detection (Baaklini and Roth, 1986a), x-ray computed tomography to study density gradients (Ellingson et al., 1987a,b; and Friedman et al., 1987), and ultrasonic velocity to evaluate density changes. The following NDE methods are applicable to densified-state bodies: gamma-ray computed tomography (Sawicka and Palmer, 1986; Sawicka and Ellingson, 1987), ultrasonics (Iwasaki and Isumi, 1981; Klima et al., 1981; Khuri-Yakub et al., 1980, 1982; Tittman et al., 1980; Generazio, 1985; Generazio et al., 1988), scanning laser acoustic microscopy (Kessler and Yuhas, 1978; Yuhas et al., 1979; Roth et al., 1986), photoacoustic microscopy (Rosencwaig, 1982; Khandelwal, 1987), and x-radiography and x-tomography (Feldkamp and Jesion, 1986; Baaklini et al., 1986b; Kress and Feldkamp, 1983). These NDE techniques have demonstrated applicability with certain limitations to flaw detection and to density interrogation in the coupon type of monolithic ceramic samples.

As discussed in chapter 1, the NDE of emerging subscale engine components is limited. The NDE techniques that worked well in coupon samples must be modified for a successful transfer into the component manufacturing and testing areas. Imaging modalities with quantitative assessment capabilities will be required to expose global variations in density, in chemical composition, and in flaw population. Chapter 4 establishes the capabilities and limitations of x-ray computed tomography as it applies to monolithic ceramic components.

2.4.2 Composites

The NDE of high-temperature composites is maturing as researchers learn how to overcome difficult inspection problems. These NDE problems include characterization of matrix anomalies, fiber-matrix interfaces, and fiber architecture peculiarities.

In CMC's the matrix contains randomly distributed flaws. These flaws initiate microcracks that propagate and coalesce to form macrocracks. These cracks can be rendered benign if they are bridged. Bridging occurs if the fiber-matrix interface is weak enough to deflect the cracks and is simultaneously strong enough for load transfer from matrix to fibers. An optimized fiber-matrix interface would effectively increase the composite's toughness and ultimate strength. Ceramic matrices are usually porous, and this porosity permits fiber degradation particularly at high temperatures in an oxidizing environment.

Multiaxial fiber reinforcement by using two- and three-dimensional weaves and braiding strengthens the composite in the principal directions and makes it relatively easy to fabricate complex-shaped composites. Braiding and weaving prevent delaminations. But poor matrix material infiltration in two- and three-dimensional preforms can result in density variations, poor densification, and thus a lower critical matrix cracking stress.

The mechanical behavior, damage accumulation, and fracture in CMC's must be better understood to establish appropriate objectives for NDE. Models for initiation of matrix cracks, stiffness degradation, and load redistribution need to be developed. On-line NDE is needed to help improve processing and to help optimize interfaces through proper feedback. Quality-control NDE is required to characterize and assure the reliability of subscale components as they become available. Noninvasive monitoring of damage accumulation and failure sequences in loaded composites is urgently needed to provide greater understanding of composite mechanical behavior. Chapter 6 describes an in situ x-ray material testing system capable of visualizing damage accumulation and the failure sequence in CMC tensile specimens under load.

Aerospace engine companies are making MMC subscale engine components concurrently with material development and optimization because these emerging material systems require considerable improvement and innovation in design and manufacturing technologies. Building a 21st century civil propulsion system can be time consuming especially because of stringent economical and environmental constraints. Chapter 5 demonstrates the role of NDE in guiding the development of emerging high-temperature composite components.

Chapter 3
Point-Scan Digital Radiography

3.1 Introduction

This chapter describes the development of a point-scan digital radiography system mainly to characterize density variations in monolithic ceramic materials and possibly to identify composite constituents in ceramic matrix composite materials. The objective is the development of a high-resolution, high-contrast digital radiography system. The resolution is controlled by selecting appropriate source and detector microcollimators (100 μm in diameter). The contrast is dictated by the beam intensity for photon counting statistics, by the energy spectrum of the x-ray source, by the detection quantum efficiency of the detector, and by the subject contrast.

If this system proves viable for characterizing ceramic matrix composites, it can be upgraded to handle in situ x-ray monitoring of these composites under tensile loading. Further, a comparative analysis with an in situ film radiographic technique (chapter 6) can be established. The capabilities and limitations of the system are discussed.

3.2 System Buildup

The point-scan digital radiography (PSDR) system consists of an x-ray generator/controller,[1] an x-ray tube,[2] an x-ray detector,[3] x-ray source and detector collimators, a source collimator positioner,[4] sample and detector positioning stages and controllers,[5] a photon counter,[6] a voltage generator for the detector, a digital multimeter and an oscilloscope, a Microvax II[7] with general-purpose interface bus (GPIB)

capabilities, a VT 340 terminal, and an image display monitor. Figure 3.1 shows the digital radiographic workstation and the x-ray generator/controller, which is labeled "low energy." Figure 3.2 is a block diagram of the system. Figures 3.3 and 3.4 highlight the major system components.

The x-ray generator/controller can produce continuously variable x-ray intensities in the range 10 to 50 kV at tube currents from 1 to 50 mA. Full-wave-rectified operation rates the high-voltage transformer at 50 kV and 50 mA maximum. The x-ray tube has a copper anode that limits the tube power to 2 kW. The focal spot size at the anode is 1×10 mm^2 and the filtration is 0.4-mm beryllium.

The collimators are 100 μm in diameter. The resulting collimation is always 100 μm or less because the source collimator is aligned with the detector collimator. The source collimator is positioned by using a motorized line-centering mount that is equipped with two direct-current Motor Mike[8] drives and that contains the bushing collimator mount. The detector collimator is fixed at the front end of the detector and is positioned by aligning the detector package.

The detector contains a 1-mm-thick, 2.54-cm-diameter, thalium-activated sodium iodide (NaI (Tl)) crystal, a 125-μm beryllium window, a voltage divider, a low-noise photomultiplier tube, and a solid-state preamplifier. The detector signal offers capability for pulse counting (if connected to a photon counter) and for pulse amplitude and energy analysis (if connected to a multichannel analyzer). The crystal light conversion efficiency is 10 times that of $Bi_4Ge_3O_{12}$, four times that of cadmium tungstate ($CdWO_4$), and twice that of cesium iodide (CsI(Tl)). The crystal primary decay is 0.23 μsec, which is comparable to that of $Bi_4Ge_3O_{12}$, 20 times faster than that of $CdWO_4$, and 4 times faster than that of CsI(Tl). The crystal scintillator is hygroscopic and has a relatively low afterglow. At the operating energy the 1-mm-thick crystal has 100-percent absorption efficiency. The use of a 125-μm beryllium radiation entrance window provides 100-percent transmission above 10 keV. This detector allows substantial accuracy at low count rates and produces one

[1]XDR–5 by General Electic.
[2]AEG Corporation electronic component, Somerville, NJ.
[3]Bicron Corporation, Newbury, OH.
[4]Oriel Corporation, Stratford, CT.
[5]Klinger Scientific, Richmond Hill, NY.
[6] John Fluke Mfg. Co., Inc., Everett, WA.
[7]Digital Equipment Corporation.

[8]Trademark of Oriel Corp., Stratford, CN.
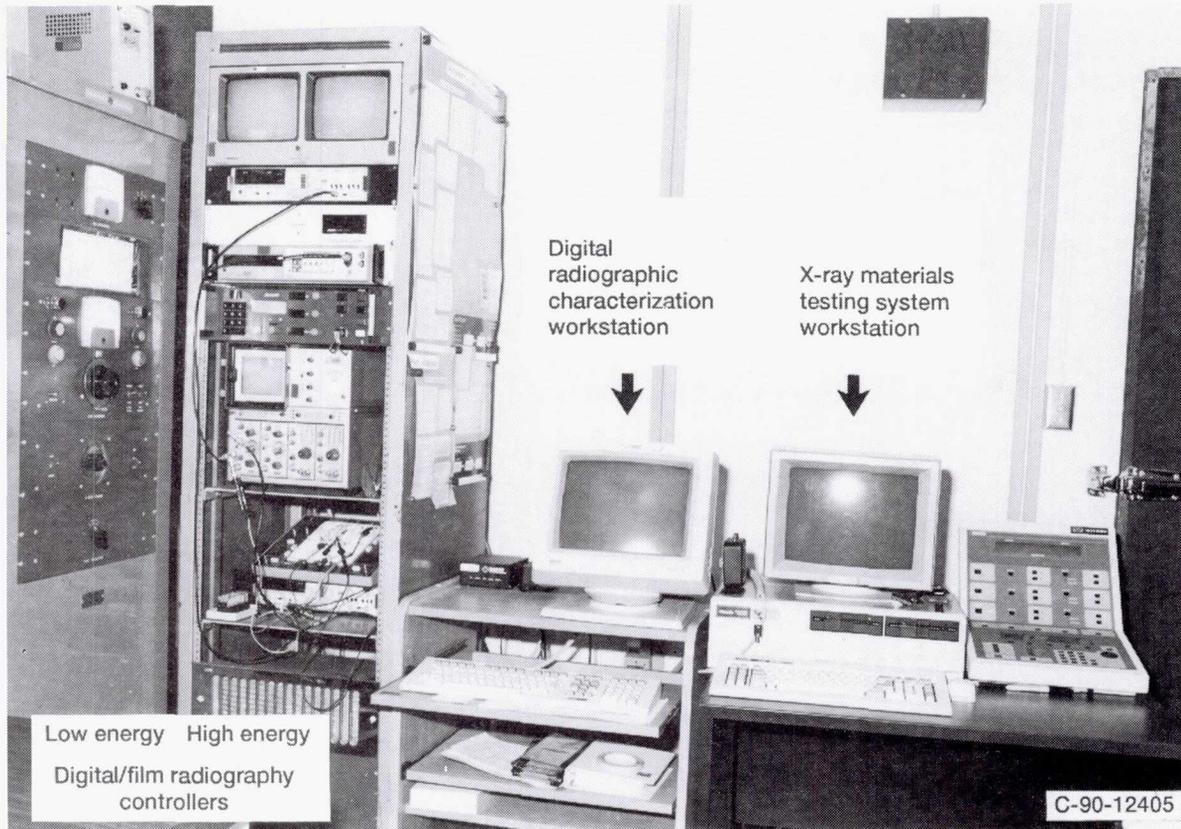
Figure 3.1.—Digital and film radiography control room.
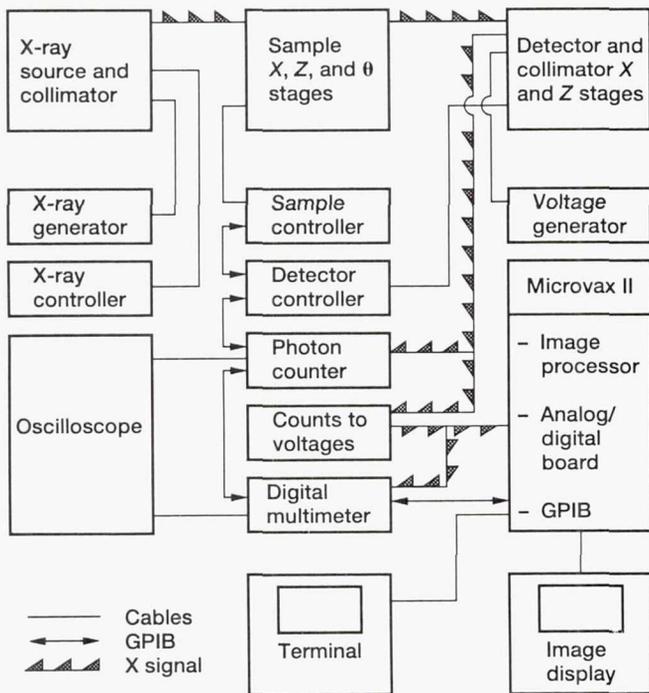
Figure 3.2.—Block diagram of point-scan digital radiographic system.

electric output pulse for every photon absorbed. Bellian and Dayton (1974) noted that the energy required to produce a photon of usable light in the NaI(Tl) crystal is in the range 40 to 50 eV.

The scintillation crystal absorbs the transmitted photons and subsequently excites the fluorescent materials. The deexcitation of the fluorescent materials from a high-energy state results in the emission of light photons. In the photomultiplier tube these light photons are collected and converted to electric pulses to be counted and analyzed.

The photon counter time gate is set to 0.1 sec. The photon count is always gated at 0.1 sec multiplied by 10 to give the count displayed per second. The trigger level is chosen by monitoring the electrical pulses with an oscilloscope and changing the trigger level control on the basis of a digital readout from a voltmeter connected to the rear panel of the counter.

The sample position stages have 0.1-μm step size capability in the horizontal and vertical directions and a rotation step size of 0.5° around the vertical axis. The detector positioning stages have 10-μm step size capability in the horizontal direction and 1-μm step size capability in the vertical direction. The stages are controlled through an IEEE–488 interface (also known as GPIB) by using programmable stepper motor controllers that "listen and talk." The source-to-object (sample) distance is 26 cm, and the source-to-detector distance is 26 cm unless otherwise stated.
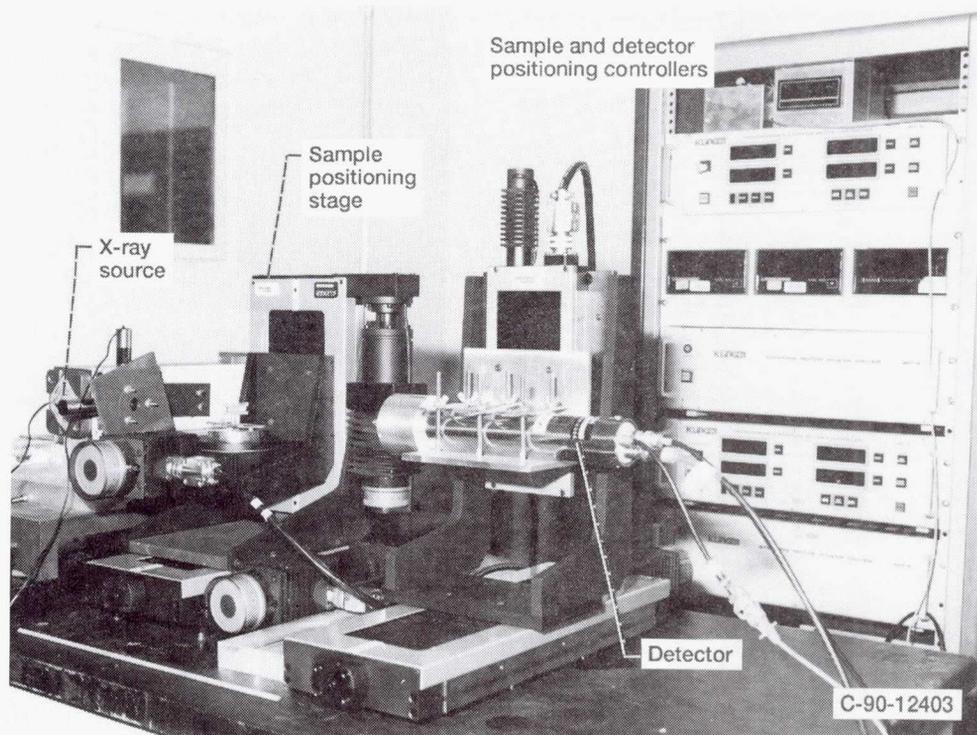
Figure 3.3.—Point-scan digital radiography characterization system.
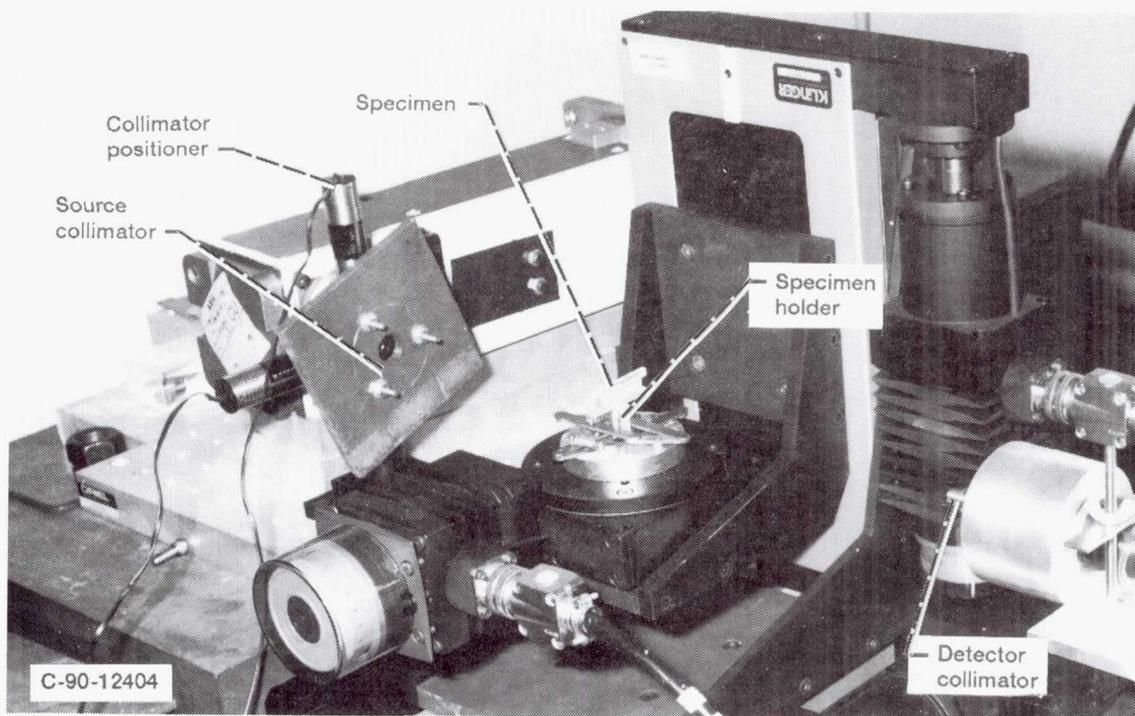
Figure 3.4.—Close up of point-scan digital radiography characterization system.

During the preprogrammed computer-controlled scanning the x-ray source and the detector are fixed and are on for the entire scan time, and the sample translates in the horizontal and vertical directions. X rays pass through the sample as it traverses in a horizontal direction, line after line, stopping after every step long enough for data acquisition and storage until the end of the scan. The data are then averaged, scaled from 0 to 255, displayed, contrast stretched, and color coded.

The x-ray beam profile of the collimated copper tube (fig. 3.5) is the result of keeping the source stationary and translating the collimated detector in the horizontal and vertical directions. The location of the global maximum count is identified and the detector is then fixed at the optimized location for digital data acquisition. Figure 3.6 shows the beam stability over a 15-hr span. Figure 3.6(a) displays photon counts versus time where data are acquired every 20 sec. These data show that the x-ray beam reaches stability approximately 1 hr after startup. Startup is defined as the start of monitoring after 1hr of tube and system warmup. Figure 3.6(b) shows photon occurrences versus photon counts, and figure 3.6(c) shows observations versus photon counts where the span is one standard deviation wide.

The copper tube bimodal profile was unexpected. In general the x-ray tube profile looks like the microfocus tube profile shown in figure 3.7. The bimodal profile may be due to the copper tube filament design or to a defective filament. The bimodal profile did not affect the experiment because of collimation, at the source and detector, respectively. The copper anode was chosen because of its energy spectrum, where photons and characteristic x rays are predominant in the low-kilo-electron-volt region. This predominance is required by

the contrast equation (2.14), where the difference in total mass attenuation coefficient controls the subject contrast C_{sub}. The ratio of scattered to primary radiation in this setup is optimum because of the microcollimation used. It is evident from figure 3.8 that the only available energy window open for differentiating among silicon carbide (SiC), silicon nitride (Si_3N_4), and air is in the 10- to 20-keV region. Figure 3.9 indicates that a higher energy is needed for thicker specimens to obtain a μx between 1 and 2. A μx between 1 and 2 assures an optimum energy (Gardner and Ely, 1967) and thus minimizes errors due to statistical counting rate fluctuations and instrumentation characteristics. The data shown in figures 3.8 to 3.11 and listed in tables E.1 and E.2 were calculated by extracting the total mass attenuation coefficients from Hubbell (1982) and using densities of 3.16, 3.21, 5.12, 5.8, 6.0, and 19.3 g/cm^3 for Si_3N_4, SiC, titanium aluminide (Ti_3Al), iron aluminide (FeAl), nickel aluminide (NiAl), and tungsten, respectively.

Figure 3.10 shows photon attenuation versus material SiC, Si_3N_4, and Ti_3Al. These values were computed by using equation (2.5) at 40, 50, 60, 80, and 100 keV. Figure 3.11(a) shows the photon attenuation versus photon energy at a specified thickness of 0.5 cm, and figure 3.11(b) shows the attenuation of photons as a function of thickness at 50 keV for Si_3N_4, SiC, Ti_3Al, FeAl, and NiAl.

Figure 3.11 also indicates the need for using higher energies, from 30 to 100 keV, to discern differences in attenuation between or within SiC and Si_3N_4 samples. Consequently, the PSDR system was designed with these considerations in mind to better characterize SiC and Si_3N_4 samples and possibly SiC/RBSN composite samples.
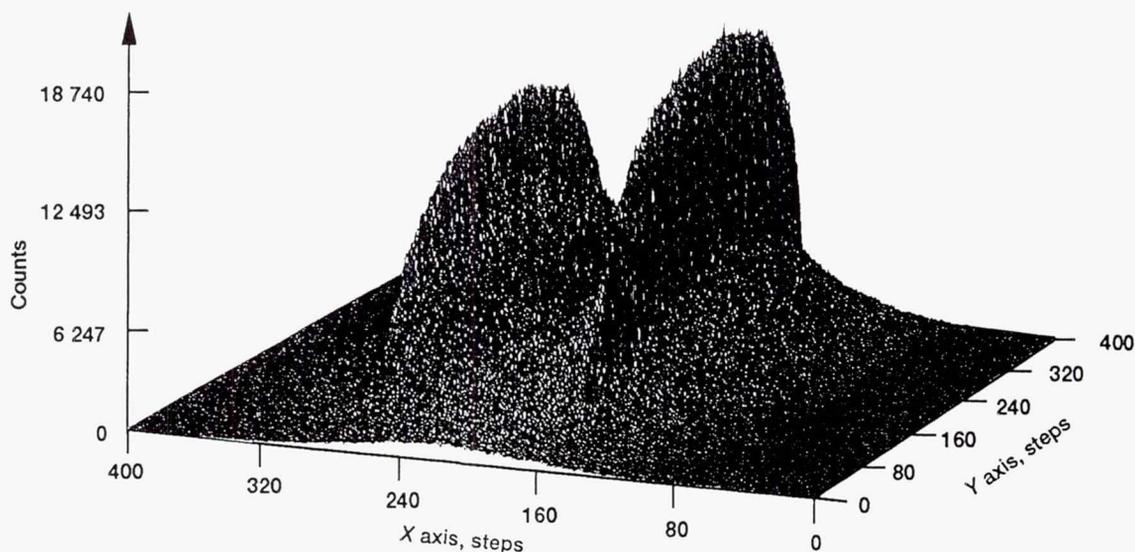
Figure 3.5.—X-ray beam profile of collimated copper tube.
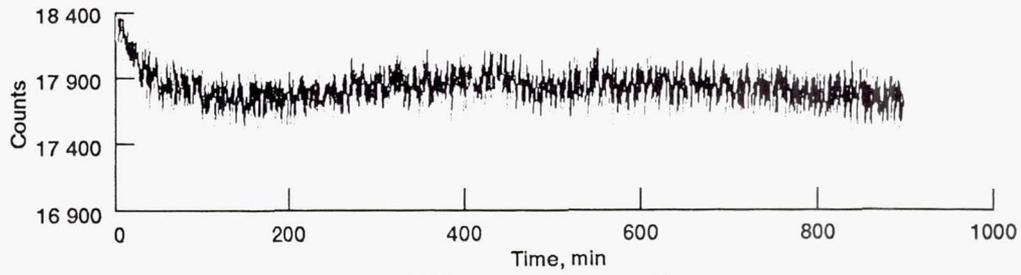
(a) Photon counts versus time.
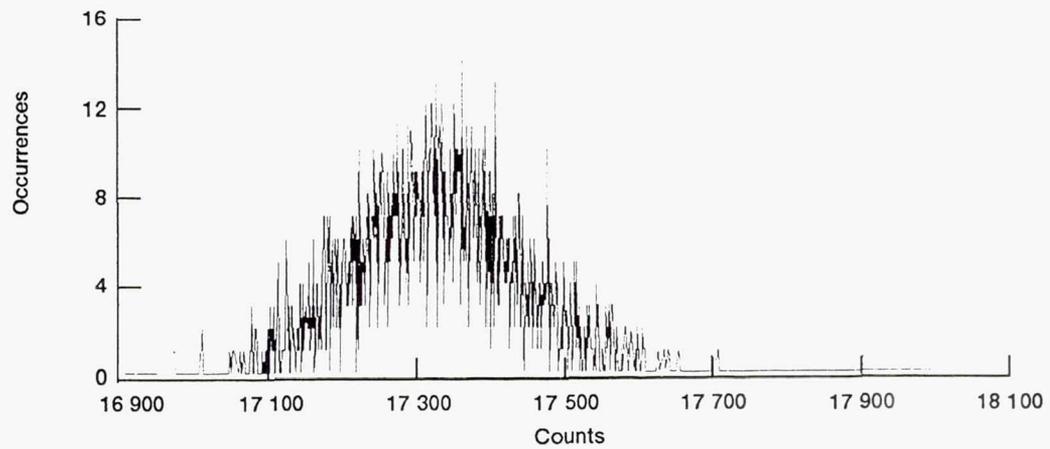
(b) Photon occurrences versus photon counts.
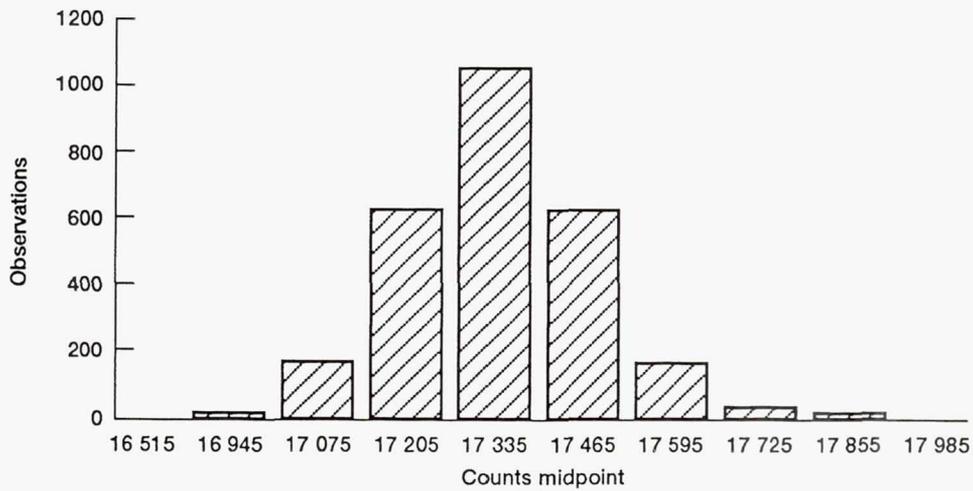
(c) Observations versus photon counts.

Figure 3.6.—Beam stability and related photon counts at optimized location for maximum photon counting. Mean, 17 335; square root of mean, 132; standard deviation, 130; minimum, 16 916; maximum, 17 994; (counts/0.1 sec) x 10 every 20 sec.
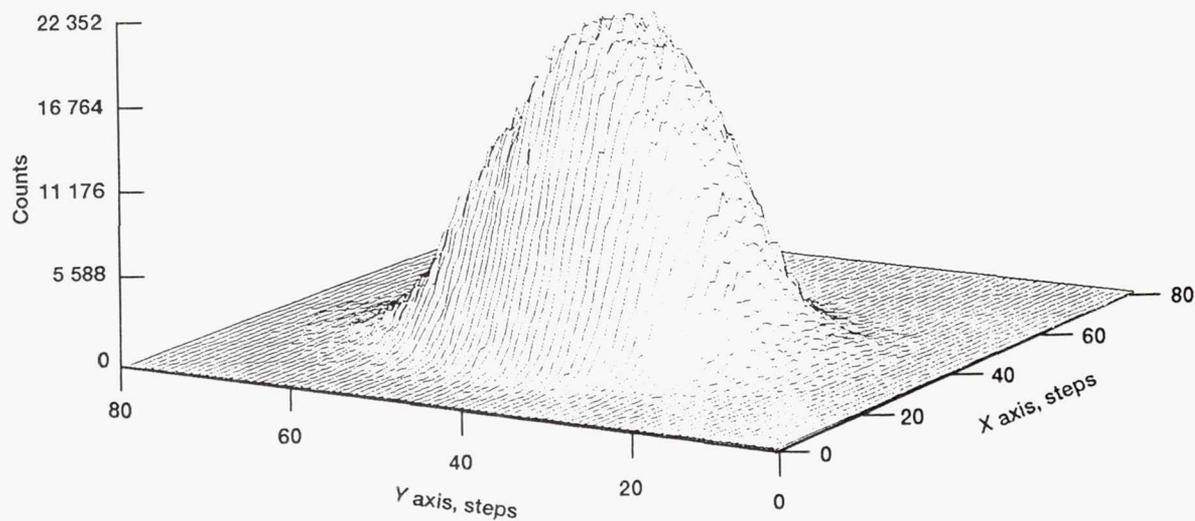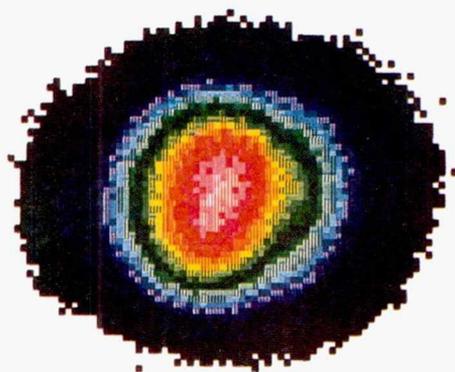
Figure 3.7.—X-ray beam profile of microfocus molybdenum system.
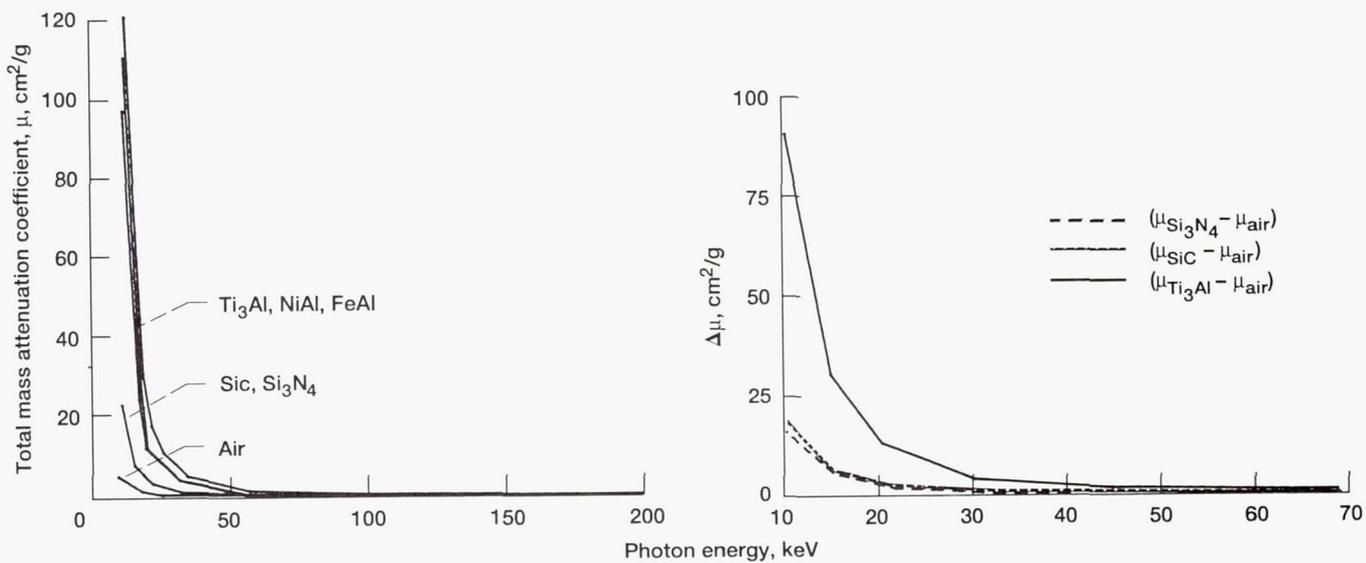
Figure 3.8.—Total mass attenuation coefficient and differential in total mass attenuation coefficient versus photon energy.

(a) Si$_3$N$_4$.

(b) SiC.
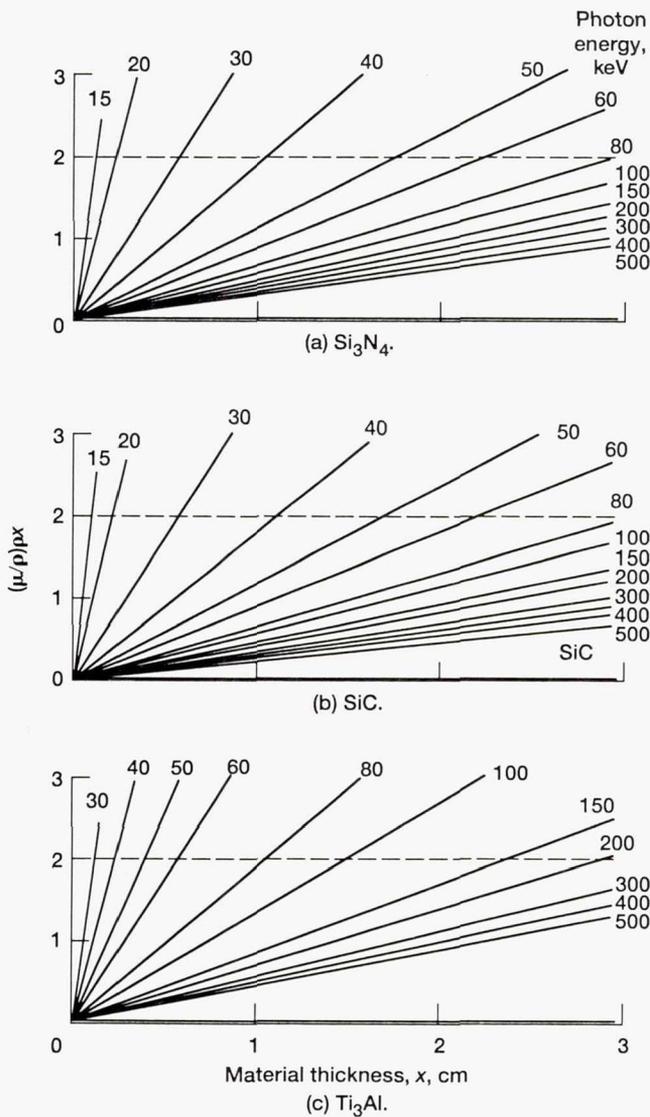
(c) Ti$_3$Al.

Figure 3.9.—Product of total mass attenuation coefficient and material thickness versus material thickness for Si$_3$N$_4$, SiC, and Ti$_3$Al.

(a) Si$_3$N$_4$.

(b) SiC.
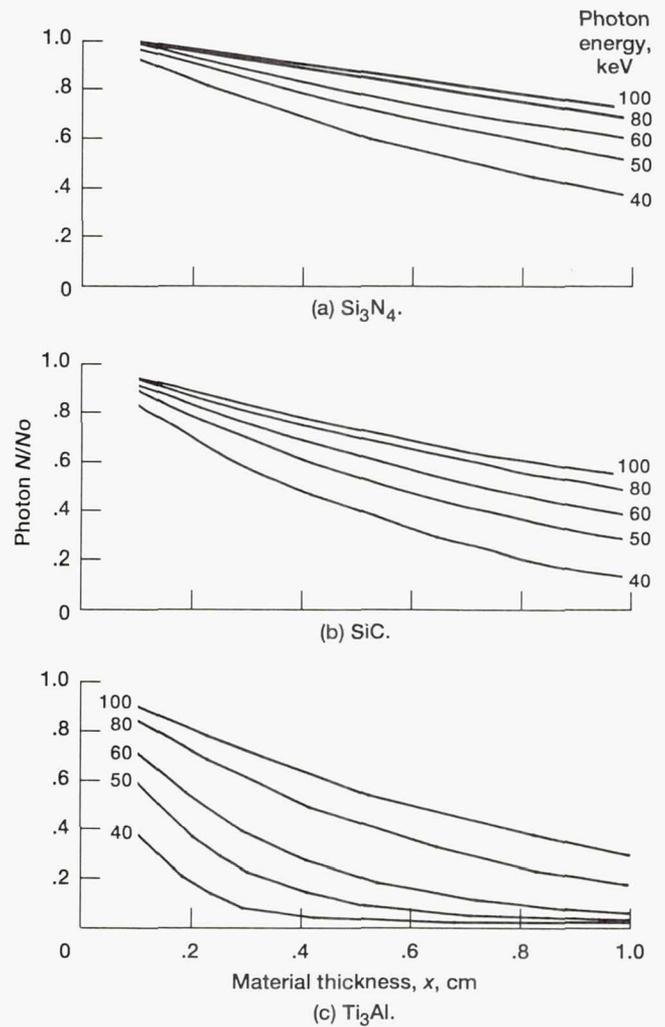
(c) Ti$_3$Al.

Figure 3.10.—Photon attenuation versus material thickness for Si$_3$N$_4$ SiC, and Ti$_3$Al.

(a) Thickness, 0.5 cm.

(b) Photon energy, 50 keV.
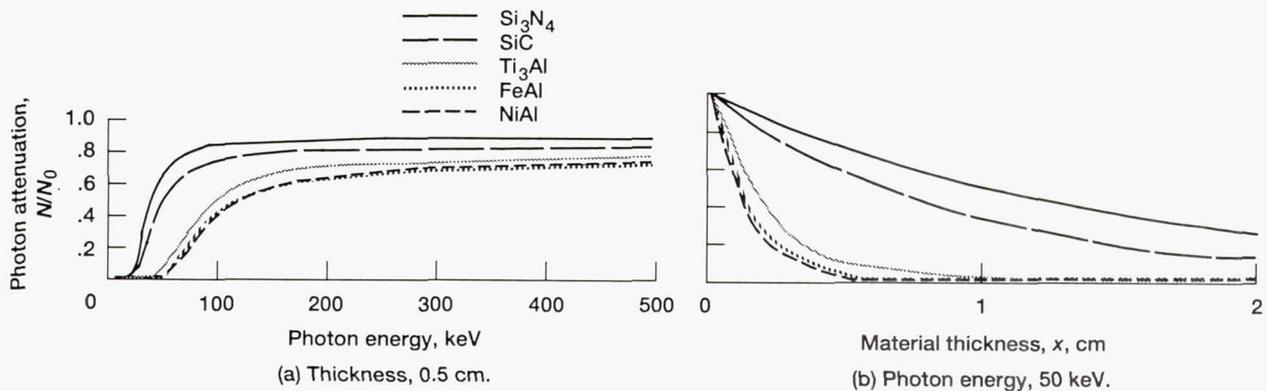
Figure 3.11.—Photon attenuation versus photon energy for 0.5-cm material thickness and versus material thickness at 50 keV.

3.3 Results and Discussion

3.3.1 Tungsten Fiber

A 75-μm-tungsten fiber with a lead spatial reference was scanned in air. The tube potential was 50 kV and the tube current was 34 mA. The source-to-fiber distance was 33 cm and the source-to-detector distance was 69 cm. The step size was 25 μm in the horizontal direction and 50 μm in the vertical direction. The scan (fig. 3.12) included 10 vertical steps and 200 horizontal steps. A three-dimensional representation of the digital radiographic data and two-dimensional selected
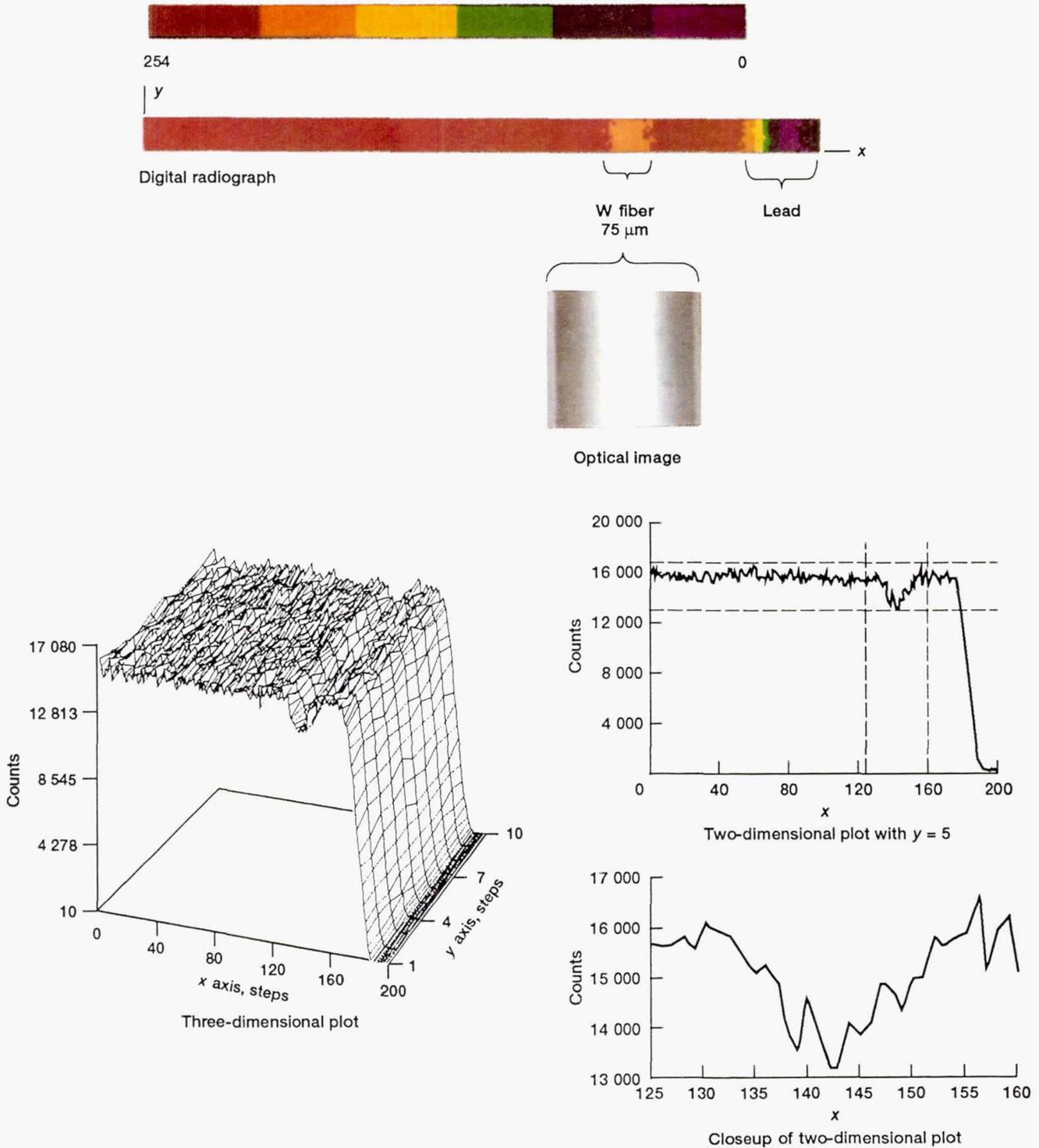
Figure 3.12.—Digital radiograph and three- and two-dimensional plots of tungsten fiber in air.
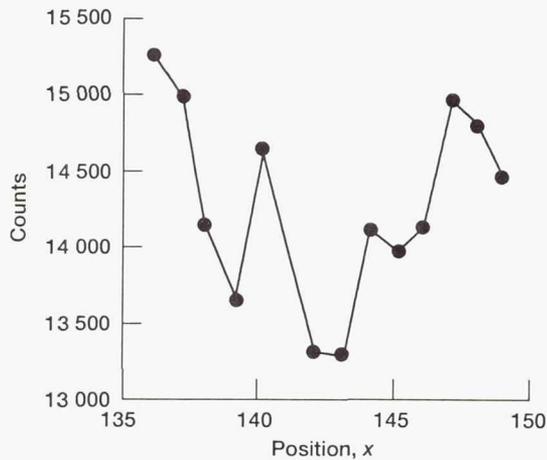
Figure 3.13.—Two-dimensional plot of photon counts passing through tungsten fiber versus position. $y = 5$; mean, 14 234; standard deviation, 639; minimum, 13 220; and maximum, 15 280.

profiles are also shown in figure 3.12. Figure 3.13 shows a line profile of photon counts versus position exactly over the fiber.

The tungsten fiber and the lead reference were successfully imaged as shown in figure 3.12. Approximately 3000 photons were attenuated by the tungsten fiber over the background attenuation in air. Because of the cylindrical shape of the fiber the photon counts varied considerably over the fiber

from a minimum of 13 220 to a maximum of 15 280 for a relatively high standard deviation of 639.

3.3.2 Silicon Carbide Fibers

A 142-μm-diameter SiC fiber with a lead frame serving as a spatial reference was scanned in air. Figure 3.14 shows a digital radiograph of the fiber area acquired at 45-kV tube potential and 35-mA tube current. Figure 3.15 shows a digital radiograph of the same area at 50-kV tube potential and 35-mA tube current. Figure 3.16 shows a digital radiograph of one tungsten fiber and four SiC fibers in air. The scans for figures 3.14 to 3.16 are of 300 horizontal steps by 100 vertical steps where the step size is 10 μm in both directions.

It is evident from figures 3.14 and 3.15 that the existing system cannot detect an SiC fiber in air. The displayed data show the presence of the lead reference but not the presence of the SiC fiber. Contrast stretching of the area where the fiber is located did not enhance the fiber detection capability.

In addition, figure 3.16 emphasizes the inability of the system to differentiate between air and SiC fibers. This implies similar detection problems with imaging SiC fibers in an Si_3N_4 matrix. Voids in Si_3N_4 are more detectable than SiC fibers because the $\Delta\mu$ is smaller in the fiber case, $(C_{sub})_f = (\mu_m - \mu_f) \times$ (Fiber diameter), than in the void case, $(C_{sub})_{void} = (\mu_m - \mu_{air}) \times$ (Void diameter).
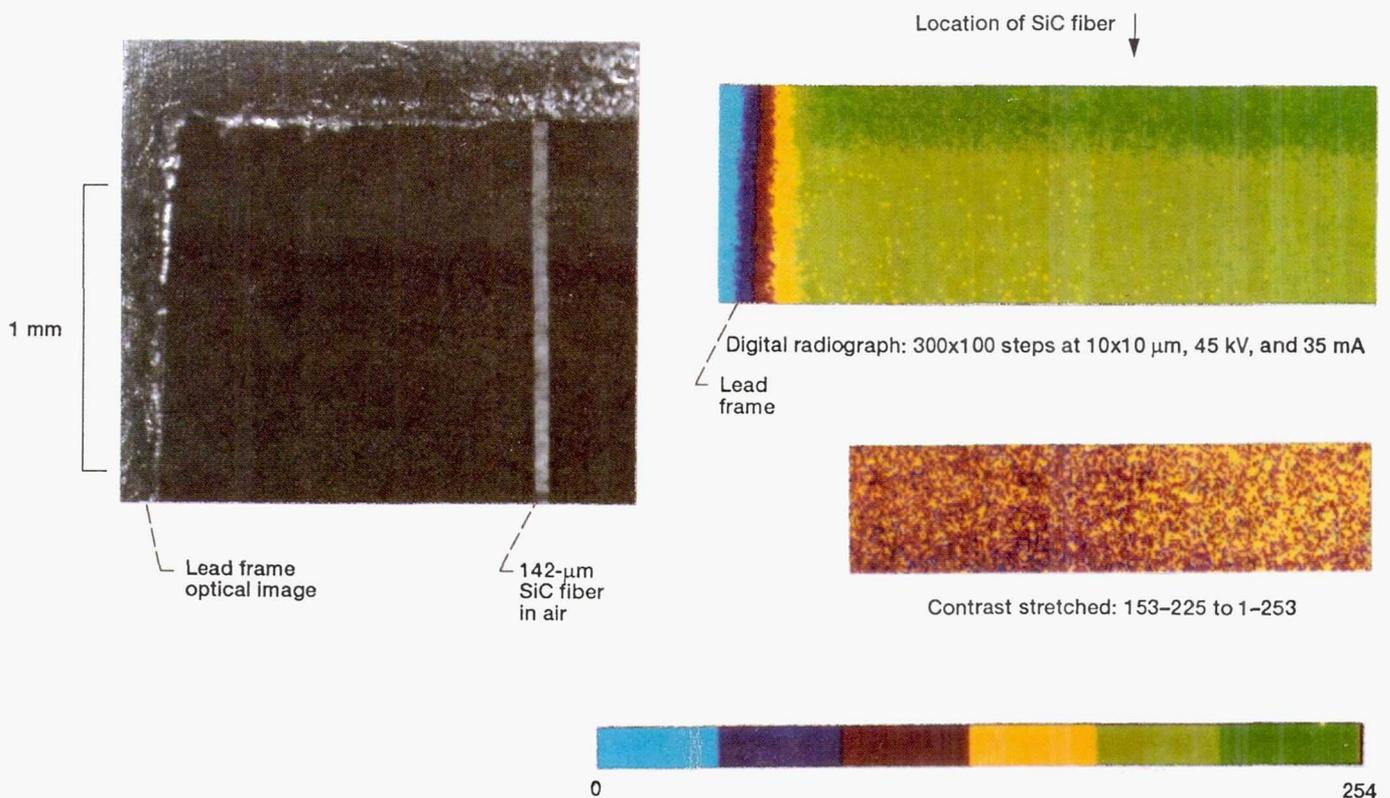

Figure 3.14.—Digital radiography of SiC (SCS–6, 142 μm) fiber in air at 45-kV tube potential.

Location of SiC fiber ↓

300x100 steps at 10x10 μm, 50 kV, and 35 mA

Lead
frame

Contrast stretched to 1–196 from 236–253

0   254
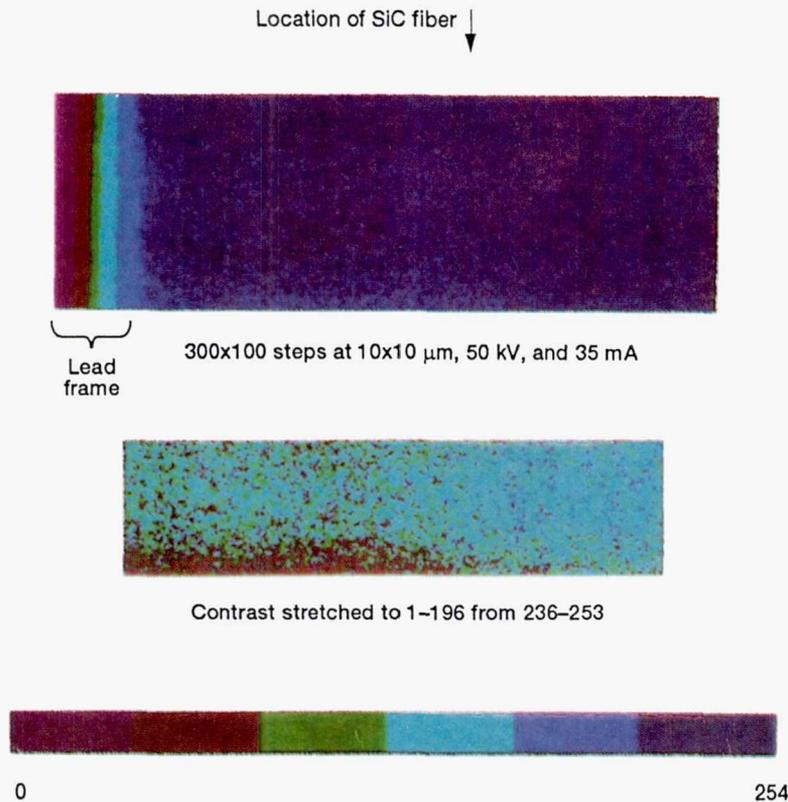
Figure 3.15.—Digital radiography of same SiC fiber shown in figure 3.14 at 50-kV tube potential.

Scans of the region of interest ($\sim$2 to 3 mm^2), by varying the time from 5 to 14 hr with sampling photon counts over 0.5 sec and averaging, did not show sufficient detectability improvement.

3.3.3 Silicon Nitride Bar

An Si$_3$N$_4$ modulus-of-rupture (MOR) bar was scanned. The bar was 0.6 cm wide, 0.35 cm thick, and 3.0 cm long. The tube potential was 50 kV and the tube current was 34 mA. The source-to-sample distance was 33 cm and the source-to-detector distance was 69 cm. The step size was 25 μm in the horizontal direction and 50 μm in the vertical direction. The scan (fig. 3.17) includes part of the original scan where 200 vertical steps by 500 horizontal steps were traversed.

The digital radiograph successfully detected the steel spring holder, the Si$_3$N$_4$ sample, and the anticipated high-density case and low-density core within the Si$_3$N$_4$ sample (Sanders and Baaklini, 1988). Contrast stretching further enhanced the density difference between the case and the core.

From figure 3.17 the ratio $N_{Si_3N_4}/N_{air}$ was about 0.25 in the case region and about 0.42 in the core region. This observation is a markedly different result than that obtained with monochromatic radiation ($N/N_0 = 0.8$) in figures 3.10 and 3.11. The PSDR system can be used to precisely study the attenuation mechanisms in polychromatic radiation experiments by incorporating a multichannel analyzer and a higher energy and flux density source.

The major limiting factors in the PSDR system are the focal spot size and the beam profile. The reason is that it was necessary to choose an x-ray diffraction tube instead of the copper or molybdenum radiographic tubes because of procurement restrictions.

With minor modifications the PSDR system is a viable tool for imaging subtle density variations in monolithic ceramics. However, this system is not appropriate for in situ monitoring of ceramic matrix composites under tensile loading because data acquisition is too time consuming and because a major modification must be made to the system to acquire the necessary contrast sensitivity for imaging the composite constituents.

Location of four SiC fibers

Digital radiograph: 300x100 steps at 10x10 μm

Contrast stretched

Four 142-μm SCS–6 fibers in air
Optical image

75-μm
W fiber
in air

0   254
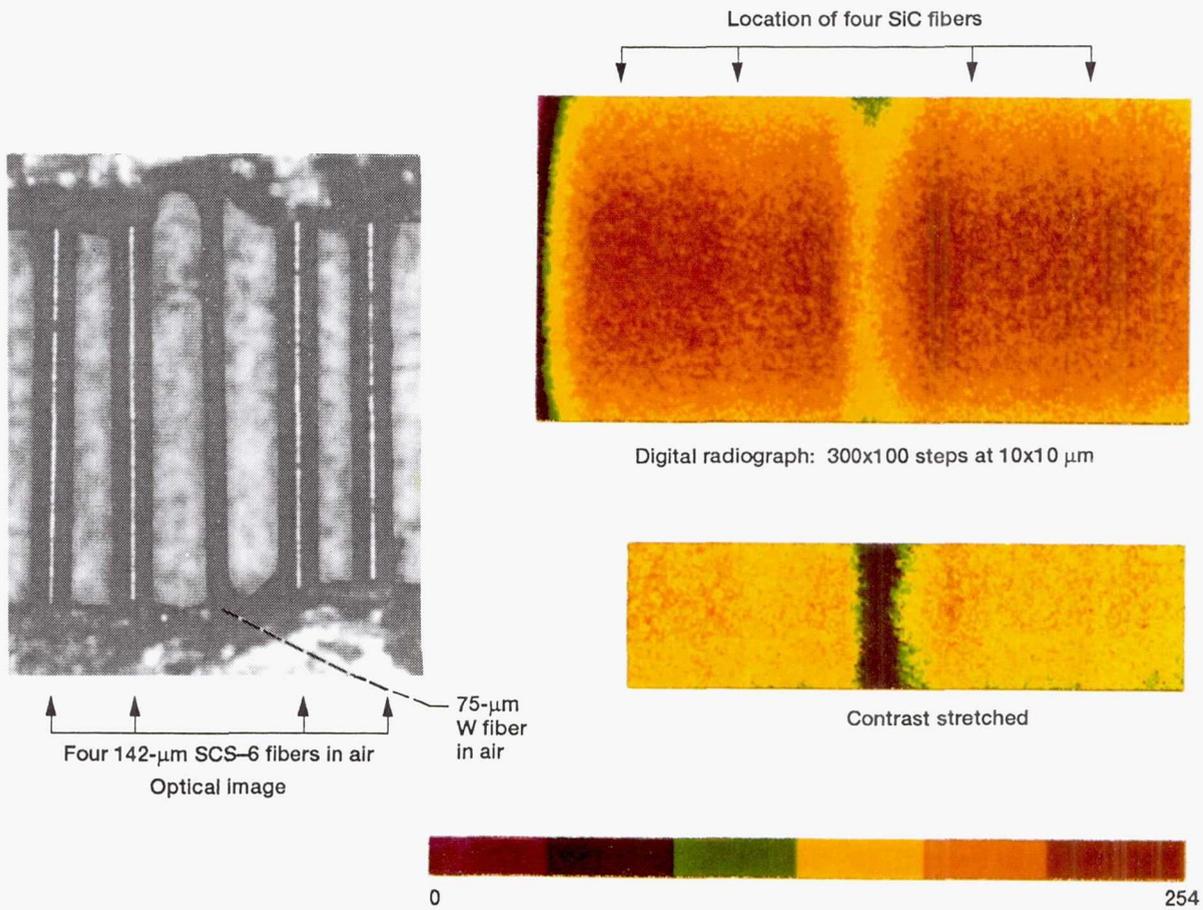
Figure 3.16.—Digital radiography of four SiC and one tungsten fiber in air.

Contrast
stretched

Pixel values,
60–108

254

0

Air

|← Case →|← Core →|← Case →|

1 cm

Steel
spring

Si$_3$N$_4$, 0.6 cm
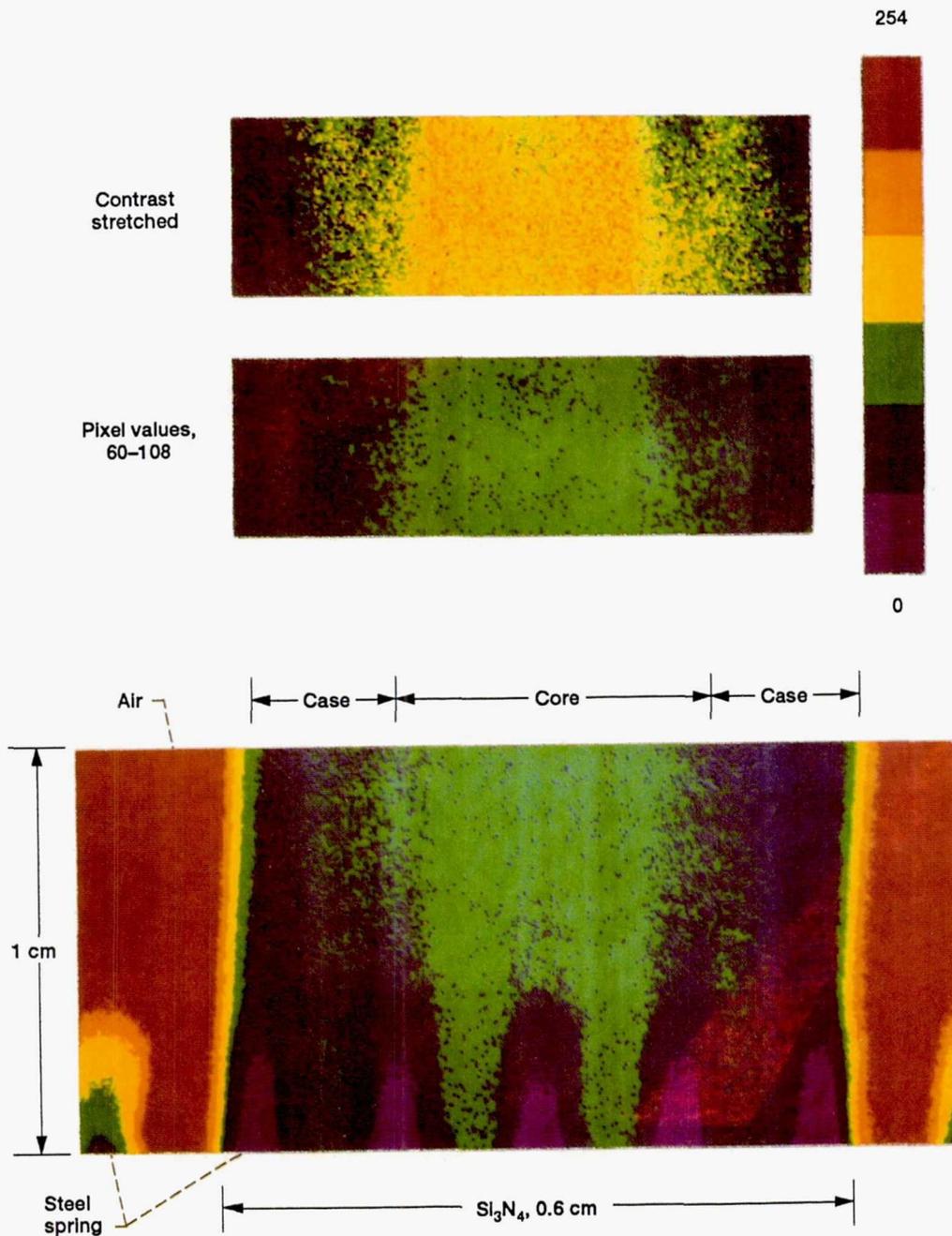
Figure 3.17.—Digital radiography of Si$_3$N$_4$ sample in air.

3.4 Conclusions

A point-scan digital radiography (PSDR) system has been developed with microcollimation on the order of 100 μm. The system is viable for characterizing density variations in monolithic ceramic specimens and for studying x-ray tube profiles.

The system, with minor modifications, can provide for detailed studies of x-ray attenuation mechanisms when polychromatic radiation sources are used. Modifications are needed before the PSDR system can be used for in situ monitoring of ceramic matrix composite samples under tensile loading.

Chapter 4

Characterization of Ceramic Disks and Engine Components by X-Ray Computed Tomography

4.1 Introduction

This chapter presents the capabilities and limitations of x-ray computed tomography (XCT) for characterizing monolithic ceramics. XCT is applied to Si_3N_4 disks, an Si_3N_4 blade, and an SiC rotor. The XCT findings are corroborated with microfocus radiography, scanning acoustic microscopy, and metallography.

Because overall density and density anomalies affect fracture strength and fracture toughness in monolithic ceramics, the emphasis in this chapter is on detecting density variations within selected regions of samples. At present, XCT is the only nondestructive evaluation technology that can adequately characterize the internal spatial density variations of fully densified objects.

4.2 Materials and Experimental Procedures

4.2.1 Materials

Silicon nitride disks, a prototype Si_3N_4 blade, and a prototype SiC rotor were evaluated in this study. Silicon nitride disks (fig. 4.1) and a blade (fig. 4.2) were made by the ceramic sintering methodology described in chapter 2. The SiC rotor (fig. 4.3) was fabricated by the injection molding technology described in chapter 2.

4.2.2 Systems

XCT, microfocus radiography, scanning acoustic microscopy, and optical microscopy were the principal NDE methods applied.

The XCT system used in this investigation is a laminography/dual energy (LAM/DE) system.[9] LAM/DE is a second-generation CT scanner (i.e., a translate-rotate CT scan geometry system). For this geometry the scanning process consists of translating the specimen or component past the x-ray beam, rotating it, and translating it past the x-ray beam again until the specimen has been rotated 180°. LAM/DE includes a 420-kV isovolt x-ray source and a $CdWO_4$ linear array detector with a 128-mm field of view. The x-ray source is collimated to 91.44 cm in the horizontal direction and to 6.35 cm in the vertical direction, generating a fan-shaped beam. The slice thickness can be adjusted from 1 mm to 15 mm. In this research the slice thickness was approximately 2 mm, the image pixel size was 250 μm, the pixel integration time was 55 msec, and the total scan time per slice was 20 to 30 min. The scanning geometry of the LAM/DE system is shown schematically in figure 2.8.

The microfocus radiographic system with low energy (up to 10 W) was used to evaluate actual cross-sectional slices. The microfocus system was operated in the projection mode (2 to 4X magnification) and in the 30- to 60-kV range with a beam current of 0.25 to 0.32 mA. The system had a molybdenum anode and a 10-μm focal spot. The detection medium was Kodak film type M. The film was backlighted and digitized. The digitized image was color coded to incrementally show radiographic density differences. A schematic of the microfocus projection radiography system is shown in figure 2.1(c).

A pulse-echo/pulse-reflection SAM system was also applied to the samples. A reduced-aperture lens was used at a nominal 50-MHz center frequency. The acoustic lens was

---

[9]Designed and built by Advanced Research and Applications Corporation for the Wright-Patterson Air Force Base, OH.
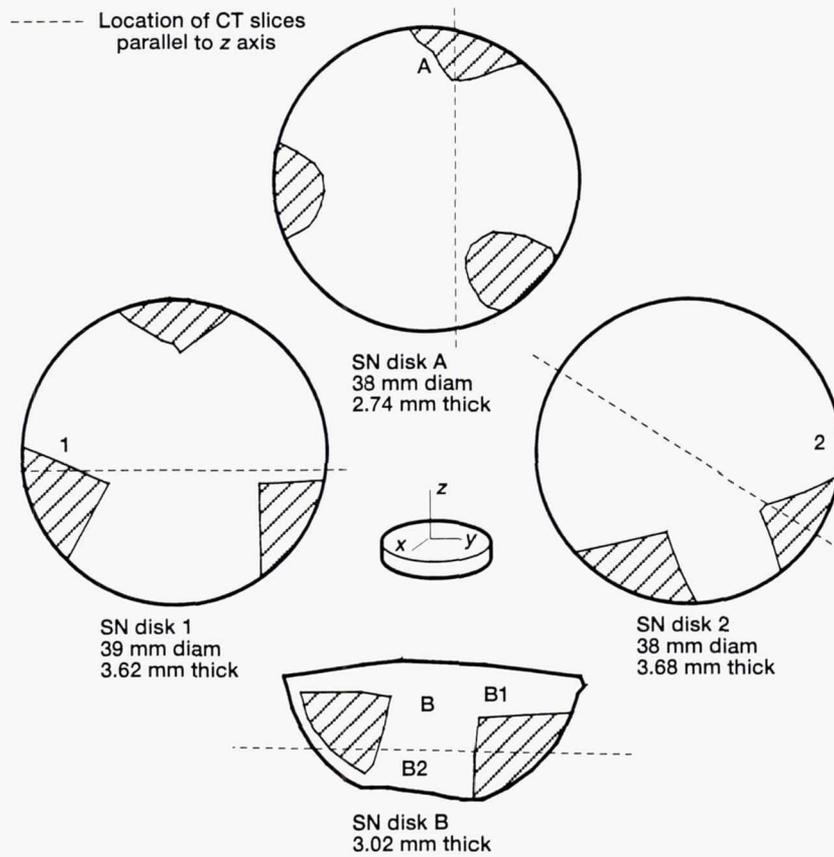
Figure. 4.1.—Schematic of Si_3N_4 disks showing location of cross-sectional slices (parallel to z axis) of interest.

35 mm

25 mm

21 mm

2.39 mm thick

SN blade S1:
cross section (x, y);
2.39 mm thick

30 mm

18 mm

z

y

x

SN blade S2:
cross section,
(parallel to z axis);
2.88 mm thick
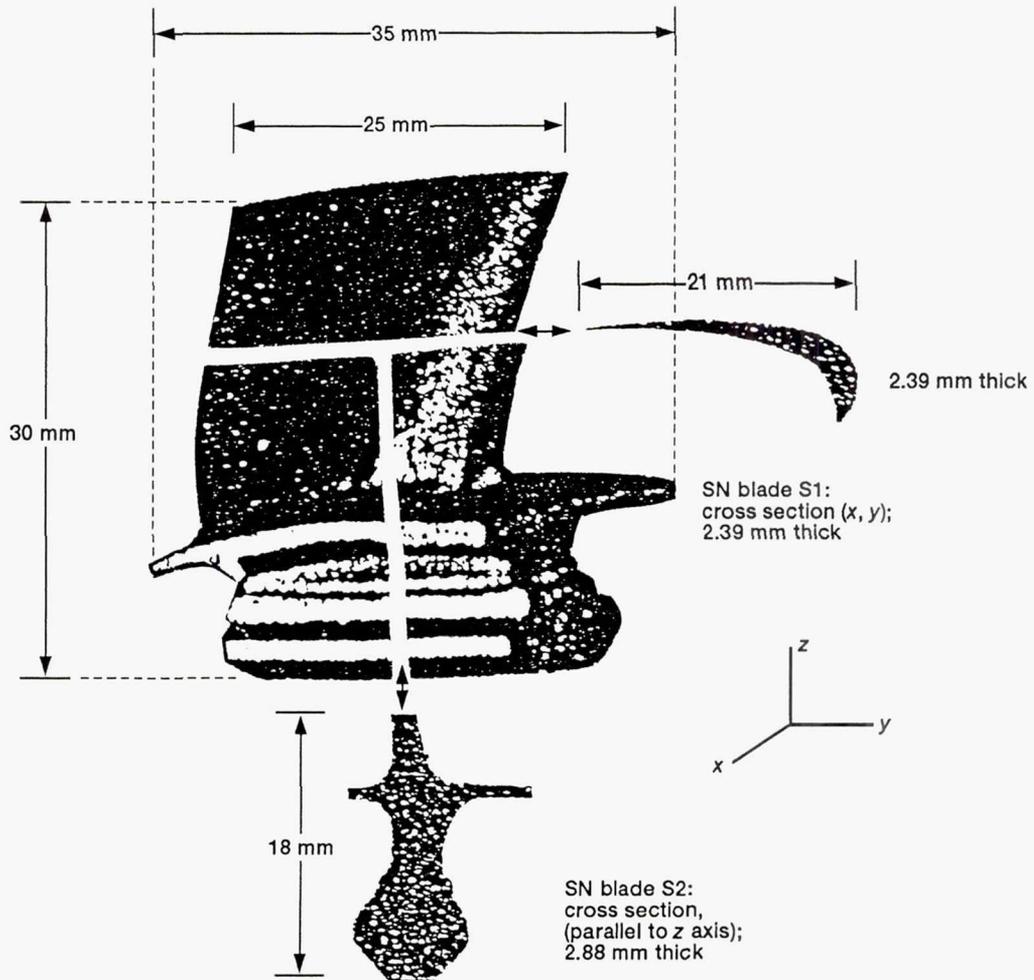
Figure 4.2.—Sketch of Si_3N_4 blade showing cross-sectional slices of interest.
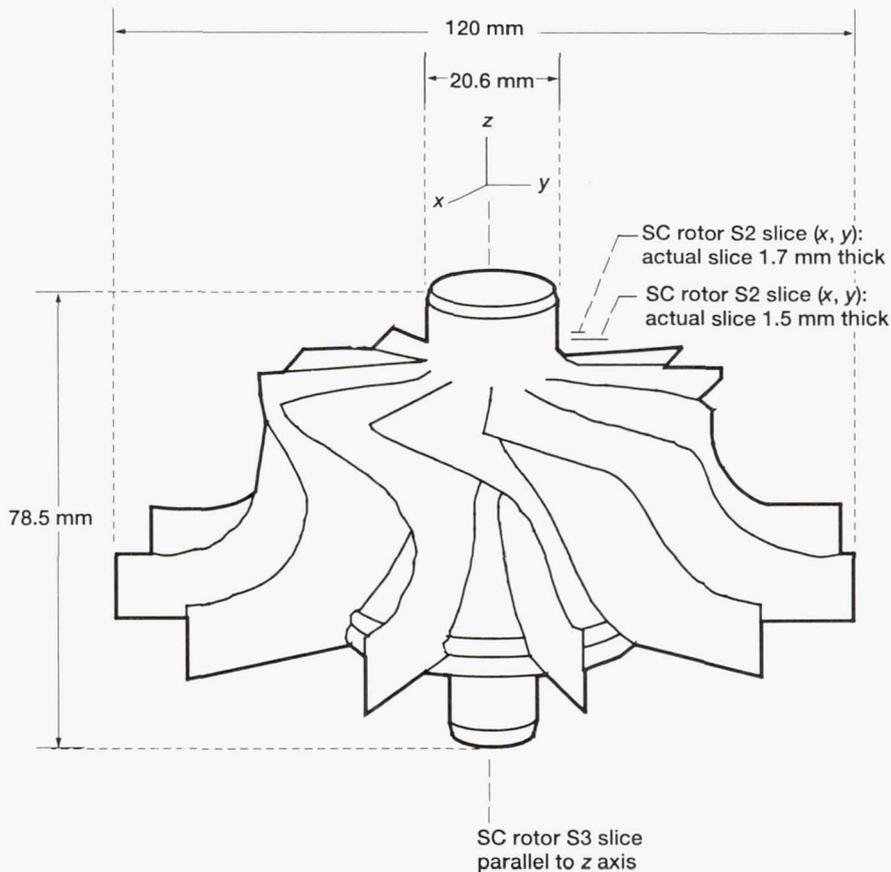
Figure 4.3.—Schematic of SiC rotor showing location of cross-sectional slices of interest.

positioned above the sample in a distilled-water coupling bath. The transducer generated and detected ultrasonic pulses. Stepper motors drove the sample in a raster pattern as the reflected signal amplitude was digitally stored as a function of position. An adjustable delay time between pulse generation and signal digitization allowed imaging of either near-surface or subsurface sample slices. A schematic diagram of the lens-specimen configuration is shown in figure 2.9(b).

4.2.3 Procedures

In-plane (x,y) CT evaluations (fig. 4.4) were performed on sintered ceramic disks. In addition, selected CT slices parallel to the z axis (fig. 4.5) were imaged. One side of each disk was polished for metallographic examination. Thereafter, the disks were radiographically imaged as shown in figure 4.6, and selected optical micrographs were taken as shown in figure 4.7. SN disk B was cut into two pieces, B1 and B2, in order to expose the internal microstructure of the CT slice in a plane parallel to the z axis. The B2 face was polished and selected micrographs were taken as shown in figure 4.8.

CT evaluations were performed on three selected cross sections of the SiC rotor as identified in figure 4.3 and as shown in figures 4.9 to 4.11. After the CT evaluation the actual slices, SC rotor S1 and SC rotor S2 were cut out from the rotor. Then the rotor was cut in approximately two halves, exposing two internal faces from SC rotor S3. One of these faces was polished and characterized metallographically as shown in figure 4.10. One side of the slices SC rotor S1 and SC rotor S2 was polished. Thereafter, these slices were radiographed as shown in figure 4.12. Optical micrographs were taken to highlight microstructural porosity variations as shown in figures 4.13 and 4.14. In addition, subsurface scanning acoustic microscopy images were made of SC rotor S1 as shown in figure 4.15.

A CT evaluation of slice SN blade S1 (figs. 4.2, 4.16, and 4.17) was performed while the Si_3N_4 blade was still intact. The SN blade S1 physical segment corresponding to the CT slice was then cut out of the airfoil. Next, CT slice SN blade S2 was evaluated (figs. 4.16 and 4.17) and then cut out of the blade/airfoil root of the blade for subsequent metallographic evaluation. Radiographic (figs. 4.18 and 4.19) and ultrasonic (fig. 4.20) evaluations were performed on both blade slices.

TABLE 4.1 – DENSITIES AND CT NUMBERS FOR Si_3N_4
DISKS AND SLICES FROM Si_3N_4 BLADE
AND SiC ROTOR

Sample	Average CT number	Green density, g/cm^3	Sintered density, g/cm^3	Immersion density, g/cm^3
SN disk 1	3343	1.87	3.20	3.24
SN disk 2	3347	1.91	3.16	3.25
SN disk A	3309	1.91	3.19	3.24
SN disk B:	3354	1.86	3.15	3.26
B1	------	------	------	3.26
B2	------	------	------	3.26
SN blade S1	3100	------	------	3.17
SN blade S2	3250	------	------	3.19
SN rotor S1	2990	------	------	3.10
SN rotor S2	3070	------	------	3.12

Immersion densities were determined by the Archimedean principle for all Si_3N_4 disks and all cutout physical segments (actual slices) of the Si_3N_4 blade and the SiC rotor (table 4.1).

4.3 Results and Discussion

4.3.1 Silicon Nitride Disks

The hatched areas in figure 4.1 are regions where the surfaces of the Si_3N_4 disks were light gray. The unhatched areas were dark gray. These contrasting areas were attributed to contact with boron nitride (BN) spacers between the disks during sintering. The spacers apparently prevented uniform heating and consequently reduced densification of the disk regions in contact with the BN. This a priori knowledge guided the selection of the CT slices (parallel to z axis) as indicated in figure 4.1. The objective was to find out whether these low-density regions existed throughout the disks.

CT images of in-plane (x,y) slices (fig. 4.4) show that the CT number variations were more pronounced in localized regions of SN disk 1 than in disks 2, A, and B. Similarly, figure 4.5 shows that the CT number and by implication the density variations were more pronounced near the midplanes of SN disk 1 than in disks 2, A, and B. Also, through-the-thickness microfocus radiography illustrated in figure 4.6 shows that the density was more uniform for SN disk 2 than for SN disk 1.

Optical micrographs (fig.4.7) reveal that more porous (i.e., less dense regions) corresponded to the BN/Si_3N_4 contact areas. In addition, the radiographic image of SN disk 1 (fig. 4.6) reveals similar evidence of low-density regions. Figures 4.8 and 4.9 confirm that lower CT numbers corresponded, in general, to regions with high porosity (low density).

X-ray diffractometer scans of polished SN disk A at the BN/Si_3N_4 contact regions and at other regions showed β-Si_3N_4 to be the only detectable crystalline phase. There was no evidence of boron diffusion into the Si_3N_4 disks. This demonstrated that the only variations in these disks were density (porosity) variations.

It can be concluded that both radiography and tomography detected significant through-the-thickness density (porosity) variations in SN disk 1 and SN disk 2. Superficial near-surface density (porosity) variations tended not to show up in tomographs and radiographs because of a lack of contrast relative to overall thickness.

4.3.2 Silicon Carbide Rotor

The CT image of the slice SN rotor S3 reveals lower CT numbers in the rotor hub region (yellow-red) and higher CT numbers (yellow-green) toward the outside edge. This was substantiated by higher porosity (reduced density) at point A in figure 4.10 versus lower porosity (higher density) at
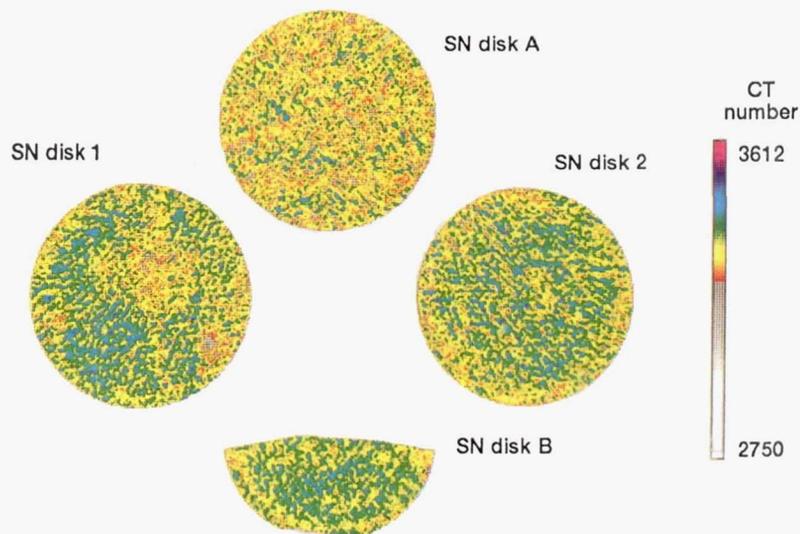
Figure 4.4.—CT images of in-plane (x, y) slices from Si_3N_4 disks.

(a) SN disk 1.

(b) SN disk 2.

(c) SN disk A.

(d) SN disk B.

CT number

3546

3000

3530

3000

3409

3000

3374

3000
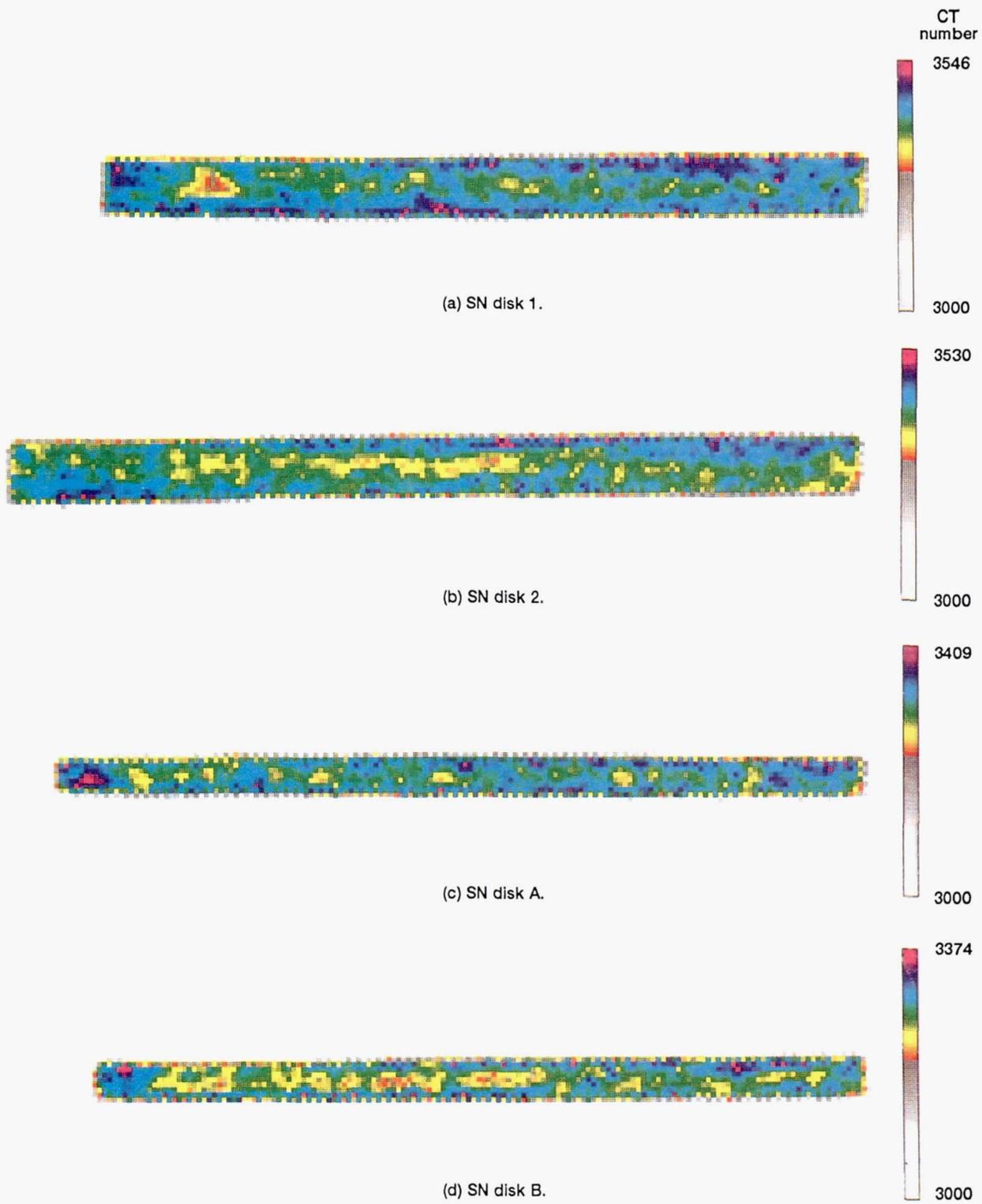
Figure 4.5.—CT images of selected slices (parallel to z axis) as indicated in figure 4.1.
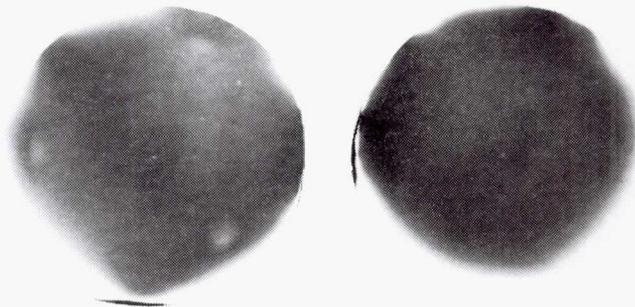
(a) SN disk 1.   (b) SN disk 2.

Figure 4.6.—Through-the-thickness microfocus radiography of SN disk 1 and SN disk 2.

2750   3612

CT number

200 μm
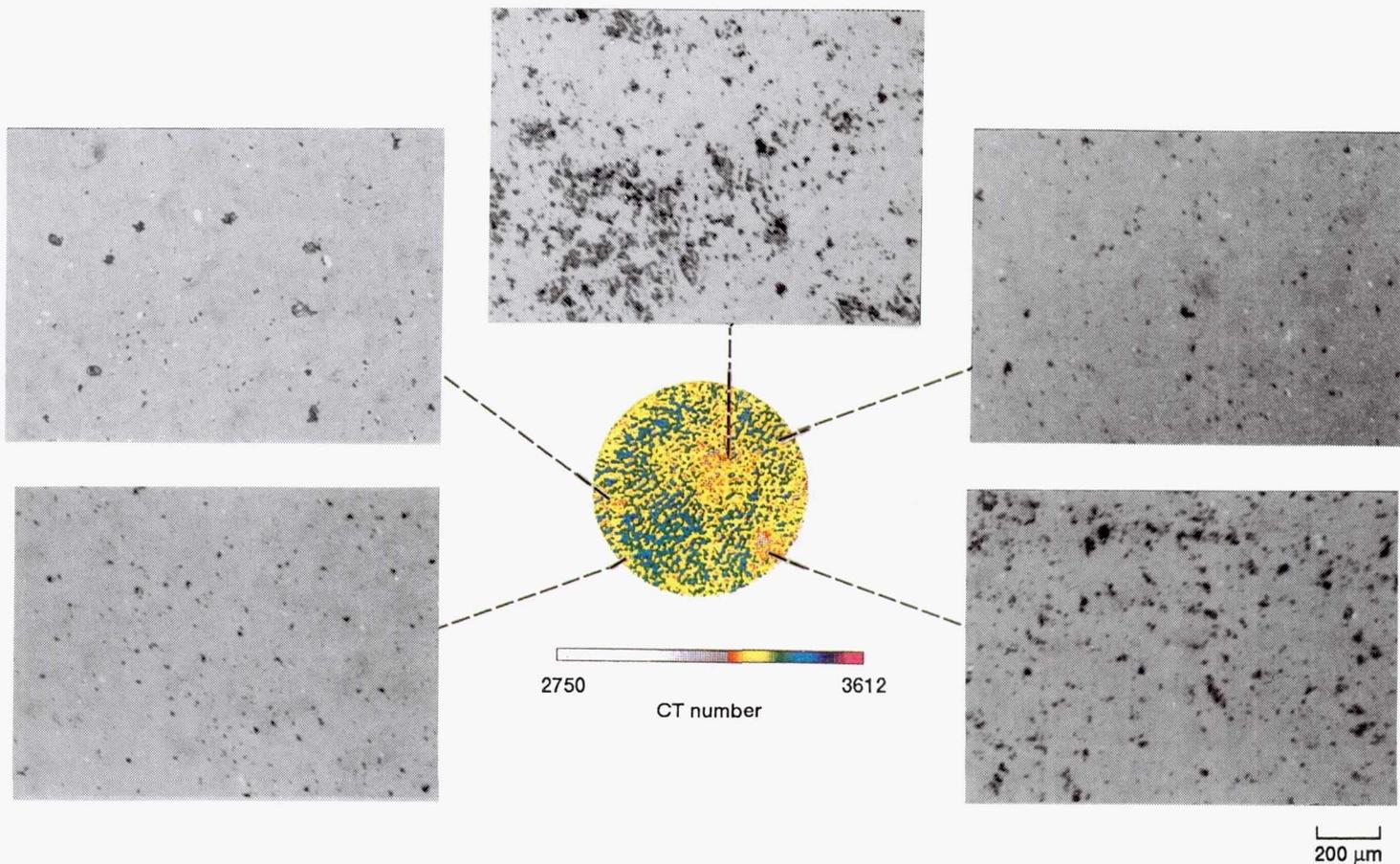
Figure 4.7.—Optical micrographs highlighting microstructure of different regions on polished SN disk 1.
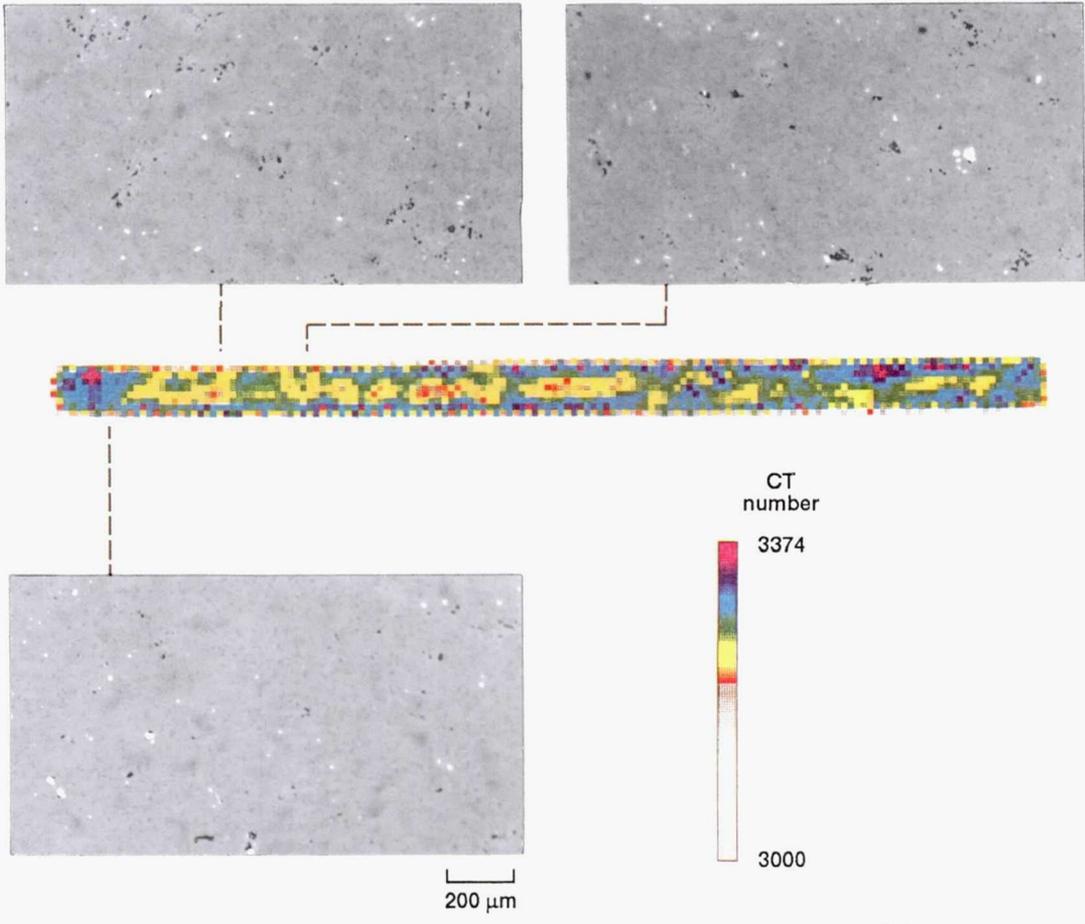
Figure 4.8.—Optical micrographs highlighting microstructure of different regions on polished SN disk B (parallel to z axis) slice.
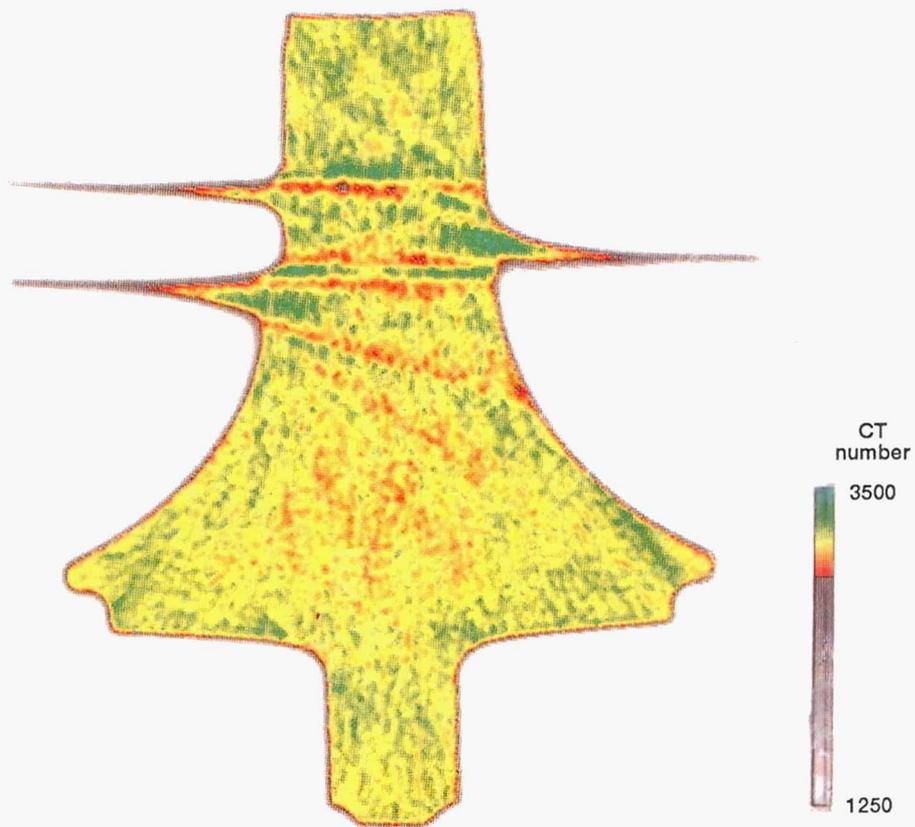
Figure 4.9.—CT image of cross-sectional slice (parallel to z axis) of SC rotor S3.
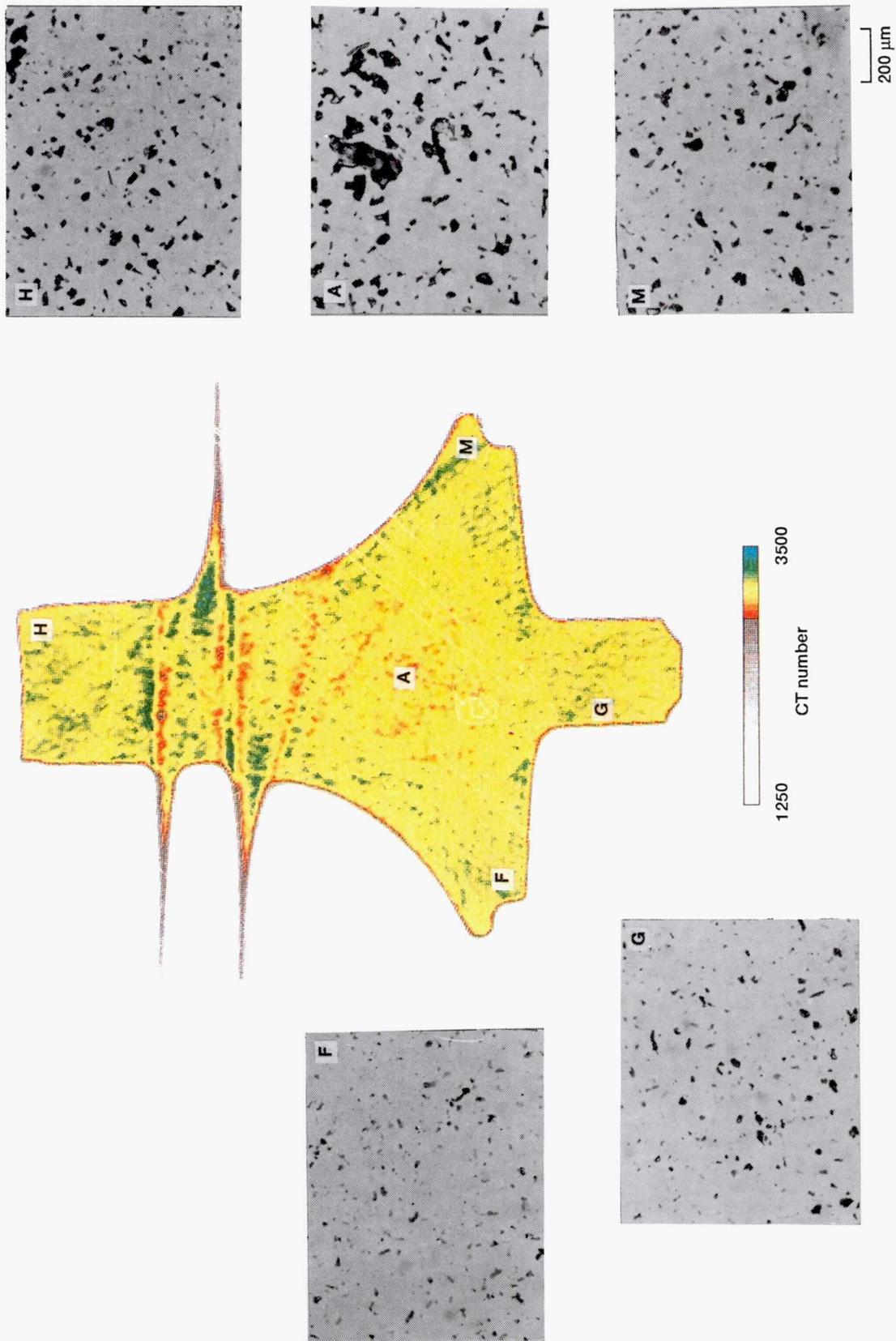
Figure 4.10.—Optical micrographs highlighting microstructure of different regions on polished SC rotor S3 face.
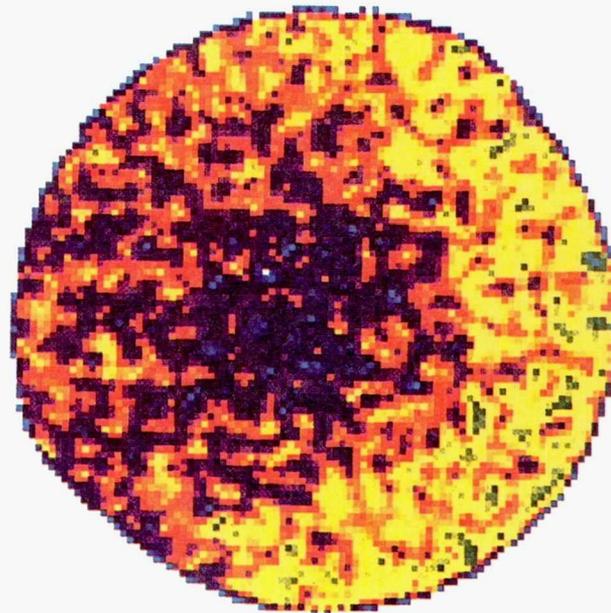
(a) SC rotor S1.
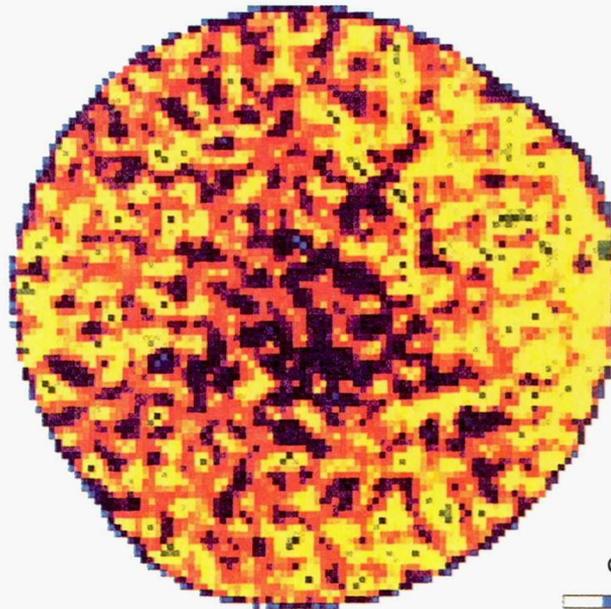
(b) SC rotor S2.

CT number

2625   3328

Figure. 4.11.—CT images of cross-sectional slices of SC rotors S1 and S2.

point F in the optical micrographs. However, the green-red striations emerging from the protruding blades were CT artifacts and not true CT number variations. Figure 4.10 shows one example at point M where the microstructure would be of reduced porosity if the green striation reflected true high-density regions. The microstructure at point M had porosity similar to that at point H.

The CT image of SC rotor S1 (fig. 4.11(a)) depicts a half moon of higher CT numbers (yellow) than those in the center

region (black). Slice SC rotor S2 (fig. 4.11(b)) exhibits lower density than slice S1 in the center region and higher density near the edge. The radiographic images in figure 4.12, the optical micrographs in figures 4.13 and 4.14, and the subsurface ultrasonic scan in figure 4.15(b) exhibit similar density variations detected by the CT number variations in figure 4.11. Furthermore, figure 4.15(a) features a cluster of voids in a plane directly above that of figure 4.15(b).
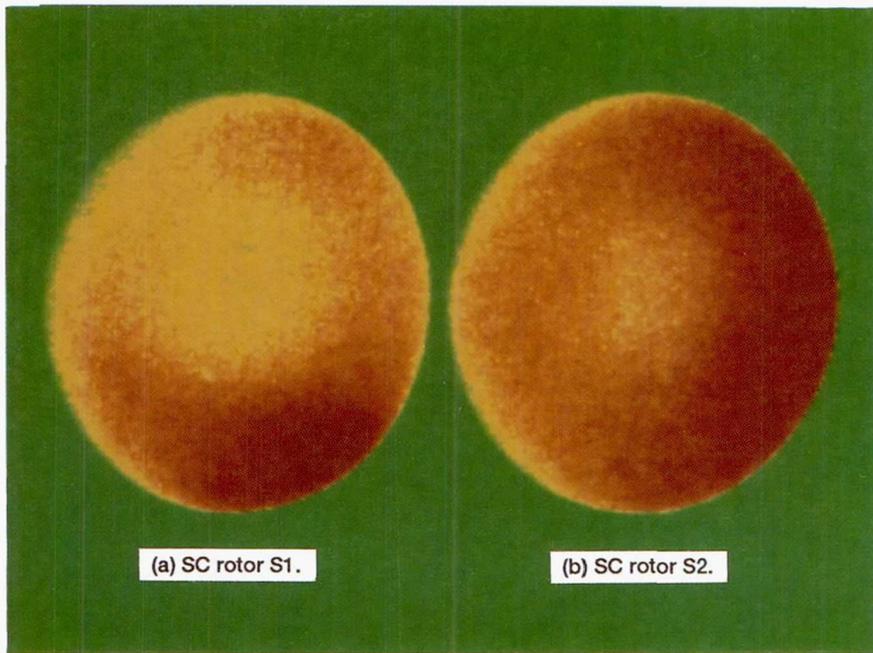
More
dense

Less
dense

Figure 4.12.—Radiographic images of cross-sectional slices.
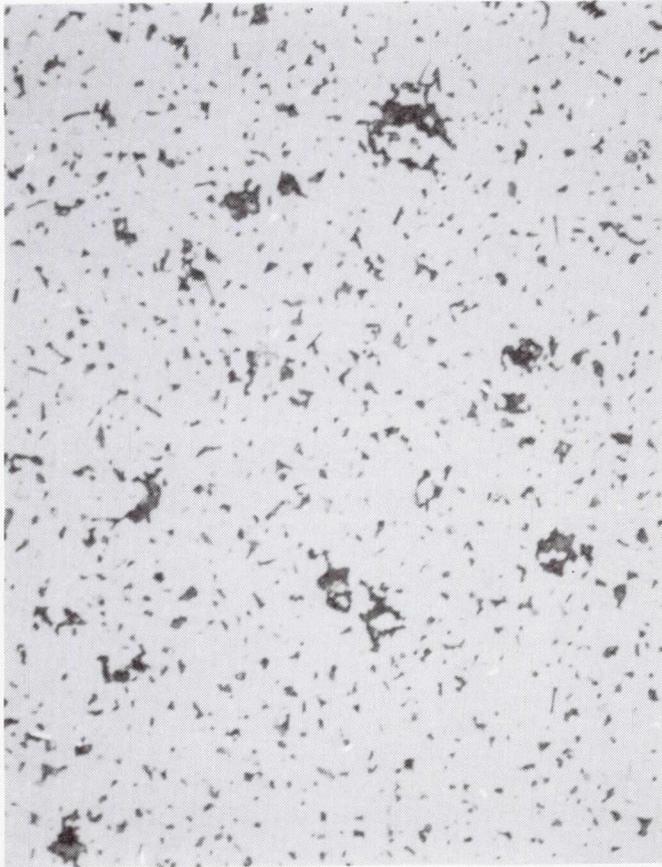
(a) Center.

(b) Higher density edge.

200 μm
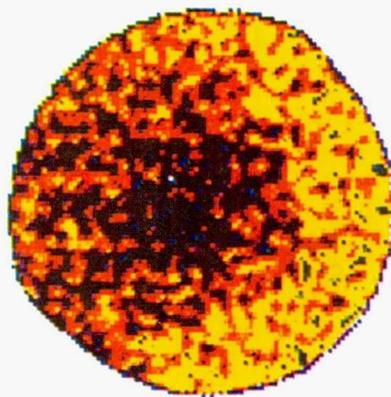
Figure. 4.13.—Optical micrographs highlighting microstructure of polished SC rotor S1 face in center and in higher density edge.
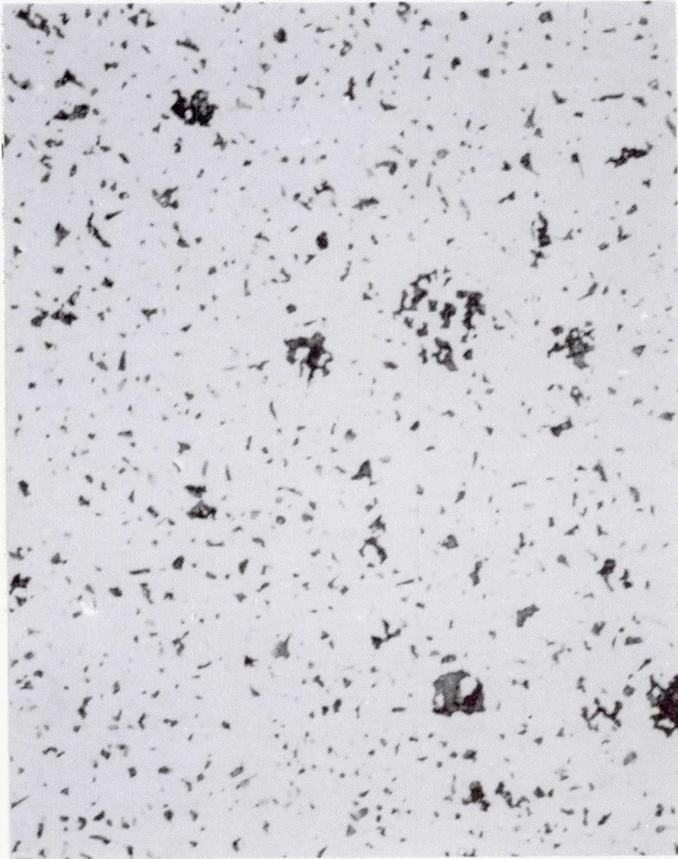
(a) Center.

(b) Higher density edge.

200 μm
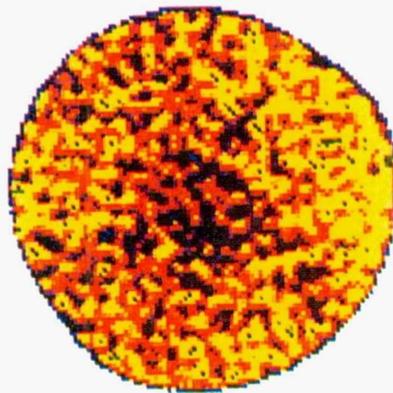
Figure 4.14.—Optical micrographs highlighting microstructure of polished SC rotor S2 face in center and in higher density edge.
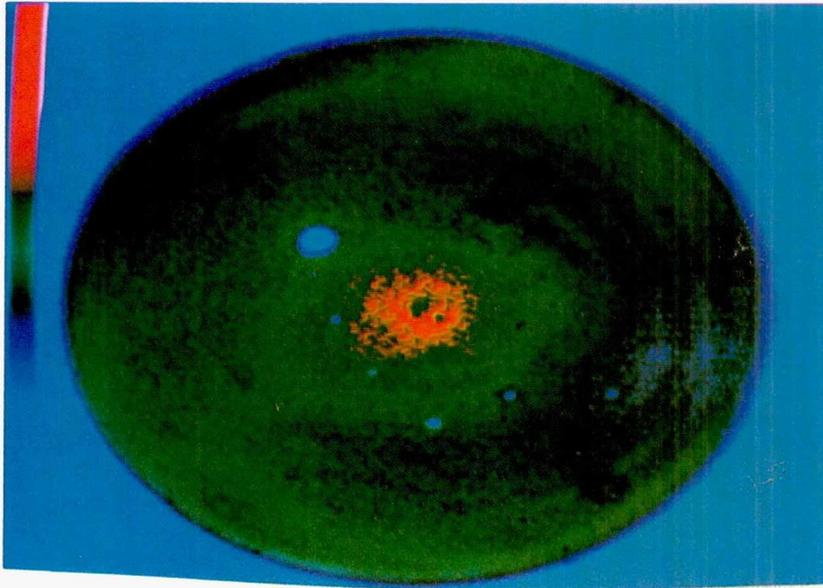
(a) 1.1 mm below surface.
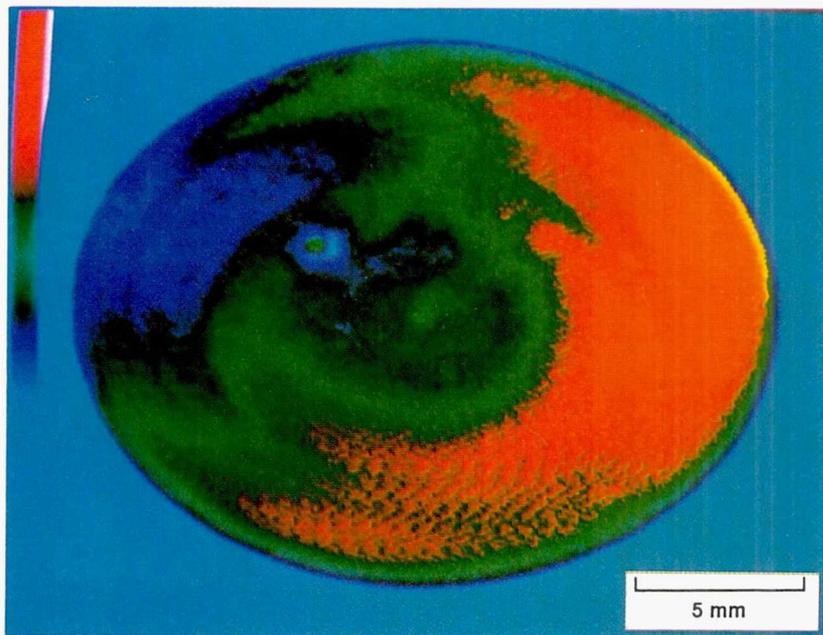
(b) 1.3 mm below surface.

Figure 4.15.—Scanning acoustic microscopy images of SC rotor S1 face.

4.3.3 Silicon Nitride Blade

CT images of SN blade S1 and SN blade S2 (fig. 4.16) and related CT number traces (fig. 4.17) demonstrate the limitations of XCT in characterizing relatively small and complex geometrical components. Density variations detected in these images could not be verified with optical microscopy. Optical microscopy shows that the microstructure was uniform throughout the polished surfaces of the two slices. Apparent density changes in figures 4.18 and 4.19 are ascribable primarily to thickness variations instead of to actual density or porosity variations. This was due to difficulties in grinding the two slices flat and sufficiently parallel to eliminate the masking effect of thickness on the imaging of true density variations within the slices.

Scanning acoustic microscopy was used to verify general microstructural uniformity as shown in figure 4.20. These ultrasonic subsurface images show that density was uniform throughout the slices and possibly that a higher density skin existed in both slices. The second finding was confirmed by projection radiography and low magnification optics (fig. 4.21).

4.3.4 Density Versus CT Number for SiC and Si_3N_4 Ceramics

The immersion densities of the disks and the cutout segments are plotted in figure 4.22 versus the corresponding average CT numbers. The coefficient of correlation r between bulk density and CT number was 0.98 for the monolithic ceramics examined.

It was demonstrated that XCT can be used to evaluate density variations. By minimizing or accounting for CT artifacts, tomographic density information can be used to characterize material properties and to identify anomalies that can affect the structural integrity of components.

(a) SN blade S2.
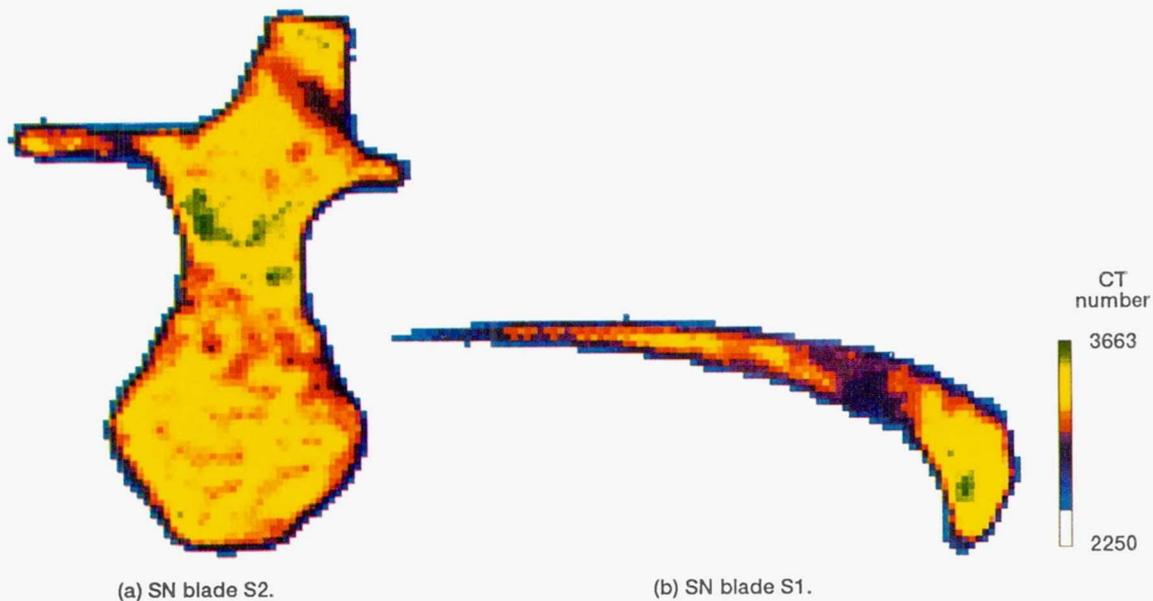
(b) SN blade S1.

Figure 4.16.—CT images of cross-sectional slices.
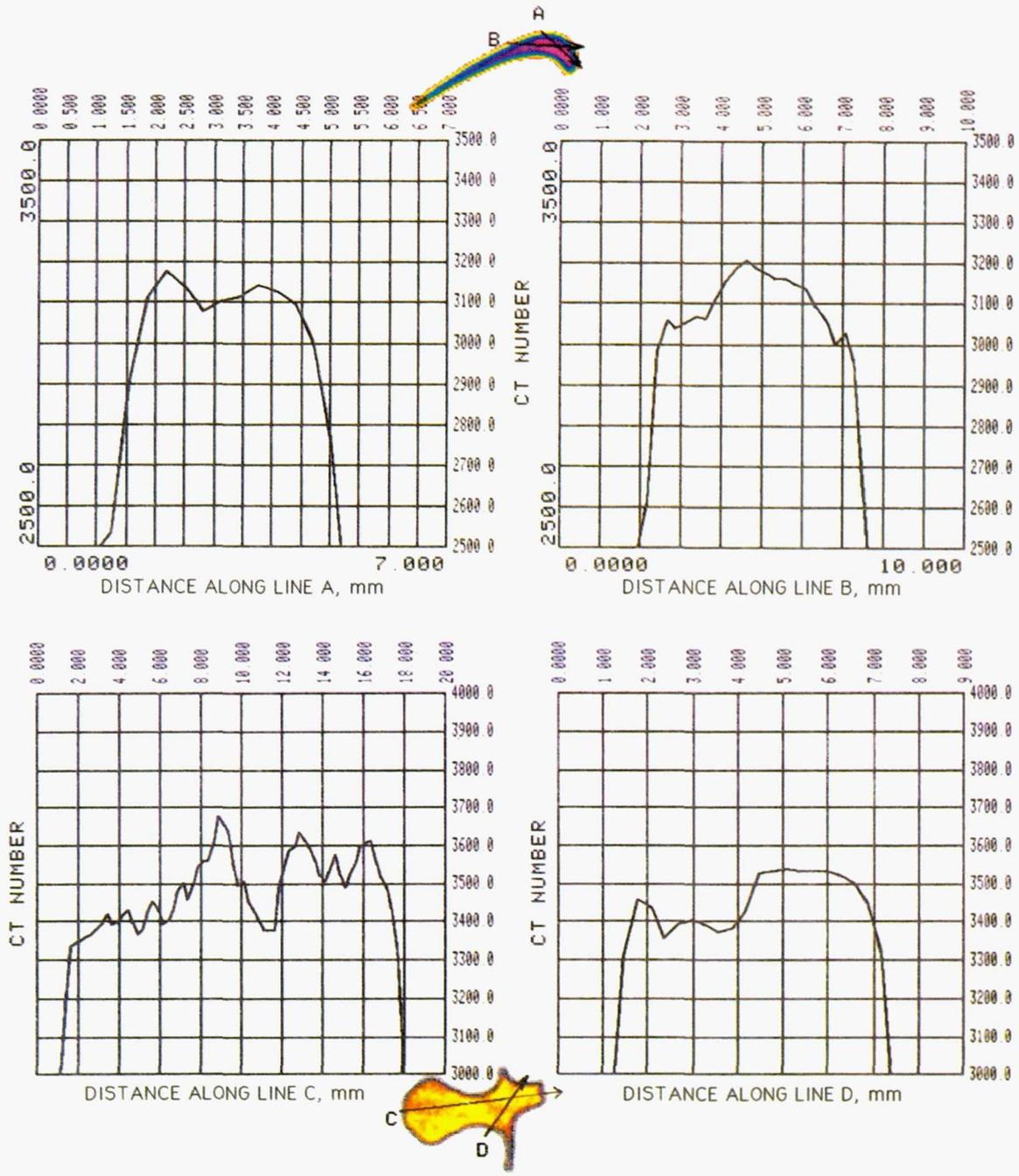
Figure 4.17.—CT number traces along lines A and B for SN blade S1 and along lines C and D for SN blade S2.

More
dense

Less
dense
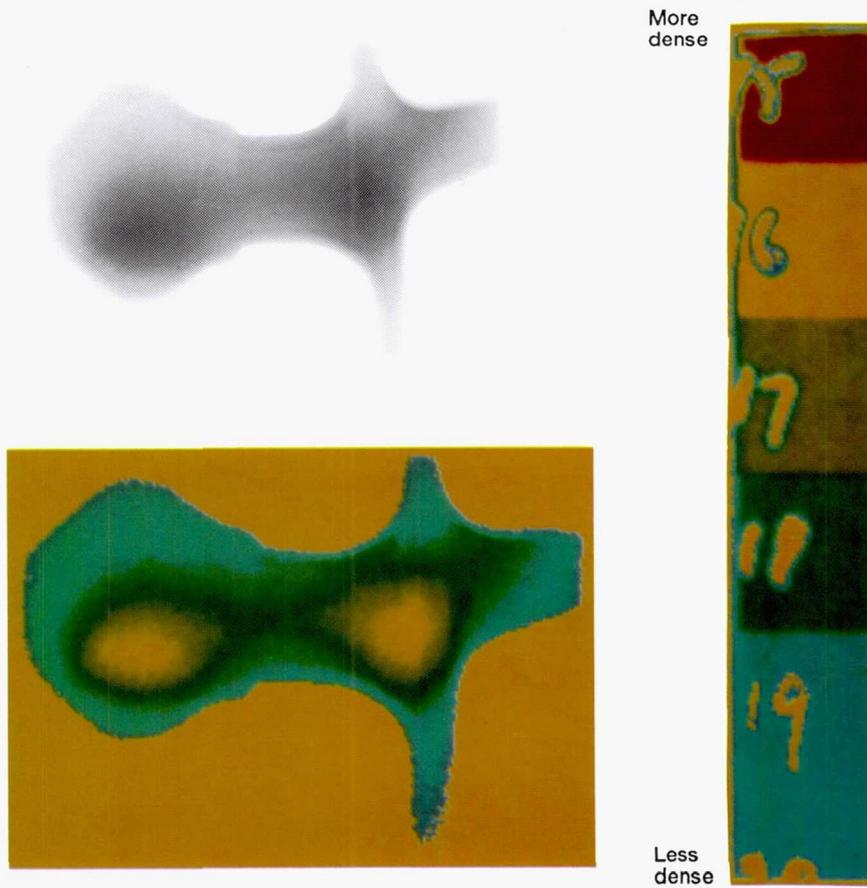
Figure 4.18.—Radiographic images of cross-sectional slice SN blade S2.

Less dense

More dense
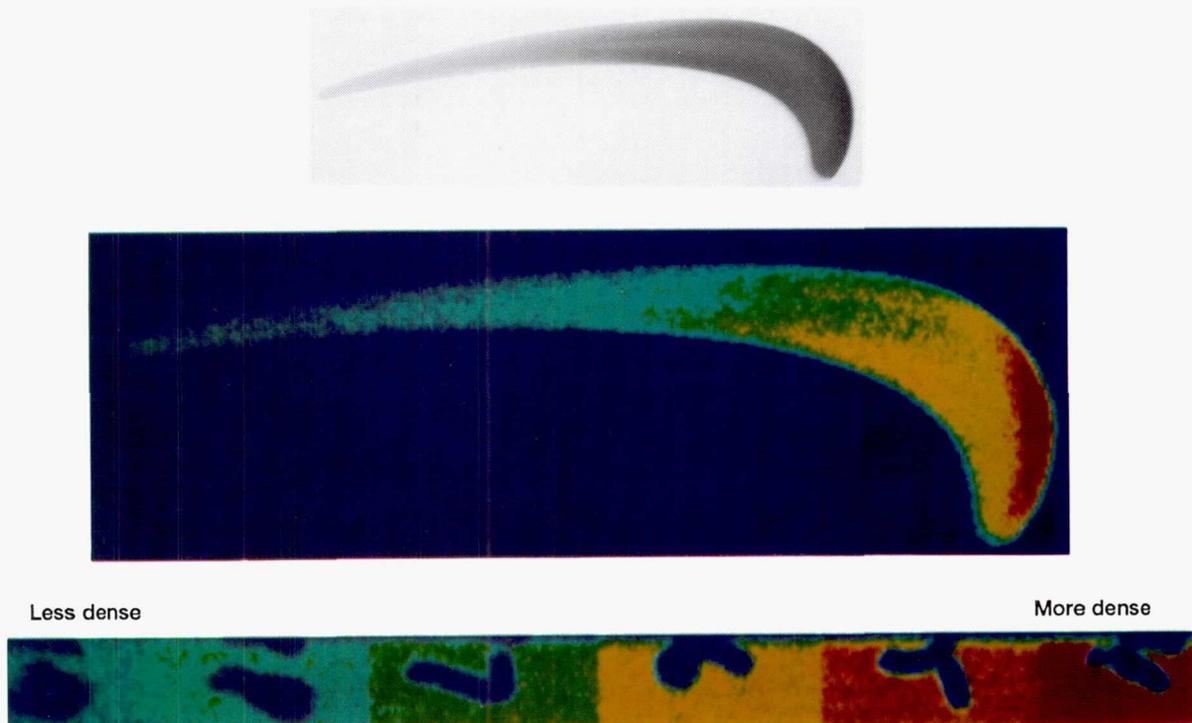
Figure 4.19.—Radiographic images of cross-sectional slice SN blade S1.
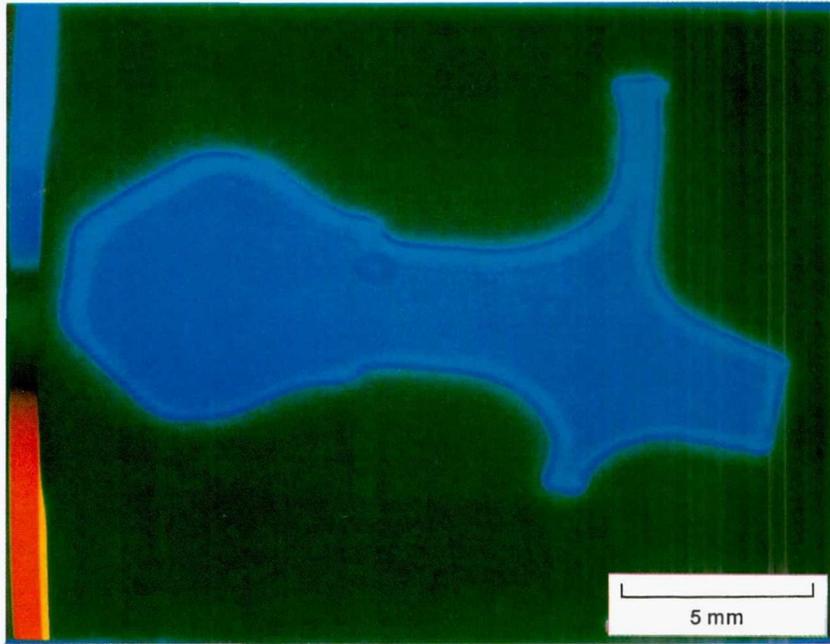
(a) SN blade S2.
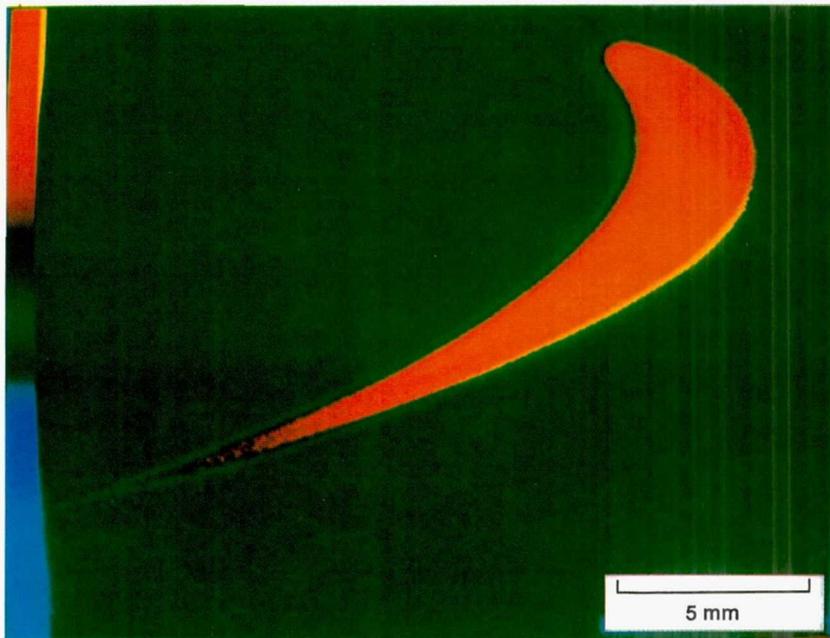
(b) SN blade S1.

Figure 4.20.—Subsurface scanning acoustic microscopy images.
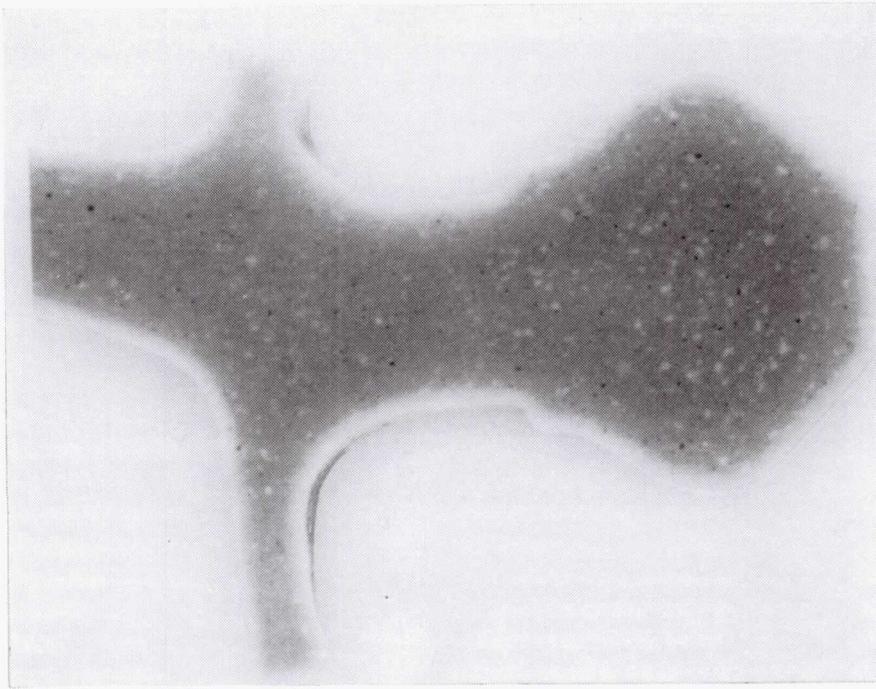
Figure 4.21.—Low-magnification optical photograph of polished surface of SN blade S2.
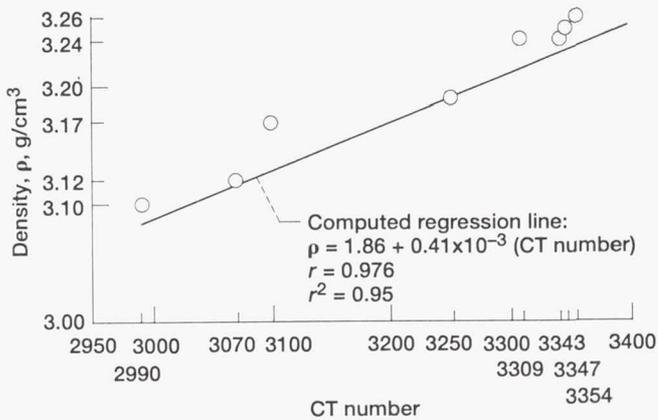
Figure 4.22.—Density versus CT number for monolithic Si_3N_4 and SiC ceramics.

Computed regression line:
$\rho = 1.86 + 0.41 \times 10^{-3}$ (CT number)
$r = 0.976$
$r^2 = 0.95$

4.4 Conclusions

The capabilities and limitations of x-ray computed tomography for characterizing monolithic ceramics have been established. X-ray computed tomography is a viable technique for characterizing a relatively medium-size component with a relatively simple geometric shape. Tomographic data do provide the information needed to deduce material densities on a volumetric basis. These tomographic findings were corroborated by radiographic, ultrasonic, and light microscopy data.

Chapter 5

Characterization of MMC Subscale Engine Components by X-Ray Computed Tomography

5.1 Introduction

Manufacturing high-temperature generic engine components requires concurrent development of new and innovative nondestructive evaluation technologies and parallel upgrading of existing NDE modalities. However, NDE technologies for characterizing newly developing high-temperature composite engine components face many challenging constraints. An NDE technique must be able to characterize components that have thin and thick parts, complex material systems (e.g., multiphase composites), complex geometrical shapes, and complex structural integration. Further, NDE must detect and resolve minute processing flaws, different phases or materials that have almost identical properties, fiber architectures, fiber pullouts, fiber breakages, fiber-matrix debonds, delaminations, splittings, and global and local density variations. In addition, nondestructive materials characterizations should correlate with mechanical or destructive evaluations. Finally, NDE must be standardized for reliable assessments and unambiguous interpretations.

Various NDE techniques have different advantages and limitations. Some are limited to detecting specific types of flaws in certain kinds of materials and components, others are limited to characterizing simple shapes, and most are limited to two-dimensional evaluation of three-dimensional objects. Individual techniques can characterize only a few features that may detrimentally affect the quality and serviceability of a specific component. Tomographic imaging, using a variety of energy sources (e.g., photons, protons, electrons, and phonons) allows three-dimensional NDE. However, x-ray tomographic imaging is the most widely used technique in industrial NDE (Armistead, 1988). X-ray computed tomography(XCT) offers distinct advantages over conventional NDE in the realm of three-dimensional detection and sizing of internal defects and anomalies. XCT can quantitatively determine volumetric variations of the CT number in successive transverse cross-sectional images (Berland, 1987;

Kak and Slaney, 1988). Comparing these cross-sectional images provides three-dimensional representation of the internal structure. The CT number represents the x-ray linear attenuation coefficient of a volume element (voxel). The x-ray linear attenuation coefficient is affected by the elemental composition and density of the material in a voxel. Comparing these cross-sectional images provides a three-dimensional representation of how internal structures, on the basis of their atomic numbers, sizes, and mass densities attenuate x-ray energies.

In this work the capabilities and limitations of XCT for characterizing metal matrix composite (MMC) specimens and subscale engine components are defined. A data base of spatial density information that can be incorporated in geometric modeling of composite constituents and consequent finite element modeling of composite stiffnesses is provided.

5.2 Materials and Experimental Systems

A subscale integrally bladed rotor (fig. 5.1(b)) and light-weight engine structures rod (fig. 5.1(a)) and ring, all made from a pedigreed SiC-fiber-reinforced beta titanium (alloy C) composite, were evaluated in this study.[10] Three additional rings (R_1, R_2, and R_3) are evaluated here. The rod and the rings were consolidated by hot isostatic pressing (HIP) using ribbon-wrapped-fiber technology, and the rotor was consolidated by vacuum hot pressing (VHP) using powder-coated-fiber technology. The rod, the rotor, and the ring are being considered for MMC gas turbine engine applications (fig. 5.2).

The experimental steps were as follows: A support rod and subscale components were initially evaluated by using XCT. Transverse cross sections were extracted and polished from the rod after it was tensile tested, from the ring after it

---

[10]Pratt & Whitney supplied the hardware.

(a) Support rods.
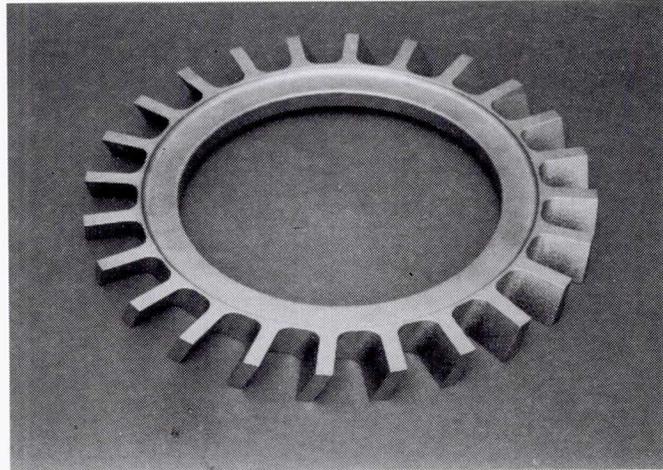
(b) Rotor subelement.

Figure 5.1.—SiC-fiber-reinforced beta titanium rods and rotor subelement.
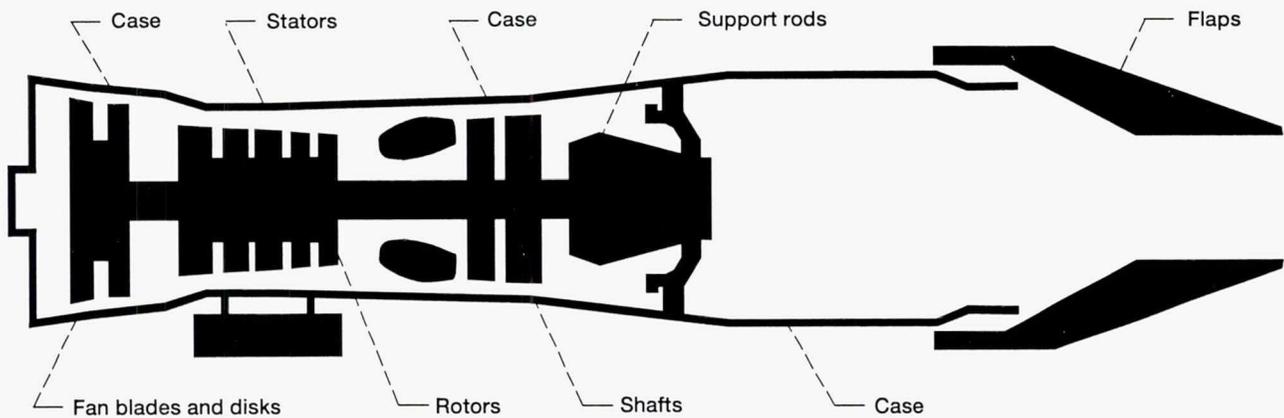
Figure 5.2.—Potential applications for titanium matrix composites in gas turbine engines.

was burst tested, and from the rotor. All these slices were metallographically evaluated and their immersion densities were measured. Each slice was radiographically evaluated. The radiographic results were then compared with metallographic and XCT slice information. Finally, the density data were correlated with CT number data for each slice.

The XCT system described in chapter 4 was used to evaluate these subscale engine components. The CT slice thickness was 2 mm, the image pixel size was 250 μm, the pixel integration time was 55 msec, and the total scan time per slice was 20 to 30 min.

A conventional radiography system (400-μm focal spot size) with high-energy capability (up to 3.2 kW) was used to comparatively evaluate the ring, and a microfocus system (10-μm focal spot size) with low energy (up to 10 W) was also used to comparatively evaluate actual cross-sectional slices.

5.3 Results and Discussion

5.3.1 Supporting Rod

XCT evaluation of a supporting rod consisted of scanning it at different locations as shown in figure 5.3. Transverse cross-sectional CT slices (in the horizontal direction) A to F exhibit the CT number variation within these cross sections as depicted by the change in pseudocolors or in grayness. XCT images detected unintended eccentricity between the composite core and case. Higher CT numbers (blue to dark blue or darker gray) correspond to the case area, whereas lower CT numbers (red to yellow or lighter gray to white) correspond to the core area of the composite slices. Variations in CT numbers along specified directions (e.g., bb, dd, and ff) are shown in figure 5.3. The CT number changed by 9 percentage points (from 98 percent to 89 percent) from the
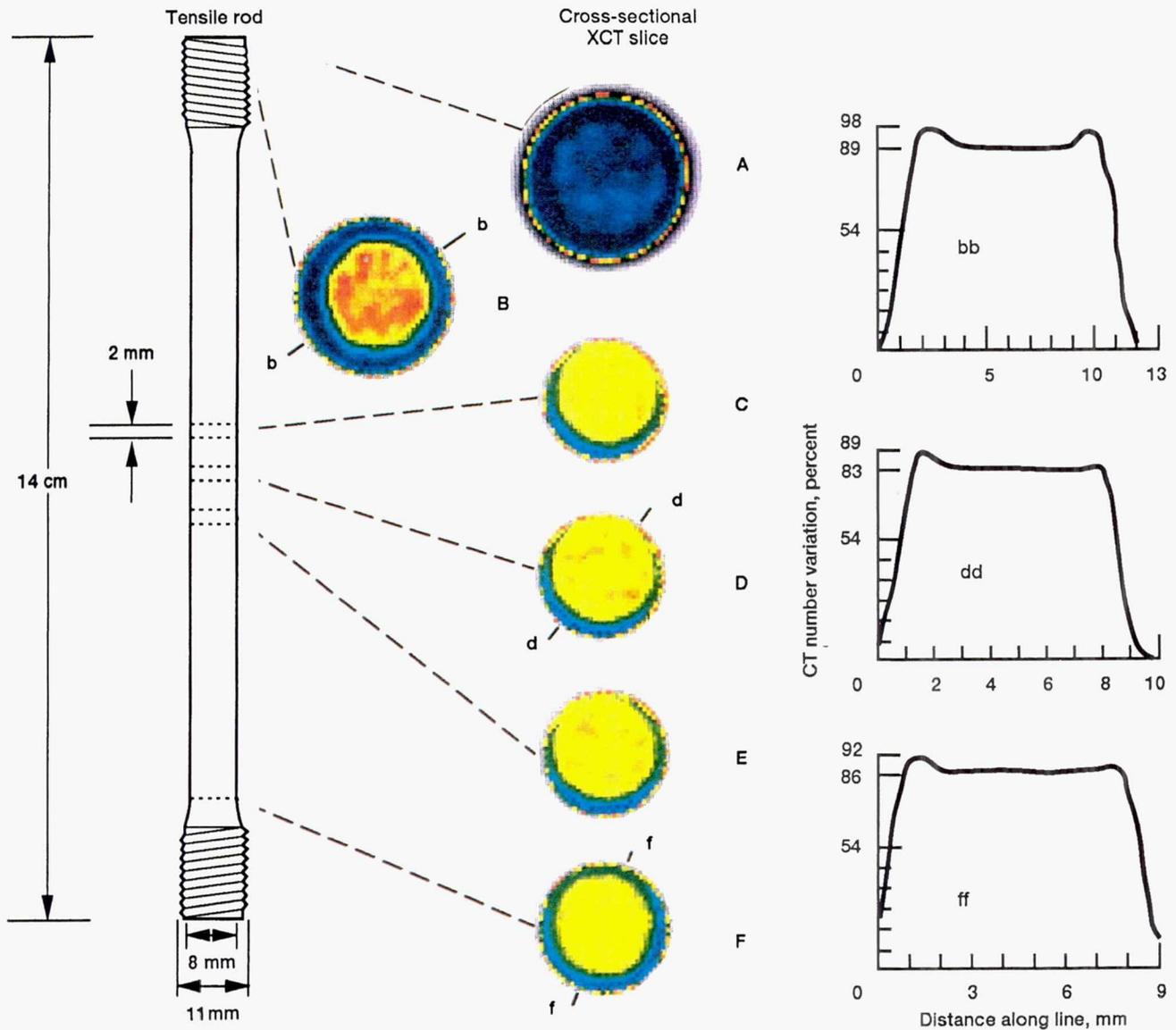
Figure 5.3.—X-ray computed tomography of MMC tensile rod.

case to the core of the composite in slice B, and by 6 percentage points in slices D (from 89 percent to 83 percent) and F (from 92 percent to 86 percent). This was expected because the case is a higher x-ray absorptive titanium-base material than the composite core, which includes mainly SiC fibers. Furthermore, in comparing slices B, F, and D it is obvious that the CT numbers for the core decreased from B to F to D, indicating nonhomogeneous consolidation in the vertical direction. The cladding in slice B is of higher CT number (98 percent) than that in slices D (89 percent), and F (92 percent). This is due to the geometry of the rod: The higher CT number sections were machined off in slices away from the threaded region. Slice A shows that no fibers or only a small number of fibers tips were present in the last 2-mm slice at the end of the rod.

Data from every voxel enable the computation of the average CT number of any region of interest to include the whole slice area as shown in the third row of figure 5.4. Row four in figure 5.4 shows the immersion densities of slices B, F, and D. These densities show a similar trend toward the average CT number for the three slices. However, the average CT number for slice B was not close to its density value. The x-ray scatter off the edges of the slice made its average CT number smaller than expected because the material that is not accounted for is of high CT number (i.e., beta titanium case material).

Figure 5.4 also shows the microfocus radiographs of actual slices taken from the XCT regions B, F, and D. These through-the-thickness x-ray attenuation radiographs accentuate the fiber distribution and average density variations

47

	B	F	D	
Images of XCT slices in rod A7				CT number
				5549
			2 mm	
Radiographs of actual slices	B	F	D	1 mm
Average CT number	4888	4829	4670	3250
Density (immersion) of actual slices, g/cm^3	5.20	4.91	4.88	
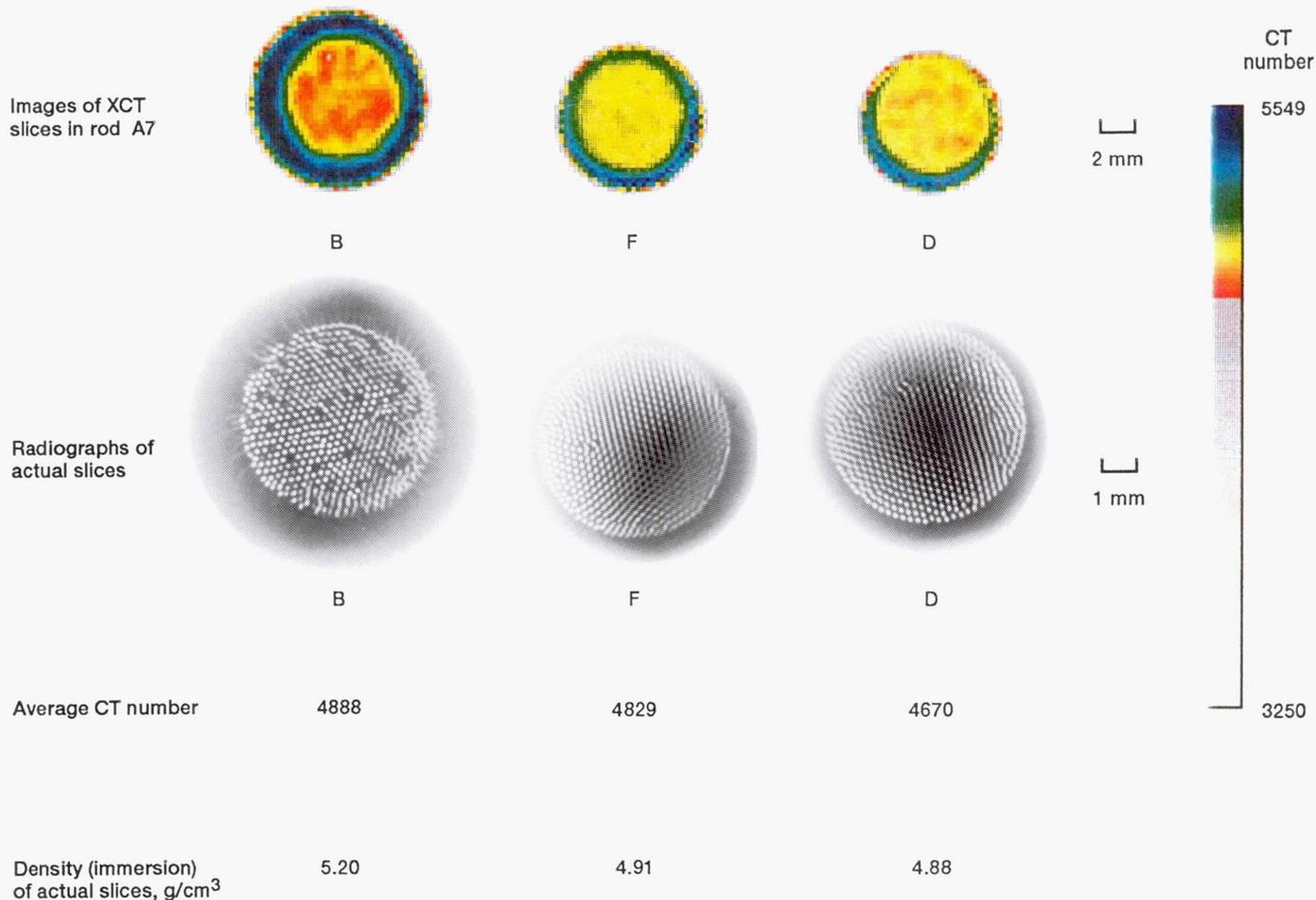
Figure 5.4.—Detailed information on actual slices from rod.

within each cross section. These are affected by (1) the degree of flatness and parallelism of the slices, which affected the through-the-thickness average density variation measurements, and (2) by the scatter off the edge of the cladding. Therefore, XCT has an advantage over microfocus radiography (i.e., even with a high-resolution radiographic system tedious sample preparation is still needed before good representative information can be obtained).

Figure 5.5 shows optical micrographs of slice B as etched and an energy-dispersive analysis x ray (EDAX) of slice D. Micrographs of polished and etched slices show that the porosity is minute. The presence of titanium-rich particles at the grain boundaries is evident, as shown in the backscattered electron (BSE) image of part of slice D and as demonstrated in comparing the energy spectrums between particle and matrix (fig. 5.5).

5.3.2 SCS–6/Alloy C Ring

Figure 5.6 shows a through-the-thickness conventional radiograph of the ring and four XCT slices. Conventional radiography shows a thinner case toward the inside diameter (ID) than toward the outside diameter (OD). Conventional radiography also shows the superimposed density variations within the composite core. Similarly, the four XCT slices show a smaller case on the ID side than on the OD side but also detail the density variations within each slice. XCT slices detected the presence of a protruding cusp in the core located near the top side and toward the ID of the ring. The core of the composite was intended to be rectangular, uniform, and equally distant from all edges. Figure 5.7 shows a magnified image of CT number variations in the slice taken at 110° and the CT number variations in percent along lines aa and bb. There was a 10-percentage-point change in the CT number between the case and the core of the ring, and a 3- to 4-percentage-point change within the composite core.

CT artifacts were not detected in the XCT slices of the rod and the ring because they had simple circular and rectangular shapes.

BSE image from slice D

5 μm

Particle
Slice D

Ti

V

Matrix
Slice D

Ti

V

Cr

Cr

Counts

10 000

8 000

6 000

4 000

2 000

0

Energy, keV

0   2   4   6

Slice B

50 μm

Slice B

1 mm
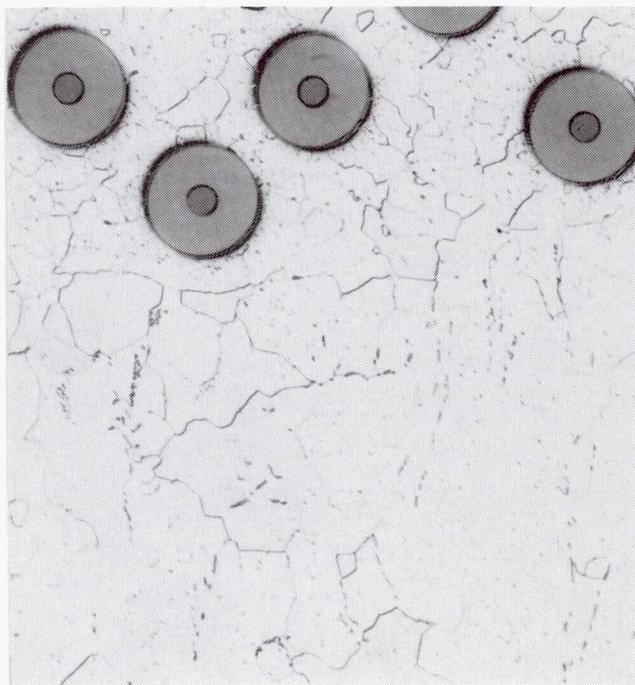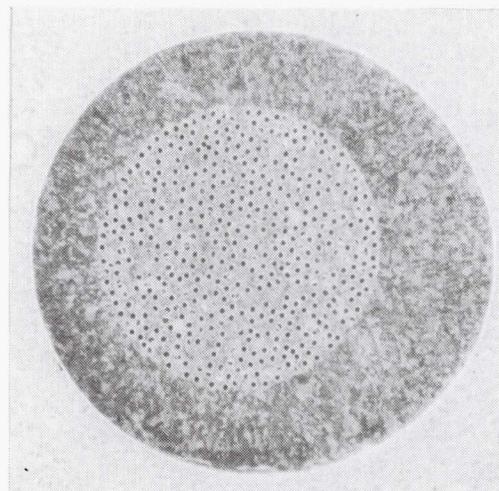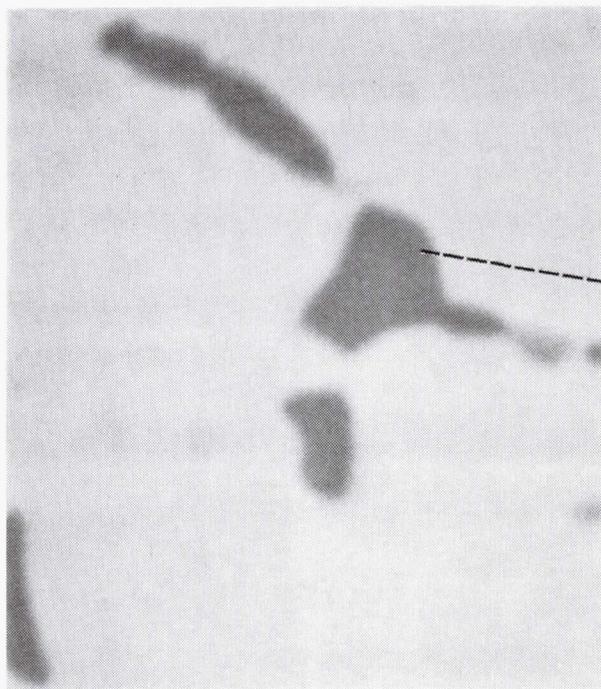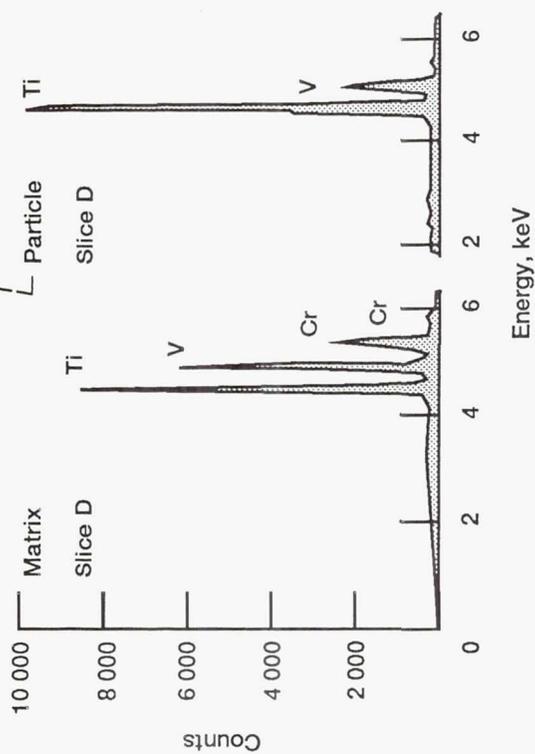
Figure 5.5.—Micrographs of slice B and BSE and EDAX of slice D.

49
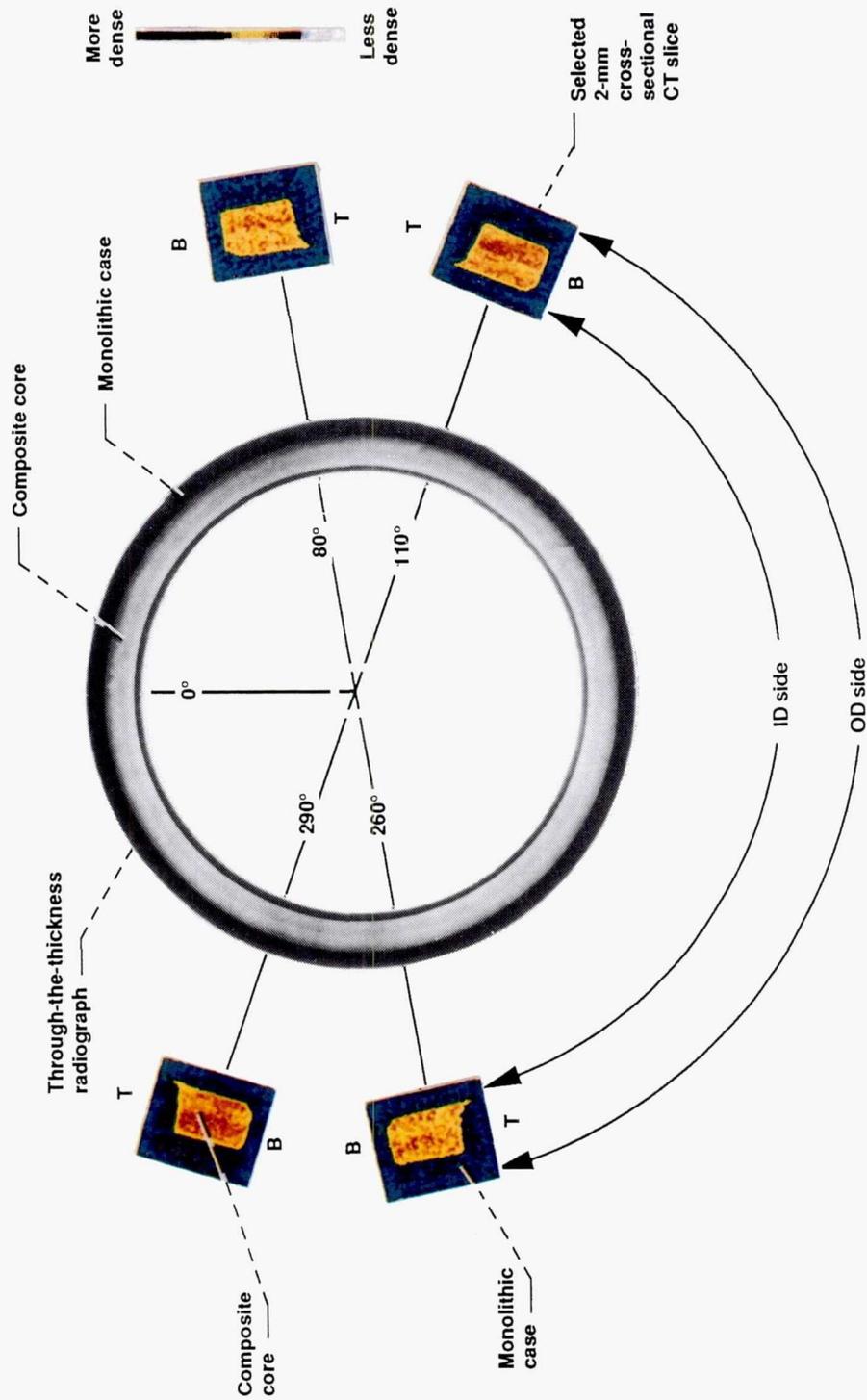
Figure 5.6.—X-radiography and x-ray computed tomography of MMC ring LES–3. (Annulus dimensions: outside diameter, 185 mm; inside diameter, 140 mm; thickness, 26 mm. Annulus material, SCS–6/alloy C composite. T is top side; B is bottom side.)
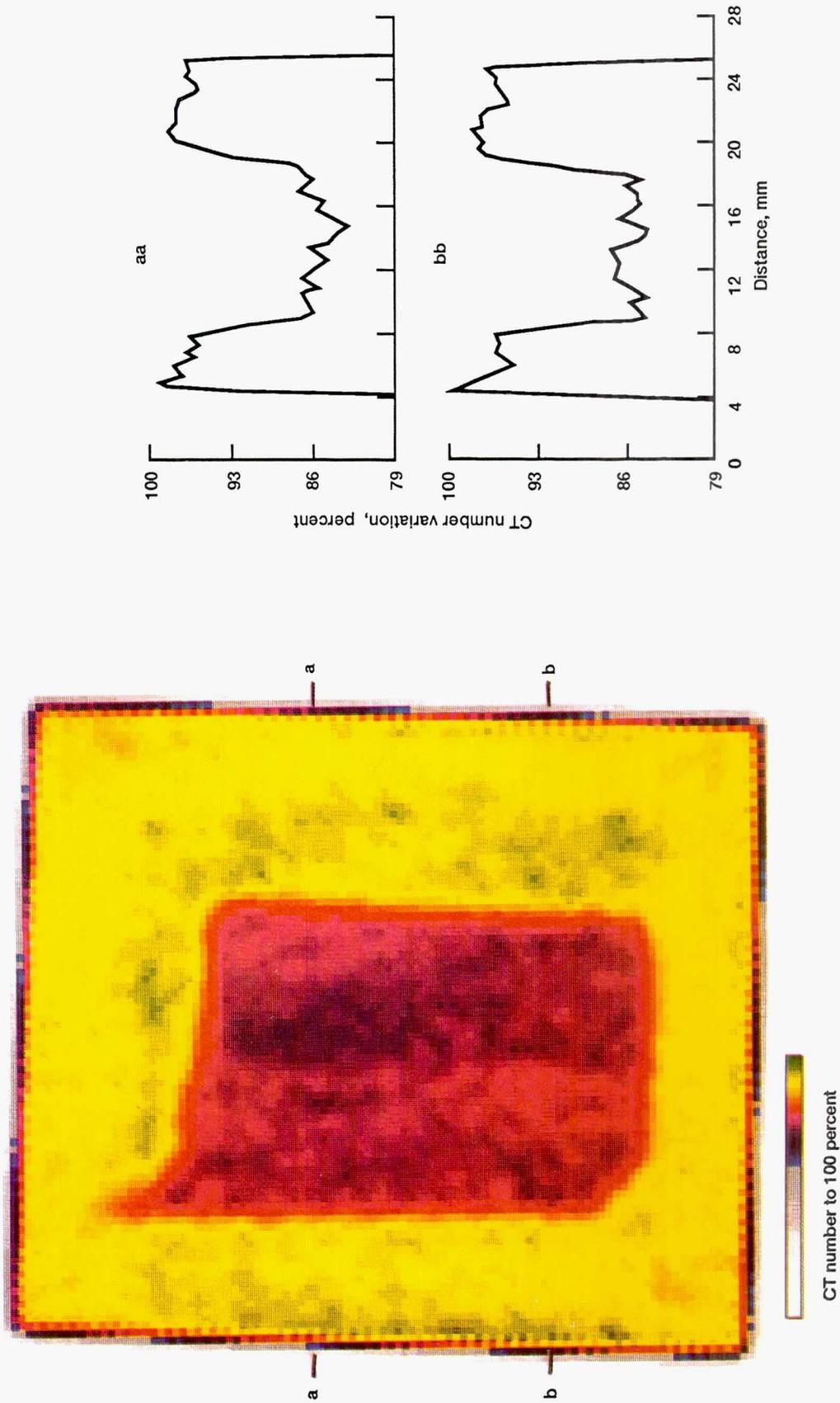
Figure 5.7—CT number variations in CT slice at 110° from MMC ring.

CT number to 100 percent

5.3.3 SCS–6/Ti-15-3 Rings

Figures 5.8 and 5.9 show through-the-thickness conventional radiographs of rings R2 and R3 along with selected XCT slices. Conventional radiography shows a thinner cladding toward the ID than toward the OD of ring R2. Similarly, the four XCT slices show a smaller cladding on the ID side than on the OD side and detail the density variations within each slice. Conventional radiography also shows the density variations within the composite core and features the presence of sizable low-density anomalies, such as the one highlighted in figure 5.8 before the 120° marker.

XCT slices in figures 5.8 and 5.9 depict the presence of a protruding cusp in the core that is located near the top side and toward the ID of the ring. XCT slices further demonstrate the presence of lower fiber volume fraction, poor consolidation, or both in the core area toward the OD side than toward the ID side. The core of the composite was supposed to be rectangular, uniform, and surrounded by uniform cladding.

Figure 5.10 shows a magnified image of XCT density variations in a slice of ring R1 before testing. The density variations along line AA show a 10-percentage-point change between the case and the core of the ring and a

3-percentage-point change within the composite core. Figure 5.10 reveals the processing or consolidation problems that resulted in the protruding cusp seen previously in rings R2 and R3. The horizontal light band (yellow) in the core section indicates a manufacturing flaw (i.e., a missing fiber layer).

Figure 5.11 shows radiographs of ring R2 before and after the burst test with different magnifications in order to compare results on the same figure. XCT slices before (A and D) and after (B and C) the burst test at approximately the same locations are also shown in the figure. One location was near the burst area (i.e., the primary fracture area); and the other was near the secondary fracture area that is located diametrically opposite to it. Radiography of ring R2 before testing detected a defect condition that may have led to the primary failure because the location of that defect coincided with the location of the primary fracture. The defect has a low radiographic density, which may indicate poor consolidation in the composite core and poor cladding/composite interface bonding. Radiography also shows poor consolidation, higher fiber volume fraction, or both in the OD side of the core before and after testing. A defect appears in the radiograph taken after testing. This type of defect was also found with ultrasonics. Characterizing defects, the difference in the degree
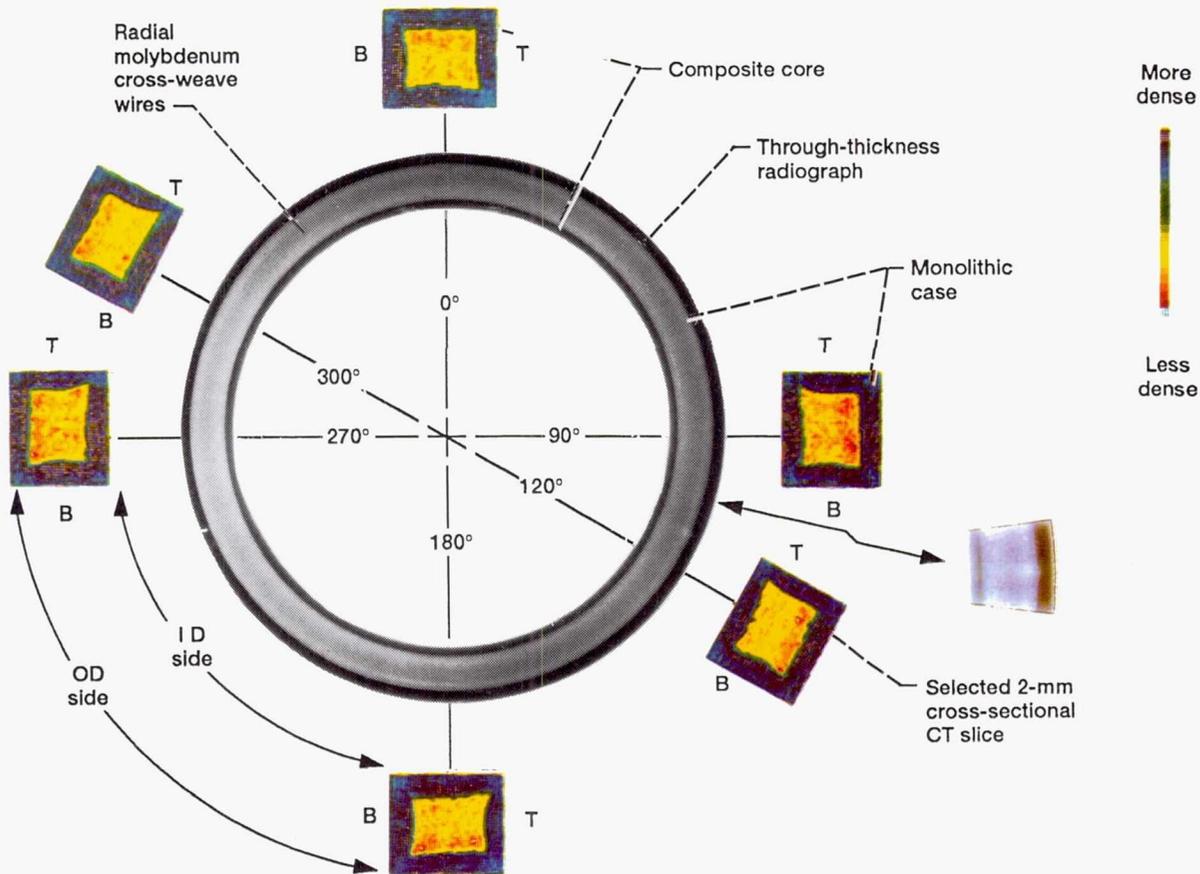
Figure 5.8.—Radiography and x-ray computed tomography of ring R2. (Annulus dimensions: outside diameter, 171 mm; inside diameter, 133 mm; thickness, 24 mm. Annulus materials, SCS–6/Ti-15V-3Cr-3Al-3Sn. T is top side; B is bottom side.)
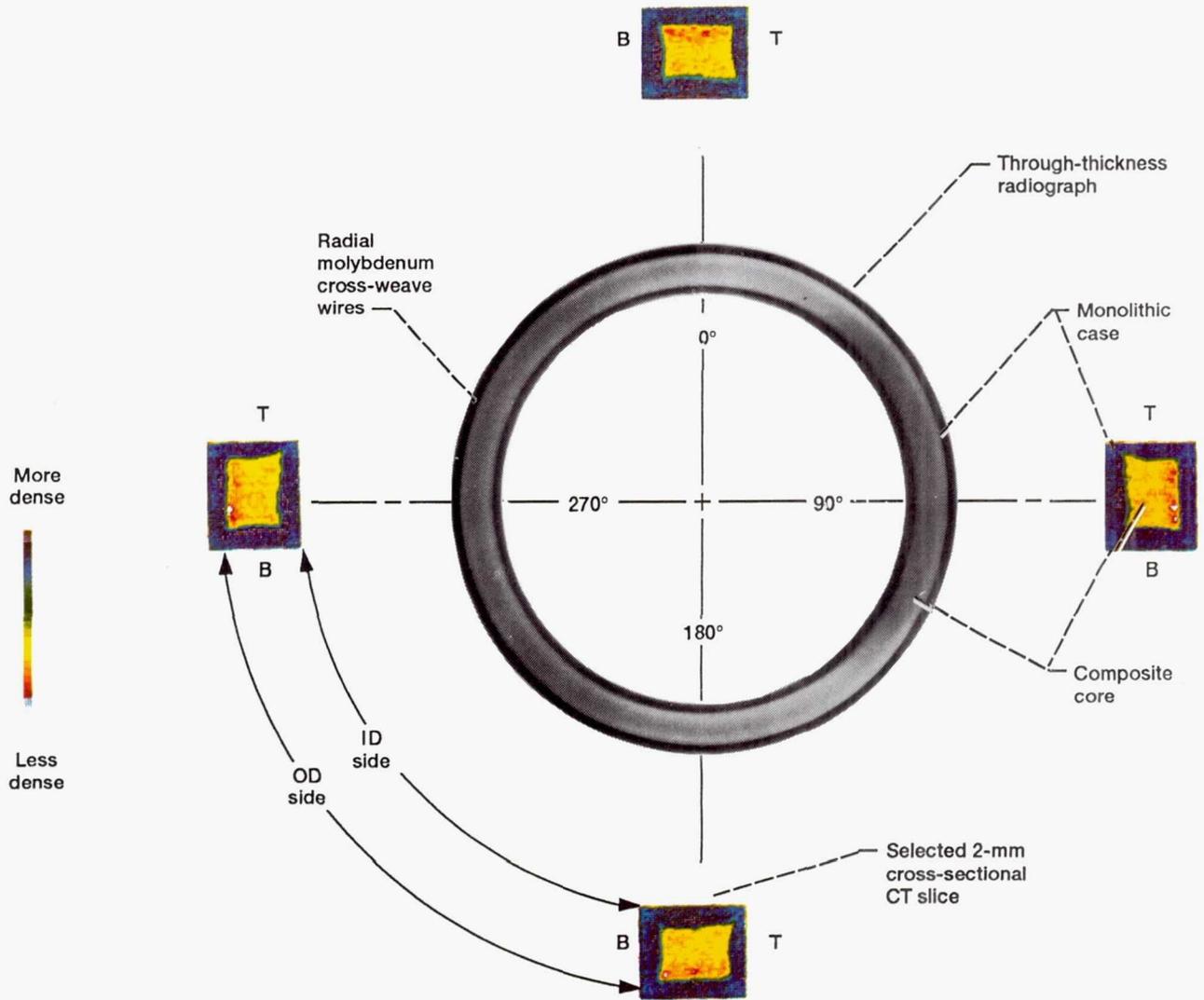
Figure 5.9.—Radiography and x-ray computed tomography of ring R3. (Annulus dimensions: outside diameter, 171 mm; inside diameter, 133 mm; thickness, 24 mm. Annulus materials, SCS–6/Ti-15V-3Cr-3Al-3Sn. T is top side; B is bottom side.)
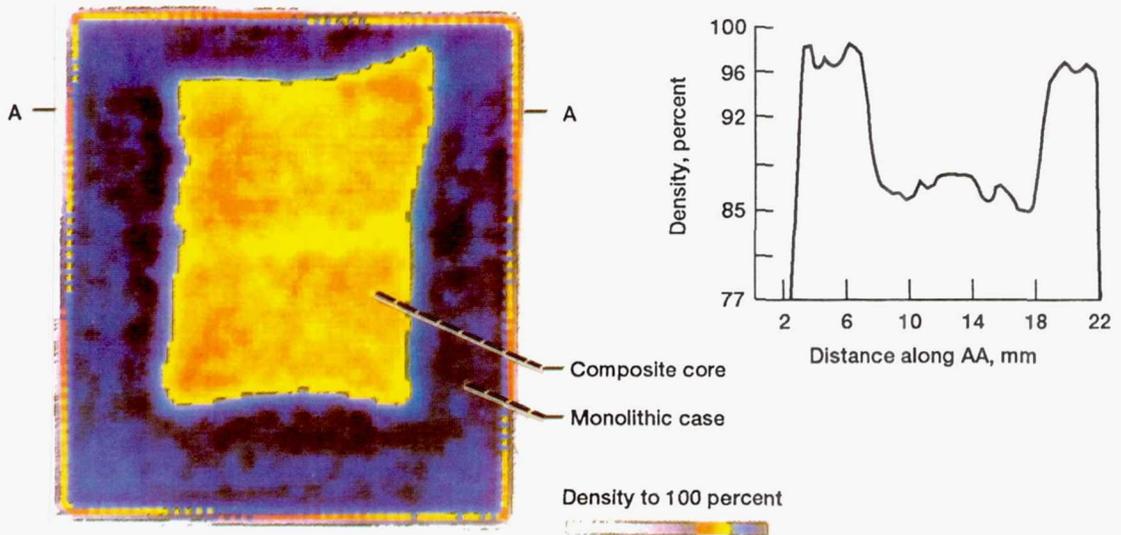

Figure 5.10.—Tomography results of a selected cross section from ring R1.
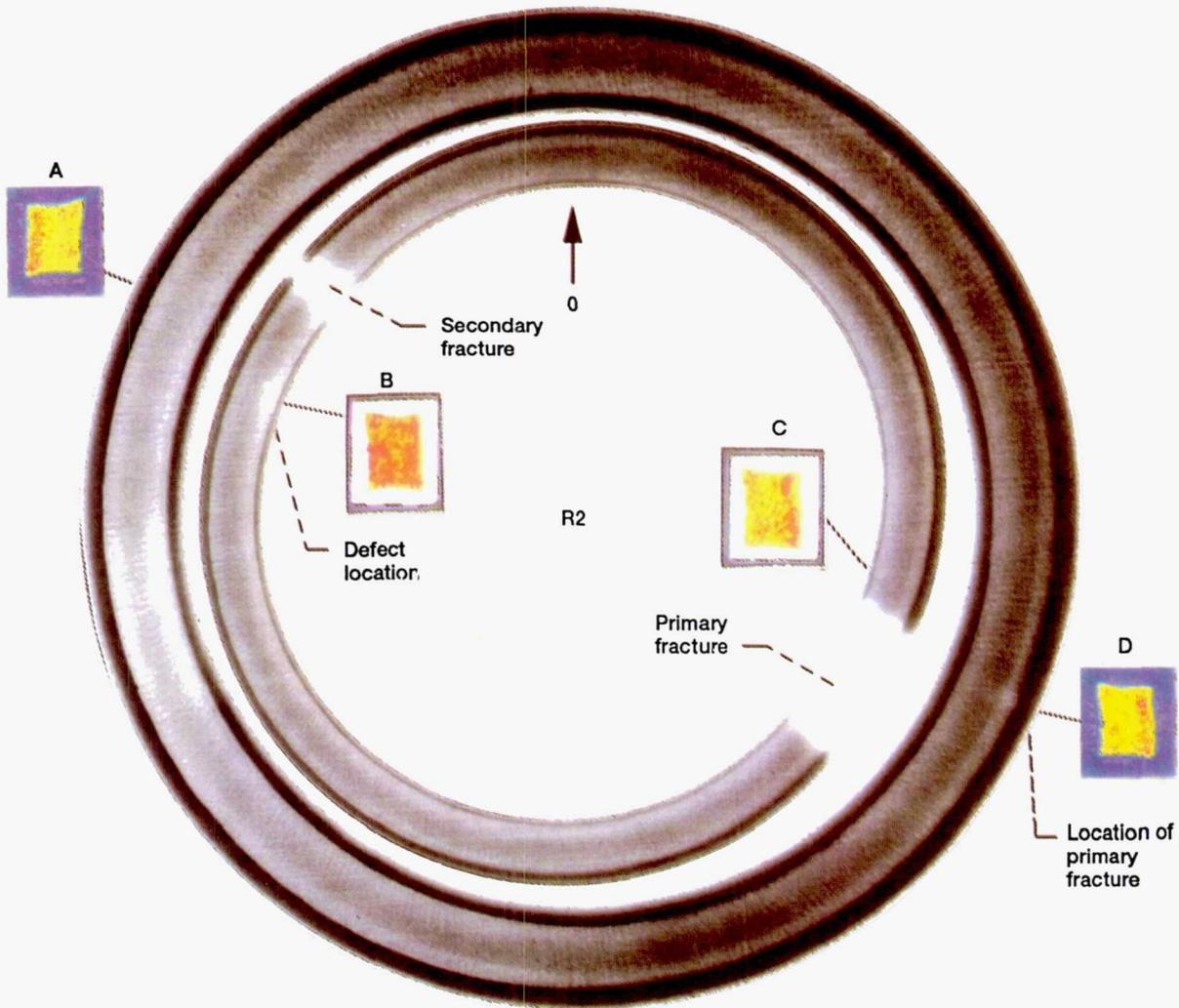
Figure 5.11.—Radiography and selected x-ray tomographic slices of ring R2 before and after burst test.

of damage that is seen between XCT slices B and C, and the damage evolution that is seen between slices A and B and C and D will require more work. Future work will correlate most NDE findings with detailed metallographic characterization.

5.3.4 SCS–6/Alloy C Rotor

A transverse axial cross-sectional XCT slice of the subscale integrally bladed rotor is shown in the center of figure 5.12 (fig. 5.1 is the optical photograph). Also shown are four XCT slices taken perpendicular to the circumferential direction roughly midway between two adjacent blades. The streaks in the transverse axial slice demonstrate photon starvation problems (i.e., few x rays are reaching the detector after being attenuated by the material along the x-ray path lengths). After taking a scan through two diametrically opposite blades, where the x-ray path in the material was on the order of 3.5 in., it was concluded that this path length is a limiting factor for XCT scanning of this material. The four XCT

transverse-to-circumference slices depict a deviation from the rectangular shape of the core to an almost "fingerprint" representation of each slice. These four slices demonstrate the presence of CT number variations within the core as well as within the cladding regions.

Comparing XCT data with radiographic data of slice B (fig. 5.13) shows that the CT number variations within the core were mainly due to the degree of fiber concentration. Greater fiber concentrations are depicted by darker colors. Also shown in figure 5.9 as well as in figure 5.8 is an area of low CT numbers closer to the outside edge and in the two protruding edges of all four XCT slices. However, metallographic examination of all four slices did not show porosity, low density, or particle concentration in these low-CT-number areas. Figure 5.14 indicates that a minute amount of porosity existed in the composite core near its boundary with the cladding. Furthermore, figure 5.15 displays the presence of titanium-rich particles that are more concentrated in the core areas than in the cladding areas. Consequently, the
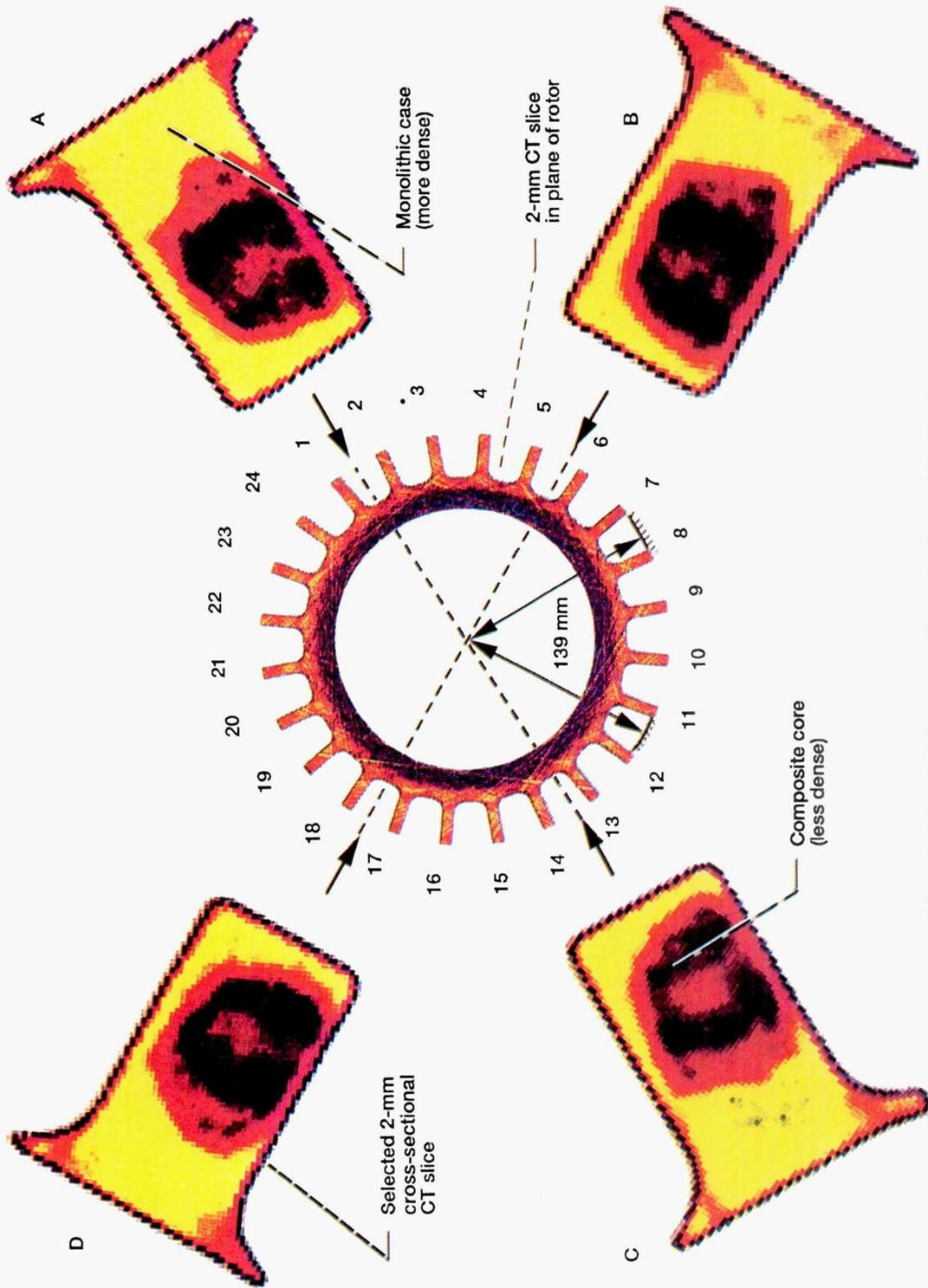
Figure 5.12.—XCT of subscale integrally bladed MMC rotor.

55

Low-CT-number area —

CT number

1750 [========] 5625

⊔ 1 mm

⊔ 1 mm
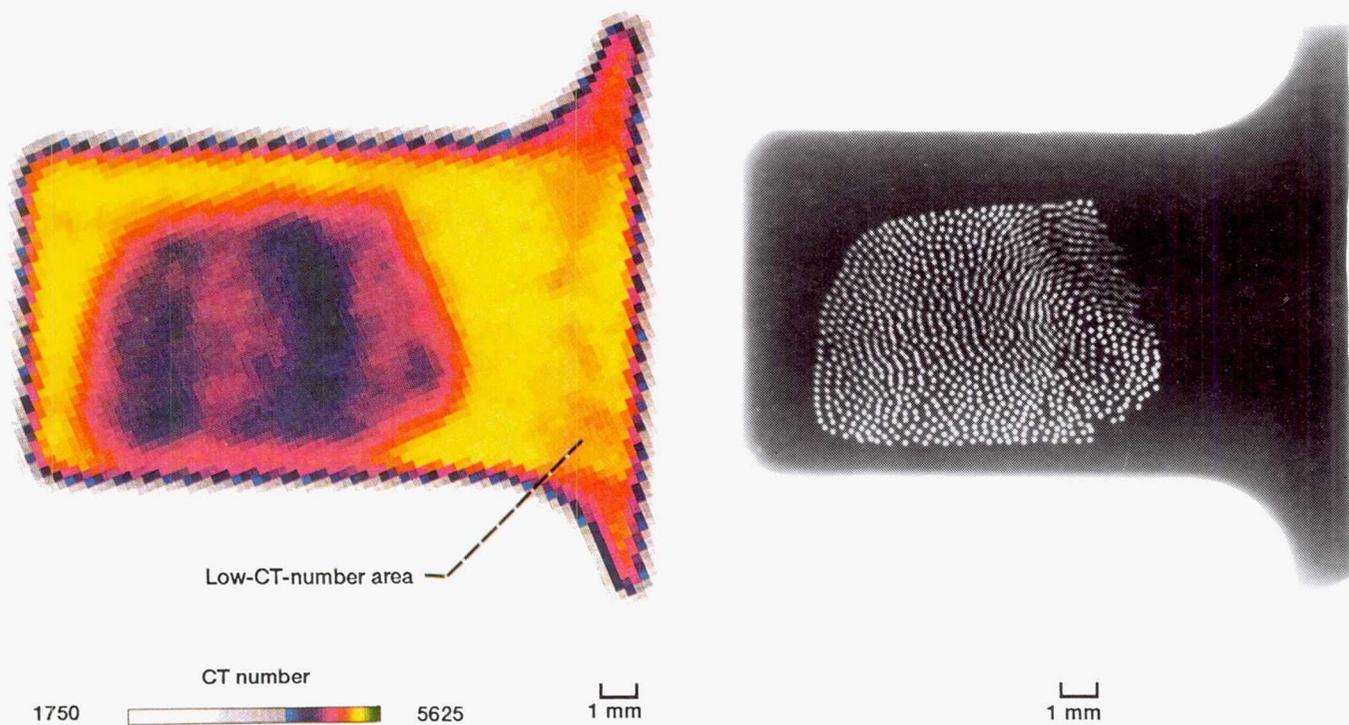
Figure 5.13.—XCT images highlighting degree of fiber concentrations.

⊔ 1 mm

⊔ 50 μm
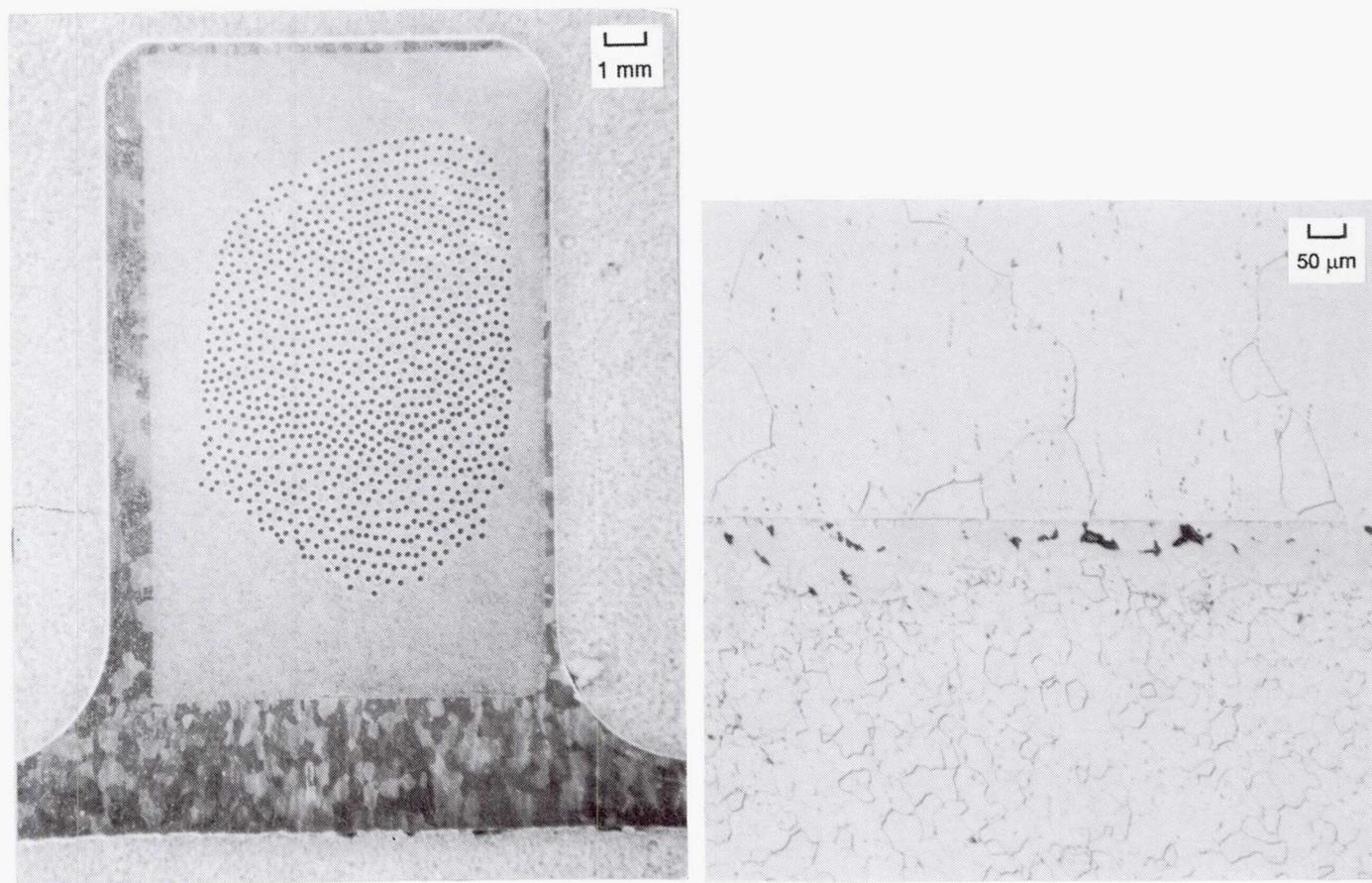
Figure 5.14.—Optical micrographs of slice D from MMC rotor.
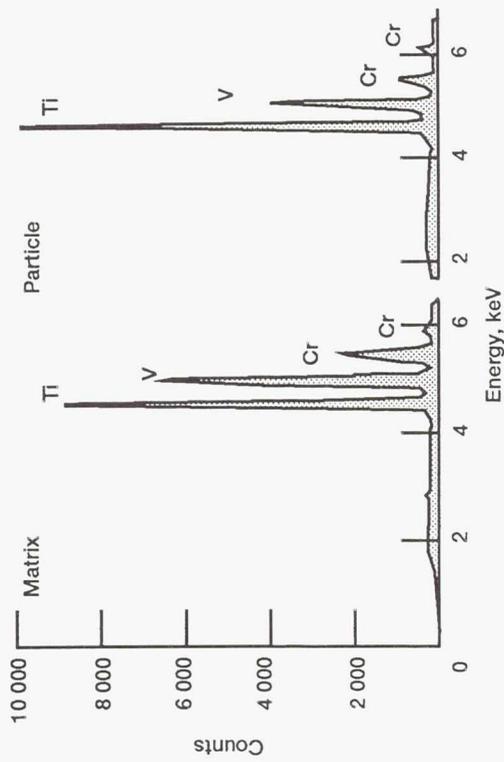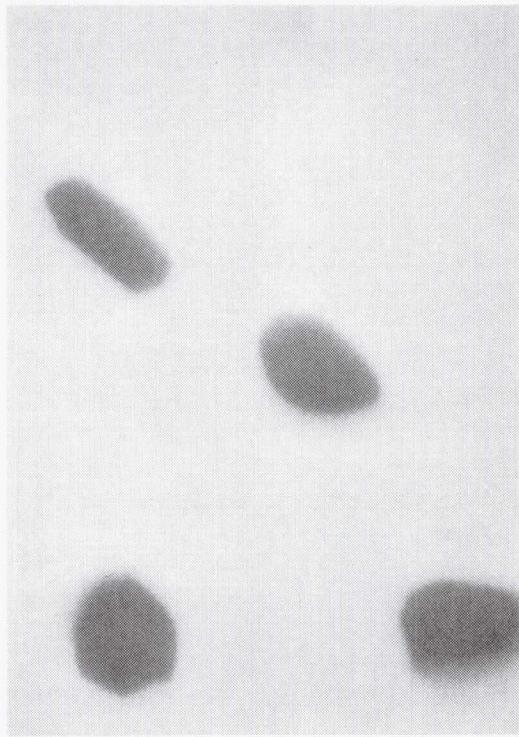
BSE cladding image

Figure 5.15.—BSE images and EDAX results from slice C of MMC rotor.

	CT number	Density, g/cm^3 (immersion)
Slice B	[a]5009	5.10
Section I	[b]4718	4.83
Section II	[b]5263	5.29
Section III	[c]5222	5.40

[a]Good average density measurement.
[b]Good density measurement away from artifact area.
[c]CT artifacts due to object geometry and reconstruction algorithms.
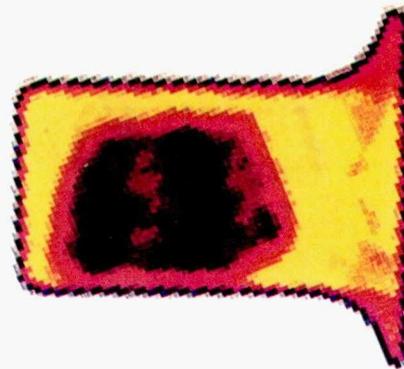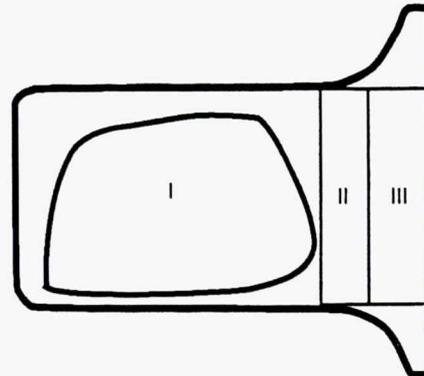
Figure 5.16.—CT numbers and immersion density measurements of different sections in slice B from MMC rotor.

subsequent CT number variations are XCT reconstruction artifacts that were due to the protruding small sections in the rotor slices combined with the translate-rotate scanning system geometry. These XCT artifacts were not detected in the XCT slices of the rod and the ring because of their simple shapes.

Slice B was further sectioned as shown in figure 5.16 and the immersion density was measured on sections I, II, and III. Density measurements correlated with optical characterization (i.e., region I was less dense than region II, which in turn was less dense than region III). The average CT numbers for the whole slice and for sections I and II agreed well with the corresponding measured densities, but the CT number for section III predicted poorly the density of that section. This proves that XCT can be used to estimate density for the whole slice and for sections free of CT artifacts.

5.3.5 Density Versus CT Number for SCS–6/Alloy C Composite

The immersion densities of a few slices from the rod and of a few slices and sections from the rotor are plotted in figure 5.17 versus the corresponding computed average CT numbers. Even though the data included some XCT artifacts and in certain cases were partially limited because of x-ray scatter off the edges, this plot shows a correlation between bulk density and CT number for a composite system.
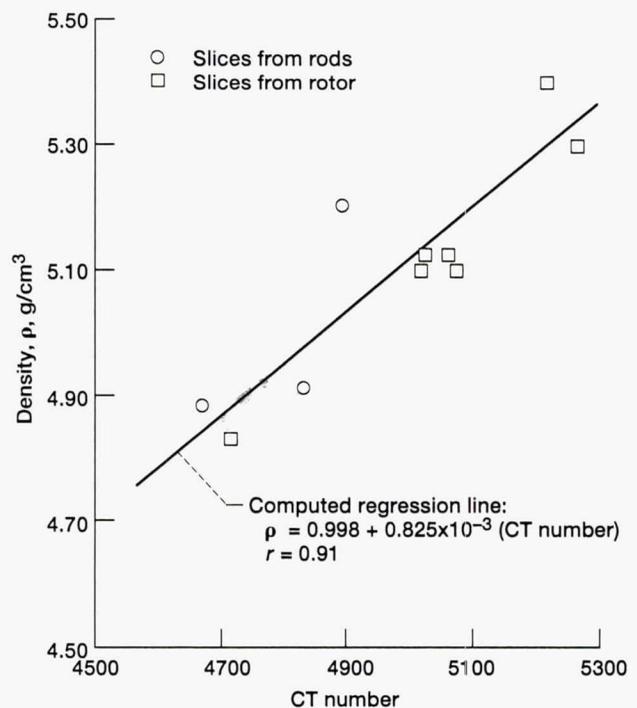
Figure 5.17.—Density versus CT number for SCS–6/alloy C composite.

5.4 General Discussion

XCT information provided to the manufacturer helped identify fabrication and processing problems for different material processes and among different components that were fabricated with similar processes. The CT number variations that were detected within the core region of the rod (less than 1 percent) were much fewer than those within the core region of the ring (3 to 4 percent). This indicates better consolidation in the cylindrical rod than in the annular ring. In order to avoid machining through fibers, as for the rod, the manufacturer now uses XCT images to guide the machining of components to final dimensions.

XCT density information is being recognized as a means for guiding structural design engineers. Distortions in composite constituents, which may cause nonuniform material responses at high temperatures and under different loading conditions, are detected by XCT. Consequently, design and test engineers can concurrently decide whether to continue testing defective components or to section them for detailed evaluation in order to further identify sources of manufacturing problems. NDE coupled with destructive verifications will certainly help to accelerate the improvement of composite components.

Three-dimensional density information on composite components can guide geometric modeling of composite constituents and can also guide composite stiffness modeling where CT artifacts are avoided or minimized. Engineering tomography, which incorporates XCT density information in finite element modeling, can significantly help in predicting the life and serviceability of composite components.

5.5 Conclusions

The capabilities and limitations of x-ray computed tomography for characterizing metal matrix composite subscale engine components have been defined. Examples of spatial density information, which can be incorporated in finite element modeling of composite spatial stiffnesses and in geometric modeling of composite constituents, have been provided. It can be inferred that x-ray computed tomography is a viable technique for accelerating the development of composite components. X-ray computed tomographic imaging can identify problems with manufacturing processes, guide machining of components to final dimensions, and lead structural and design engineers to realistic component life-prediction models.

Page intentionally left blank

Chapter 6

In Situ X-Ray Monitoring

6.1 Introduction

Ceramic matrix composite systems are being developed for heat engine applications (Mah et al., 1987; Heraud and Spriet, 1988; Bhatt, 1988b). The ultimate goal of the current research is understanding composite behavior in order to optimize the composite properties for different hot-section applications. Ceramic matrix composites (CMC's) are being developed because they provide enhanced material toughness while maintaining the useful properties of monolithic ceramics. The fiber-matrix interface in CMC's plays an important role in determining toughness-related properties (Kerans et al., 1989; Evans and Marshall, 1989), but there is little quantitative data on interface properties (Kerans et al., 1989). Furthermore, composite failure processes are not well understood, and verified and validated failure models are lacking.

In order to apply CMC's in critical high-temperature structures, the failure processes and damage tolerances must be understood and the failure analyses and mechanics models must be improved. Methodologies such as in situ x-ray radiography and acoustic emission monitoring clarify failure sequences and damage accumulation processes in composite specimens under loading. The information gathered from in situ monitoring can help in the development and validation of analytical models. Damage and failure mechanisms (e.g., transverse matrix cracking, fiber-matrix debonding, fiber breaking, fiber pullout, and delamination) can be better understood if they are imaged and identified as they occur. Noninvasive in situ examination can help to elucidate the sequence in which these phenomena occur and consequently aid in the identification of controlling factors (i.e., whether they are matrix-dominated properties, fiber-dominated properties, or a combination of both).

The objectives of this study were to demonstrate the capabilities of in situ x-ray radiography for monitoring damage accumulation and failure processes in unidirectionally reinforced SiC/RBSN systems under tensile loading. It will be seen that the methodology can be used to determine the interfacial shear strength between the SiC fiber and the RBSN matrix. This research can improve the interpretation of mechanical test results, the validation of analytical models, the verification of experimental procedures, and the optimization of the fabrication process.

6.2 Experiments

6.2.1 In Situ X-Ray and Materials Testing System

An in situ x-ray and materials testing system (IXMTS) was built in order to conduct in situ x-ray monitoring of materials under tensile loading. Figure 6.1 is a schematic of the experimental apparatus. Figures 6.2 and 6.3 show the IXMTS and details of the specimen testing and evaluation region. The IXMTS combined a 3.2-kW x-ray source and an electromechanical materials testing system.

The x-ray source and generator were capable of reaching a maximum voltage of 160 kV and a maximum current of 45 mA. The x-ray tube had either a 400-μm or a 3-mm focal spot size. Film radiography was chosen as the detection medium because of its high resolution and its registration capabilities. The materials testing system[11] consisted of a 250-kN load frame, a 100-kN electroactuator, a 50-kN load cell, and a digital control system.

All the work described here was done at room temperature. The tensile testing was done in a load control mode for some specimens and in a displacement control mode for others. Loading and displacement rates were 45 N/min and 25 μm/min, respectively. These relatively low rates were used to allow ample time for registering the in situ film radiographic image without holding the load or displacement. The load increment was 111 N or less during the radiographic exposure (25 to 35 sec), except at failure. As the tensile specimen was loaded, the axial strains were monitored by two adhesively bonded strain gauges and a clip-on extensometer. Two x-ray films (to separate film development artifacts

---

[11]Instron Materials Testing System, Canton, MA.
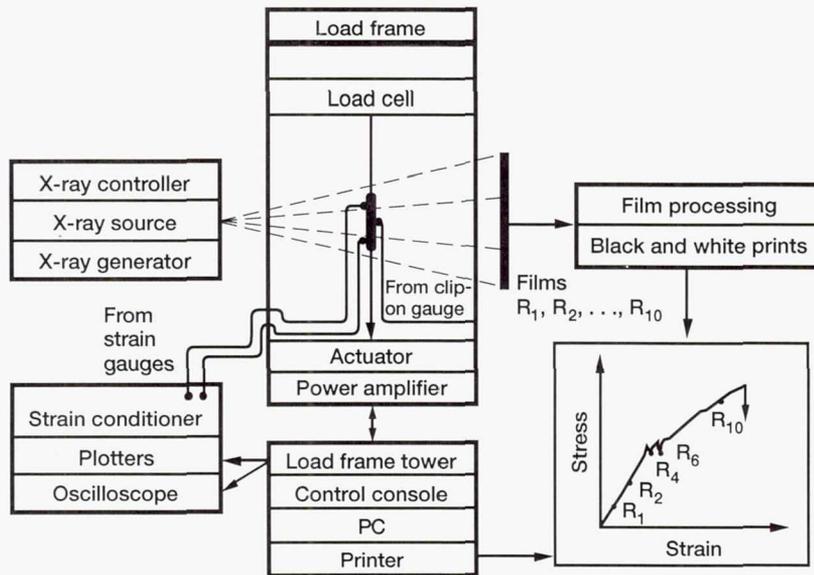
Figure 6.1.—Schematic diagram of in situ x-ray and materials testing system.

from defects in materials) were exposed at different stress-strain levels during the test.

The strain gauges were bonded to the faces of the specimen, and the extensometer was clipped to the edge while leaving the 2.54-cm gauge length accessible to in situ radiography. Immediately after each test the specimen was evaluated with microfocus radiography and optical metallography. The radiographic images were used to interpret the results in conjunction with the stress-strain data.

6.2.2 Radiographic Evaluation

Two different x-ray systems were used: a conventional system with a 400-μm focal spot size and a microfocus system with a 10-μm focal spot size. Conventional radiographs were made in the direct-contact mode (image is 100 percent of object size); microfocus radiographs were made in a projection mode with a resultant magnified radiographic image. In addition to in situ radiography during tensile testing, conventional radiography was used to evaluate silicon powder cloths and composite panels before and after machining. High-resolution microfocus radiography (Baaklini and Roth, 1986a) was used to evaluate the tensile specimens before loading and after failure.

6.2.3 Specimens

The SiC/RBSN $[0]_1$, $[0]_3$, $[0]_5$, and $[0]_8$ composite panels were produced by ceramic powder fabrication methods (Bhatt and Phillips, 1988a) from 142-μm-diameter SiC fibers with a double carbon-coated layer that are known as SCS–6 fibers.[12] Bhatt (1987) has described the method of preparing fiber-reinforced ceramic materials in detail. Fabrication procedures were summarized in chapter 2.

The radiographic evaluation of machined panels guided the cutting of tensile specimens. The selection of cuts was predicated on different density features exhibited by the composite panels to obtain specimens with a sizable volumetric high-density impurity located in the gauge length region, specimens with many small high-density impurities in the gauge length region, and specimens with low-density variations. The specimens were 125 by 12.7 mm by 1 to 2 mm. Two axial wire-wound strain gauges were adhesively bonded to the front and back faces of each tensile specimen. The specimens had glass-fiber-reinforced epoxy tabs for gripping.

---

[12]Textron Specialty Materials Division, Lowell, MA.

Strain
conditioner

X-ray
source

Film
cassette

Load
frame

C-90-12402
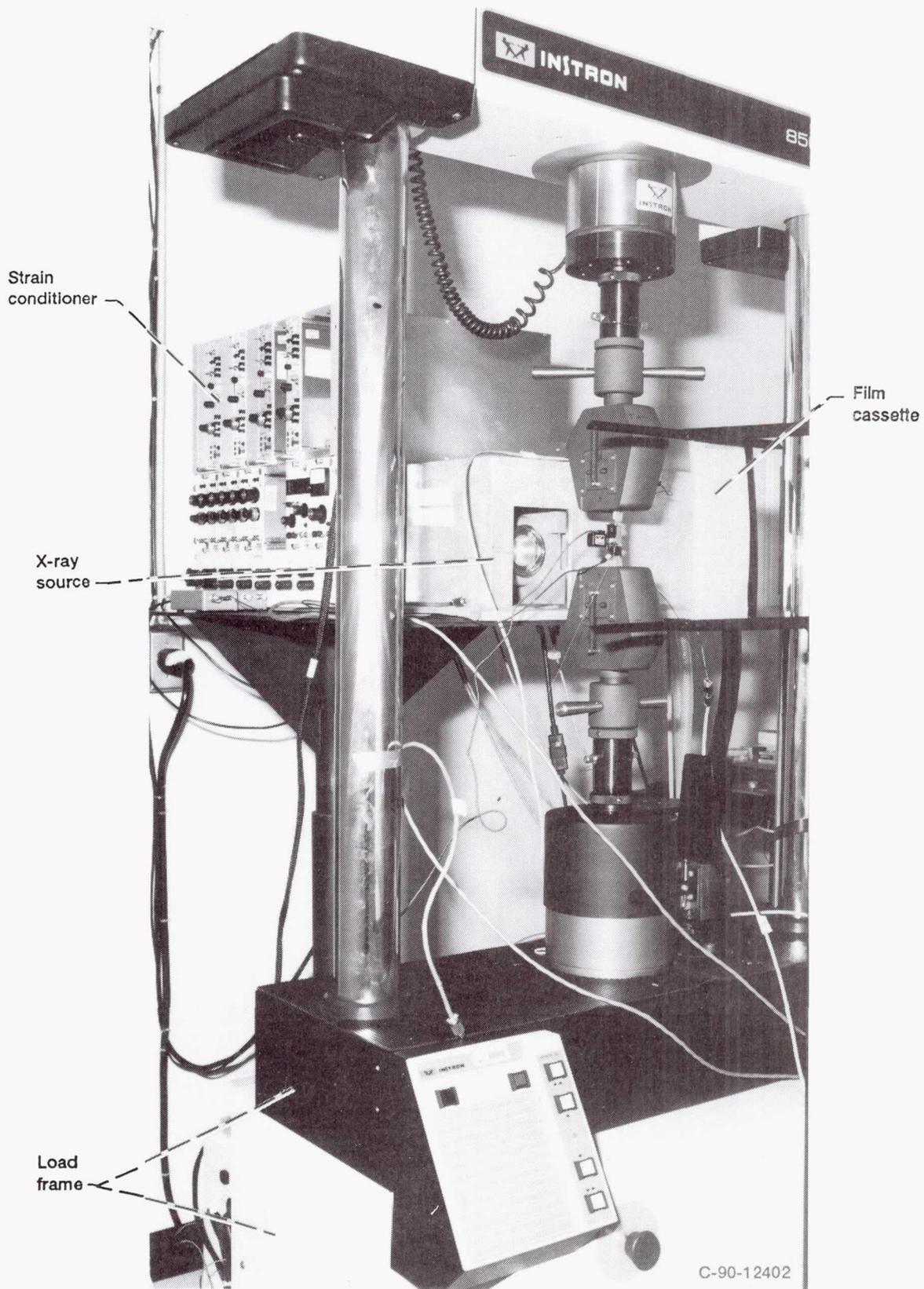
Figure 6.2.—In situ x-ray and materials testing system.
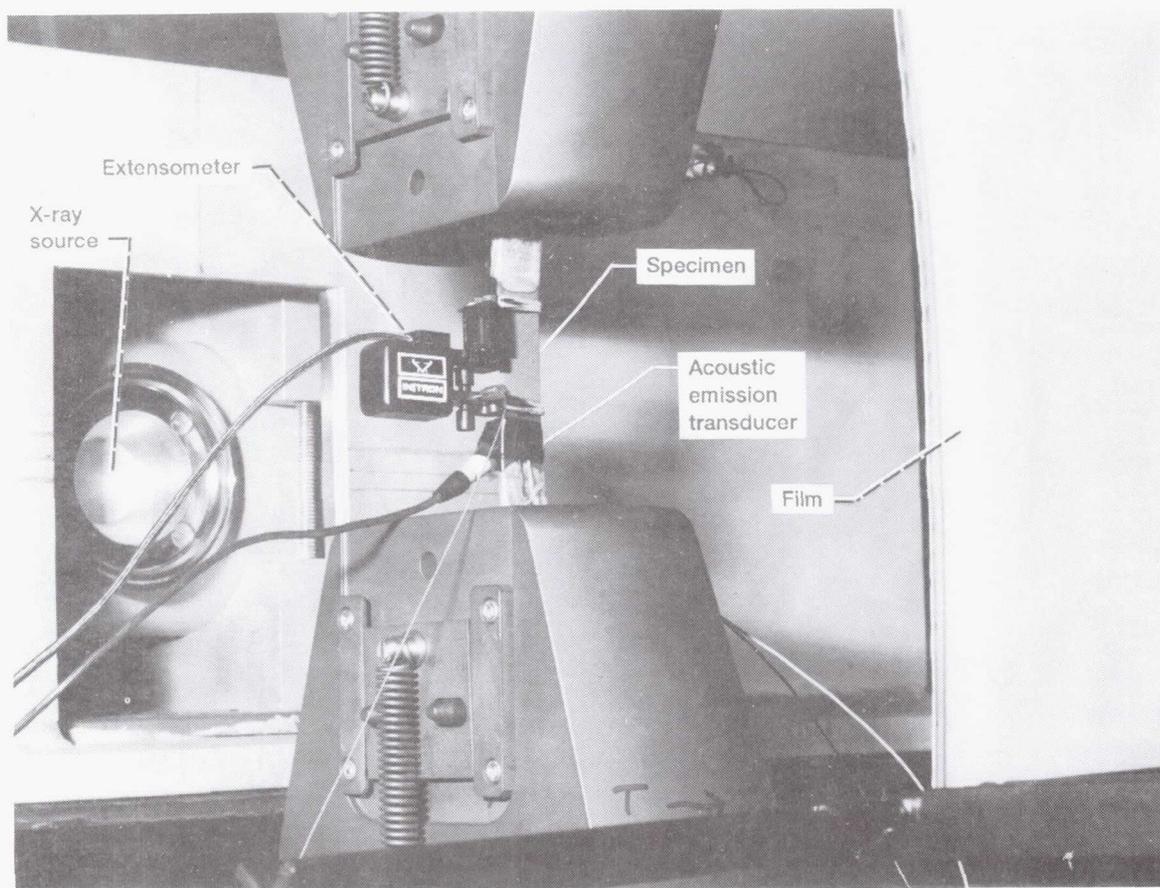
Figure 6.3.—Details of in situ x-ray materials testing system.

6.3 Results

6.3.1 Radiographic Characterization Prior to Testing

Figure 6.4 shows a radiographic image of a representative $[0]_3$ SiC/RBSN panel before and after machining the graphite layer. The graphite layer formed during the high-temperature, vacuum-hot-pressing composite fabrication. It is obvious from the radiographic print before machining (fig. 6.4(a)) that the graphite layer masked any density variation information from the SiC/RBSN panel (i.e., the density variation detected was mainly due to the variation in the thickness and density of the graphite layer itself). Machining the graphite layer enabled better radiographic characterization of the composite panels. The fiber architecture was detected after machining. The orientation of the fibers is evident in figure 6.4(b). High-density impurities (i.e., the dark isolated features (black dots) shown in fig. 6.4(b)) were identified as iron-rich inclusions. Light to white spots in figure 6.4(b) were due to localized low density or surface chipping.

6.3.2 Mechanical Properties

The room-temperature tensile stress-strain behavior for $[0]_1$, $[0]_3$, $[0]_5$, and $[0]_8$ SiC/RBSN specimens is shown in figure 6.5. Corresponding tensile properties are listed in table 6.1. The rule-of-mixtures composite modulus (Agarwal and Broutman, 1979) $E_{(rom)c}$ is

$$E_{(rom)c} = E_m V_m + E_f V_f \qquad (6.1)$$

where E_m and E_f are the matrix and fiber moduli, respectively, and V_m and V_f are the matrix and fiber volume fractions, respectively. Values for $E_{(rom)c}$ appear in table 6.1. The E_m and E_f values used were 110 and 390 GPa, respectively (Bhatt and Phillips, 1988a).

The stress-strain results for the $[0]_1$ and the $[0]_3$ specimens show a linear behavior until final fracture. At ultimate stress the specimens tested in the load control mode failed catastrophically. Specimens tested in the displacement control mode exhibited a load-drop region before final failure. In the

(a) Before.

(b) After.

1 cm
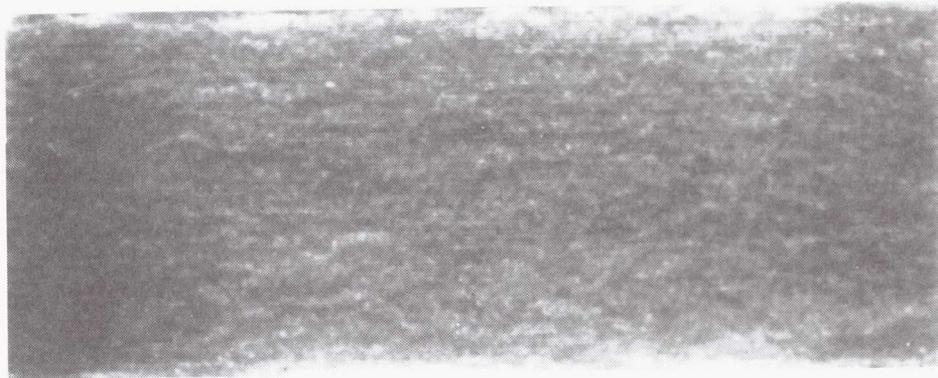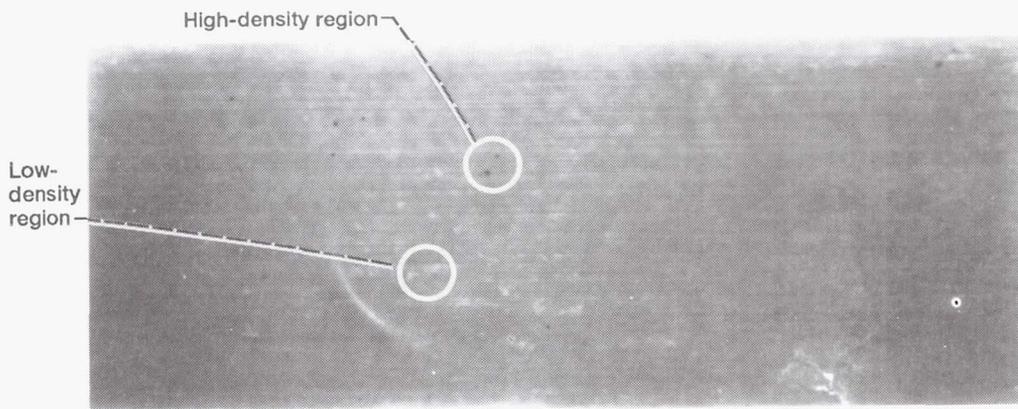
Figure 6.4.—Conventional radiographs of [0]₃ panel before and after machining.
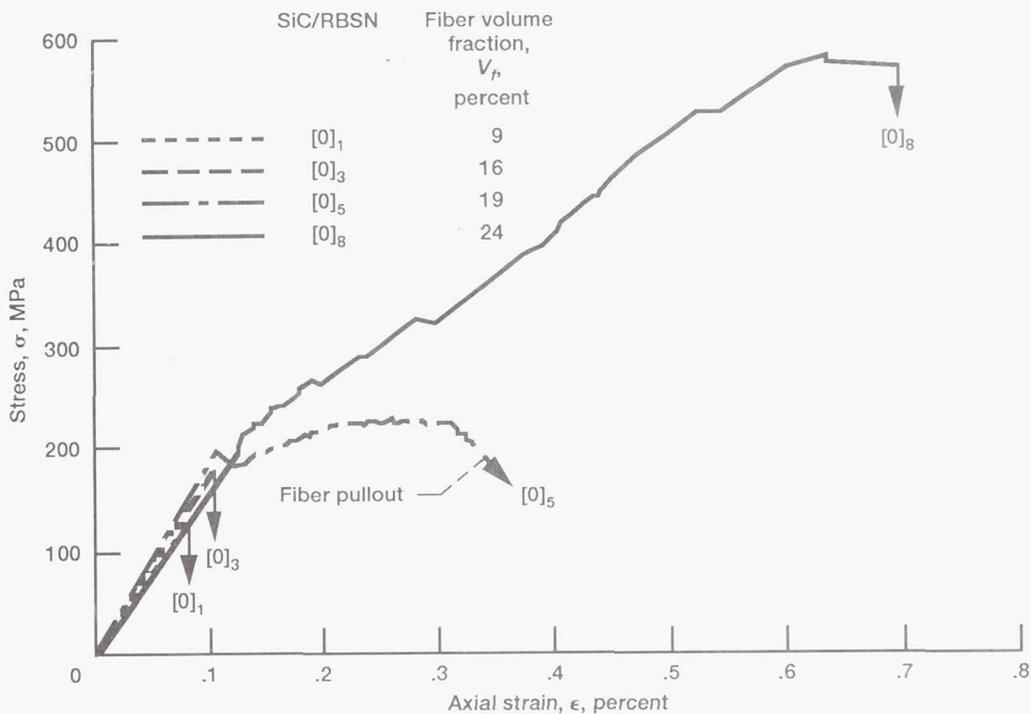
Figure 6.5.—Room-temperature stress-strain behavior for unidirectionally reinforced SiC/RBSN composite specimens.

TABLE 6.1 – ROOM-TEMPERATURE TENSILE PROPERTY DATA FOR SiC/RBSN
COMPOSITE SPECIMENS

SiC/RBSN	Fiber volume fraction, V_f, percent	Number of specimens	Composite modulus, E_{pc}, GPa (experimental)	Composite modulus,[a] $E_{(rom)c}$, (rule of mixtures)	Ultimate stress, MPa	Proportional limit	
						Stress, σ, MPa	Strain, ε, percent
$[0]_1$	19	5	160	135	129	129	1.08
$[0]_3$	16	1	178	155	178	178	.10
$[0]_5$	19	3	180	163	226	197	.11
$[0]_8$	24	1	175	177	576	195	.12
[b]$[0]_8$	23	1	108	175	129	43	.04

[a]$E_c = E_m V_m + E_f V_f$, where E_m = 110 GPa and E_f = 390 GPa.
[b]Overprocessed (1350 °C in N_2 + 4 percent H_2 for 80 hr).

latter case, radiography showed that fiber pullout was the dominant failure mechanism.

The stress-strain results for the $[0]_5$ specimens in figure 6.5 show three distinct regions. In the initial region the stress varied linearly with the strain up to an average stress level of 197 MPa when the load momentarily dropped. In the second region the stress-strain curve became nonlinear and displayed serrations because of the load dropped and recovered without exceeding an average engineering stress of 226 MPa. The third region showed fiber pullouts during which the load dropped slightly but not as catastrophically as upon final failure.

The stress-strain results for the $[0]_8$ specimen (fig. 6.5) show three distinct regions. In the initial region the stress varied linearly with the strain up to a stress level of approximately 195 MPa, when matrix cracking became evident. In the second region the behavior was nonlinear; the load either held or dropped and then recovered and increased as the strain was increased. In the third region the stress varied linearly with the strain in segments where the modulus was either the same or decreasing until maximum tensile stress was reached; shortly afterward the specimen showed minor load-carrying capacity before final fracture.

6.3.3 In Situ Radiographic Imaging

Figure 6.6 shows microfocus radiographs of the $[0]_1$ specimen. These radiographs were made before loading and after failure. The before-loading image (fig. 6.6(a)) shows a 0.5- by 1.0-mm high-density subsurface impurity. This high-density region consisted of cluster of 50-μm-diameter inclusions. One after-failure image (fig. 6.6(b)) shows that the fracture began at the site of the impurity and propagated across the width of the sample. This was inferred from the location and number of the fiber pullouts. Closer examination of the radiographic film showed the presence of multiple breaks per fiber. Figure 6.6(c) shows that microfocus radiography detected a 40-μm fiber pullout length.

Figures 6.7(a) and (b) show microfocus radiographs of two different $[0]_1$ specimens after failure. These radiographs show random fiber pullouts and multiple matrix cracks. These cracks did not propagate through the thickness of the specimens because fiber-matrix debonding occurred at the fiber-matrix interface. Similarly, figure 6.7(c) for a $[0]_3$ specimen shows through-the-width but not through-the-thickness cracks, fiber pullout, and fiber-matrix debonding. The white region toward the right of figure 6.7(c) indicates extensive fiber-matrix debonding, which also occurred outside the 2.54-cm gauge length (the area between the two strain gauges).

Figure 6.8 shows magnified microfocus radiographs of the major cracking zone in the one-ply specimen after failure. Figure 6.9 shows the right and left edges of the same specimen where fiber-matrix debonding is evident. In addition, the optical micrograph in figure 6.10 clearly shows the pullout identified by radiography. Similarly, figure 6.11 shows magnified radiographs of a five-ply specimen with random fiber pullout in and near the major cracking region. Figures 6.12 and 6.13 are optical micrographs of the same specimen showing evidence of fiber-matrix debonding and random matrix cracking where most cracks were not through the thickness or across the width. In addition, by comparing figure 6.11 with figure 6.13 it is evident that the locations of the fiber pullouts were optically nontransparent.

Figure 6.14 shows three radiographs, R6, R8, and R10, selected from a series of 10 in situ radiographs taken throughout the tensile loading history of a $[0]_5$ specimen. The stress-strain behavior is also shown. Radiographs R3, R4, and R5 did not show the presence of matrix cracking. However, in figure 6.14 radiograph R6 shows one major through-the-width crack and R8 shows multiple cracks. Radiograph R10, taken after failure, shows fiber pullouts, closure of cracks imaged earlier under load, and major cracks with a corresponding fiber-matrix debonding region at failure. Radiographs R7 and R9 showed similar information.

Figure 6.15 shows selected in situ radiographs made during the tensile loading history of a $[0]_8$ specimen. Radiograph R0 shows the specimen at near-zero load; R8 shows the specimen at 268-MPa stress and 0.2-percent strain. Radiograph R8 shows six cracks, perpendicular to the fiber orien-

(a) Before loading.

(b) After failure.
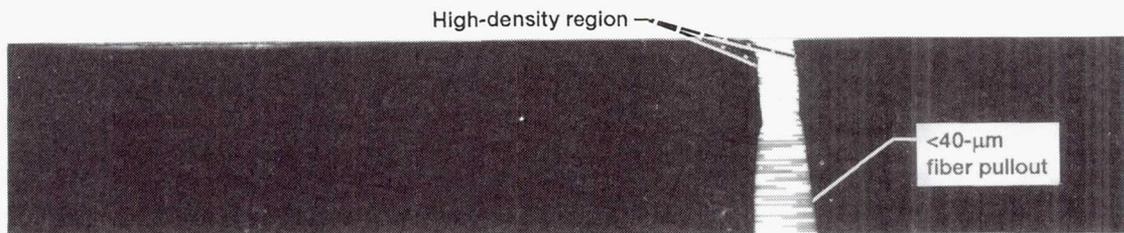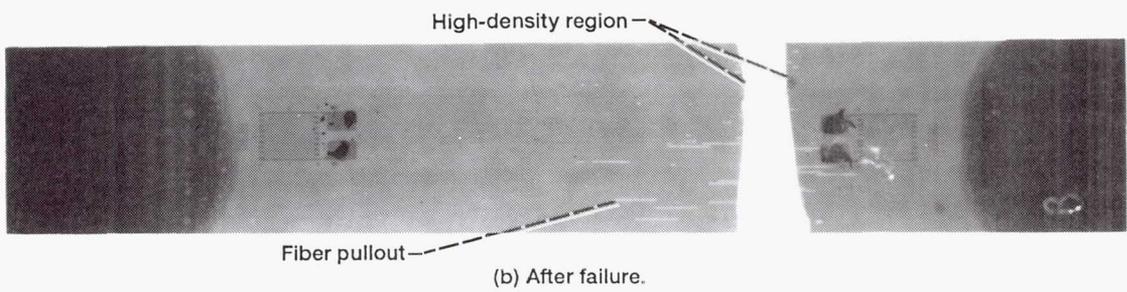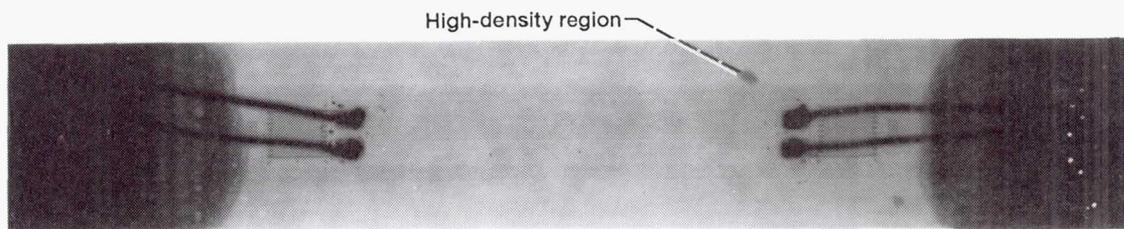
(c) After failure.

Figure 6.6.—Microfocus radiographs of $[0]_1$ SiC/RBSN specimen.

(a) $[0]_1$.

(b) $[0]_1$.

Fiber pullout

(c) $[0]_3$.

Fiber-matrix debond
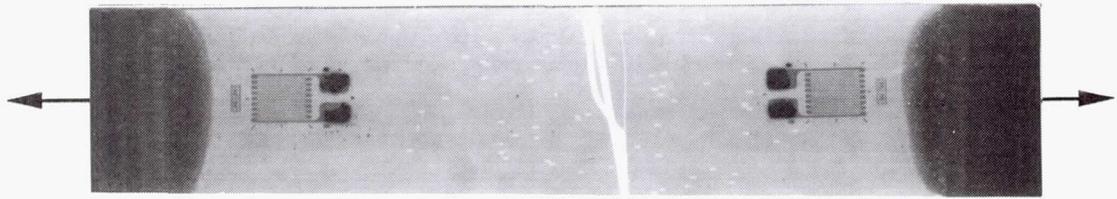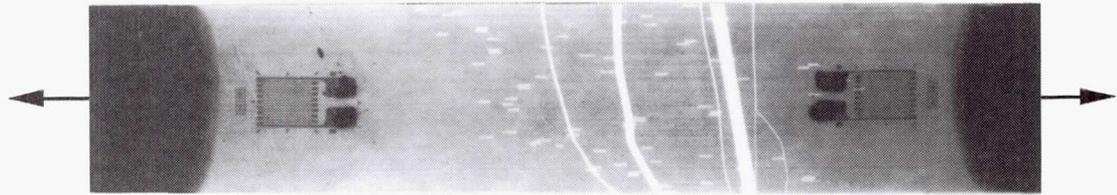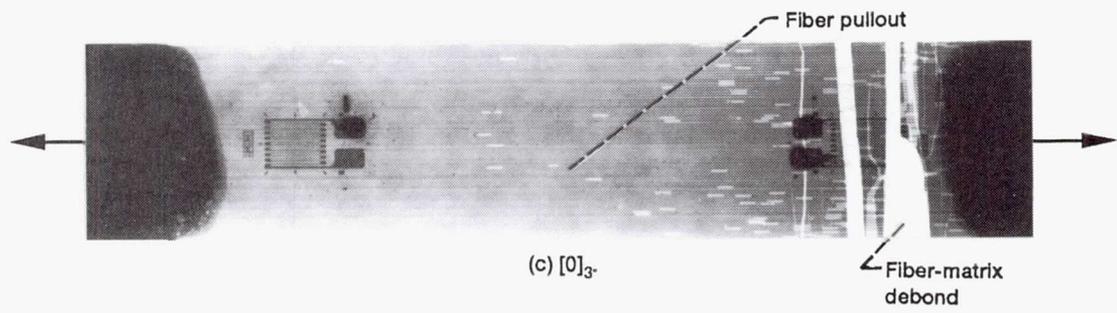
Figure 6.7.—Microfocus radiographs of SiC/RBSN specimens after failure.
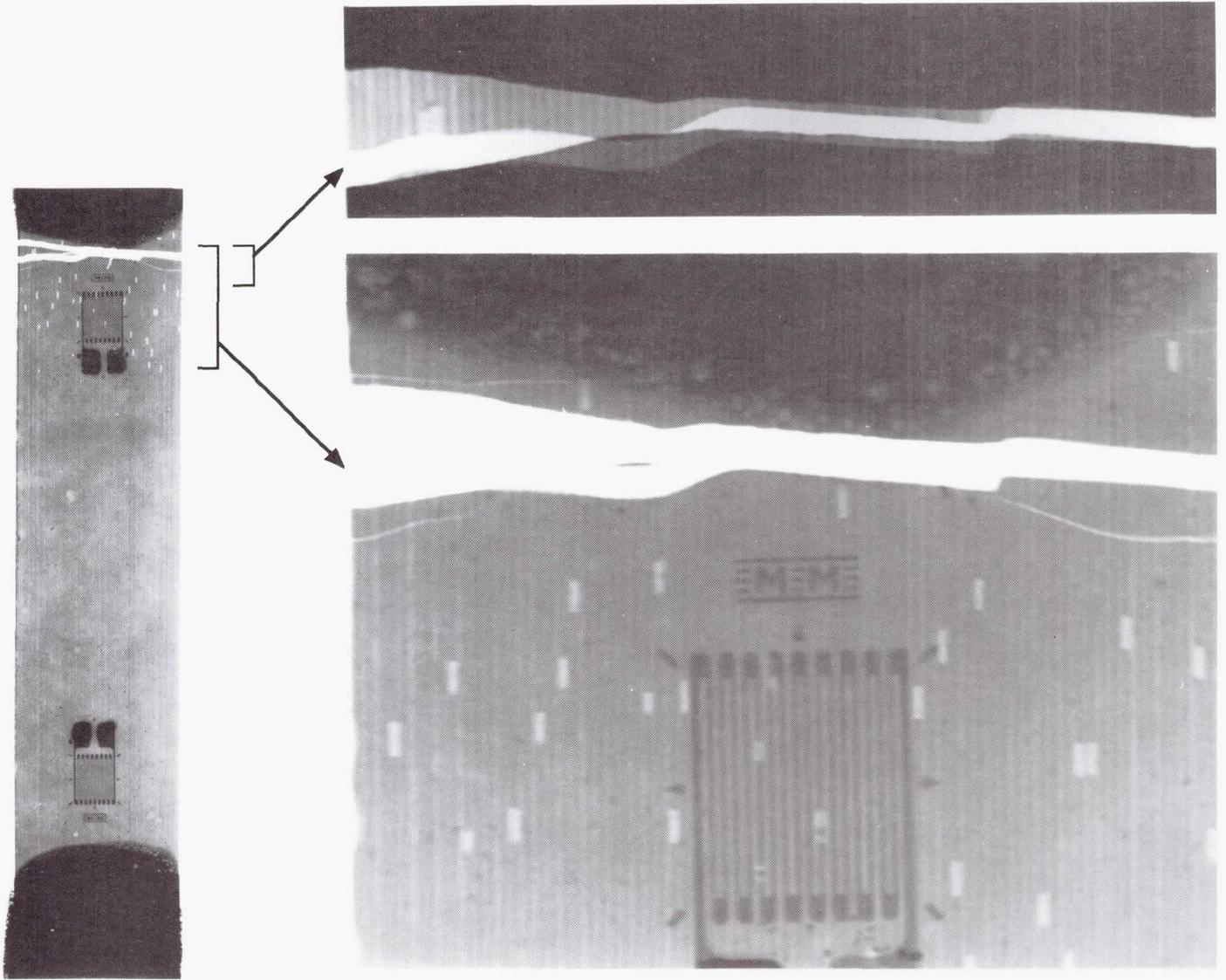
Figure 6.8.—Microfocus radiographs of $[0]_1$ SiC/RBSN specimen after failure.
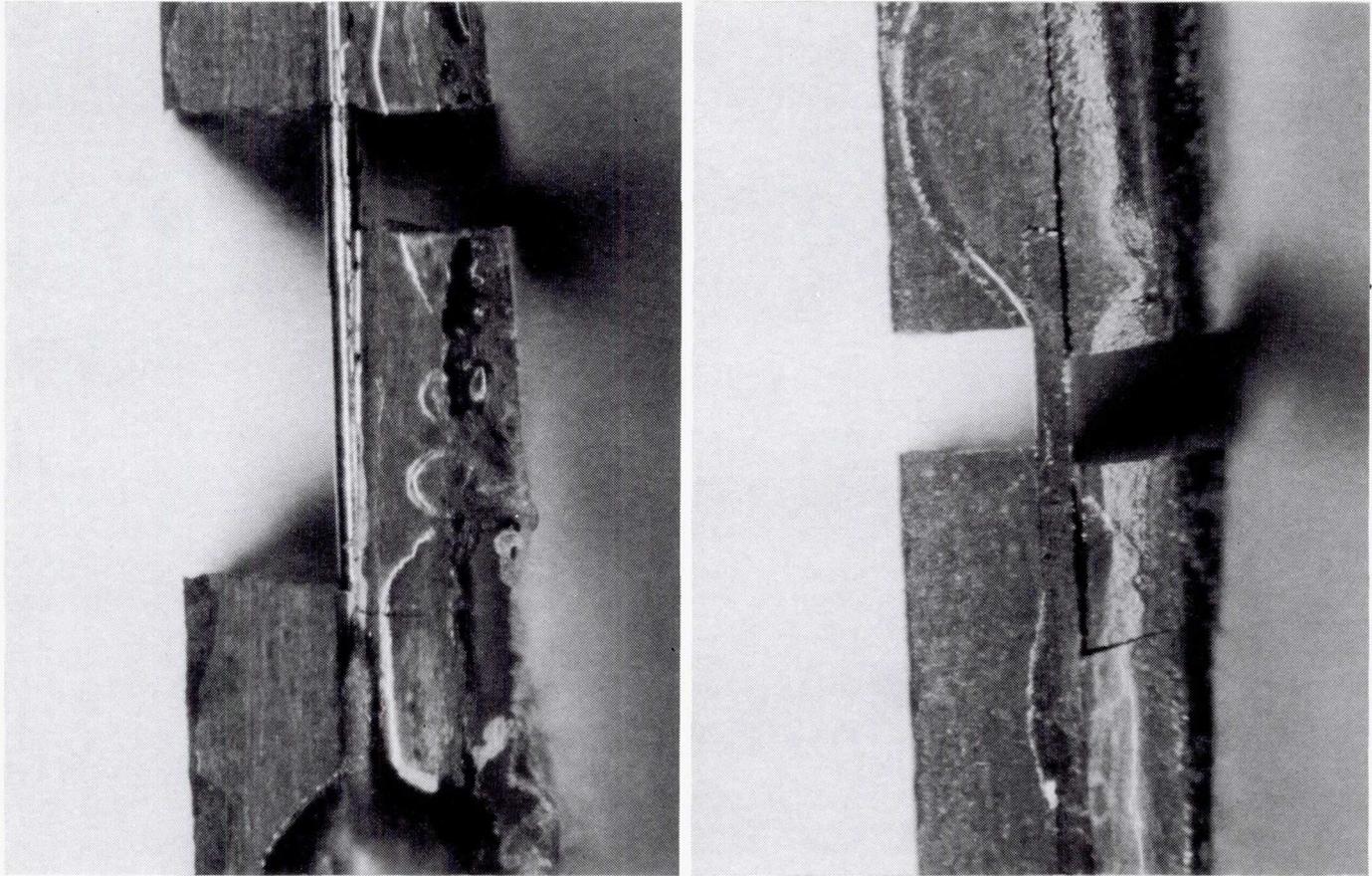
Figure 6.9.—Optical micrographs showing left and right edges of [0]₁ SiC/RBSN specimen (same as in figure 6.8) after failure.
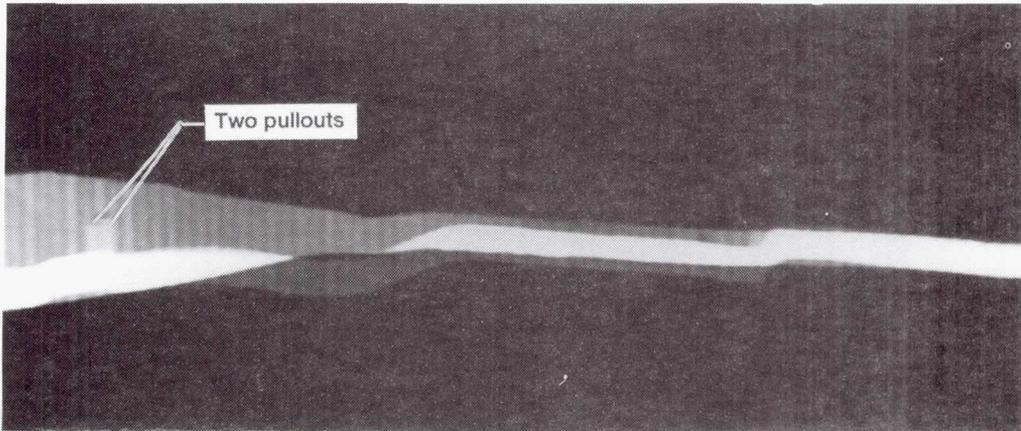
(a) Radiograph.
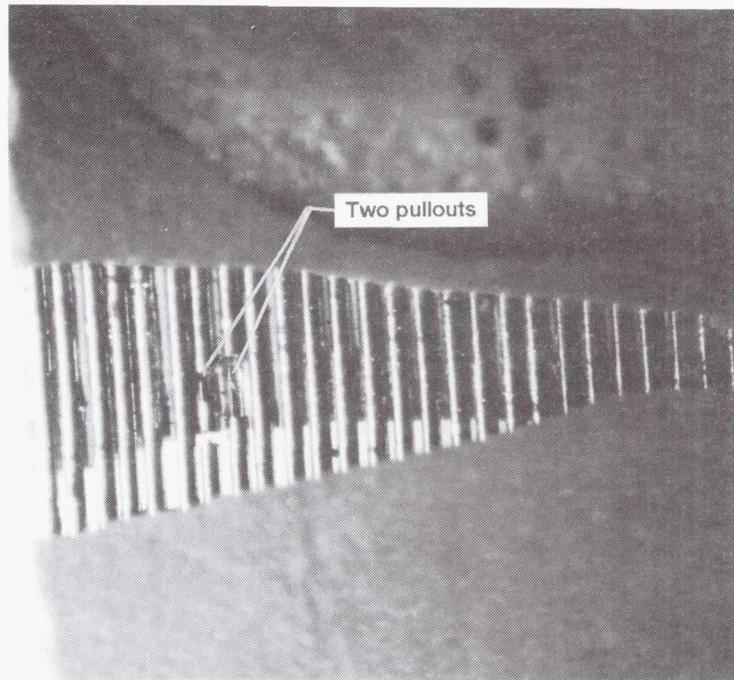
(b) Optical.

Figure 6.10.—Optical proof of fiber pullout detection by radiography in specimen shown in figures 6.8 and 6.9.
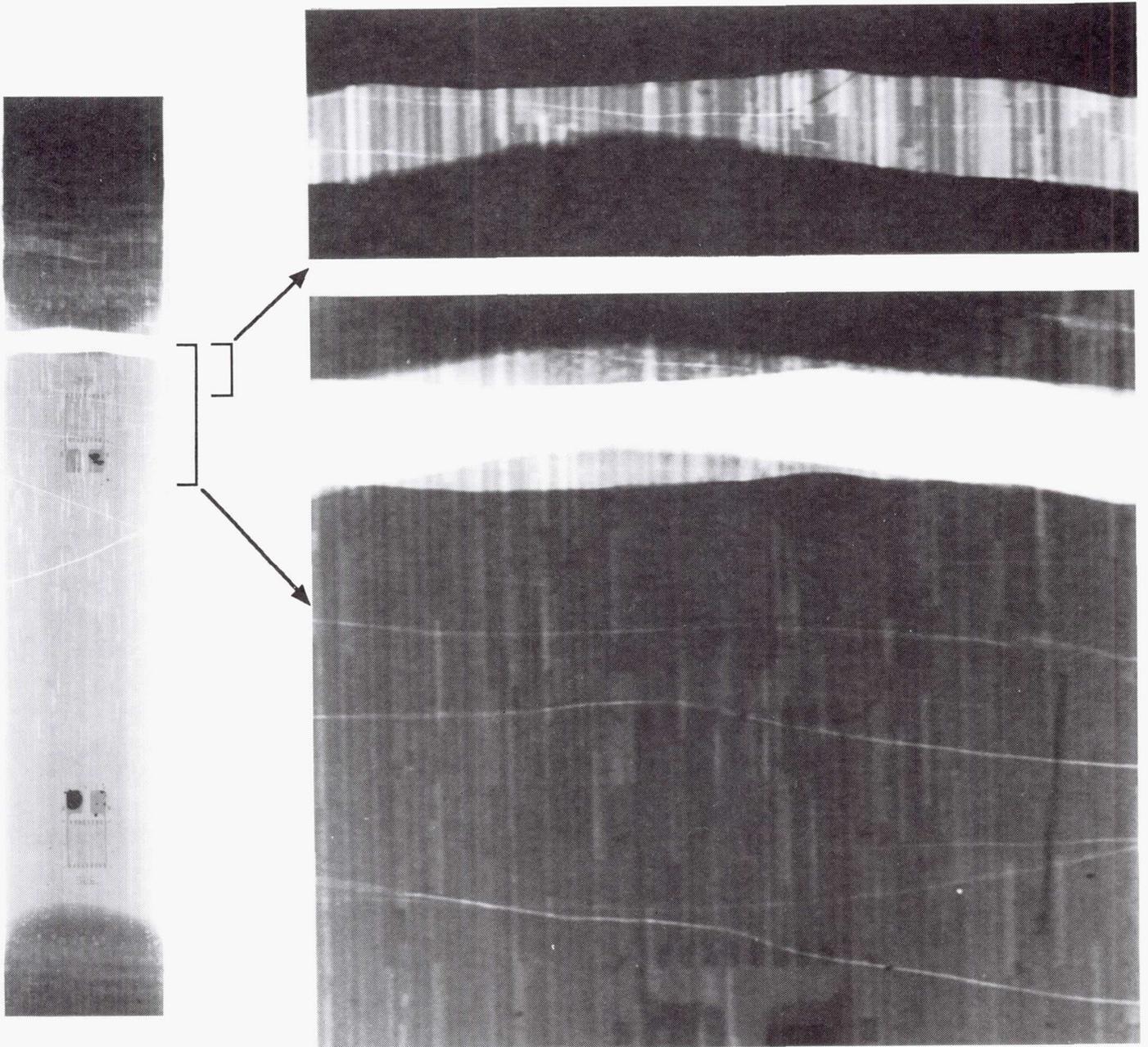
Figure 6.11.—Microfocus radiographs of [0]$_5$ SiC/RBSN specimen after failure.
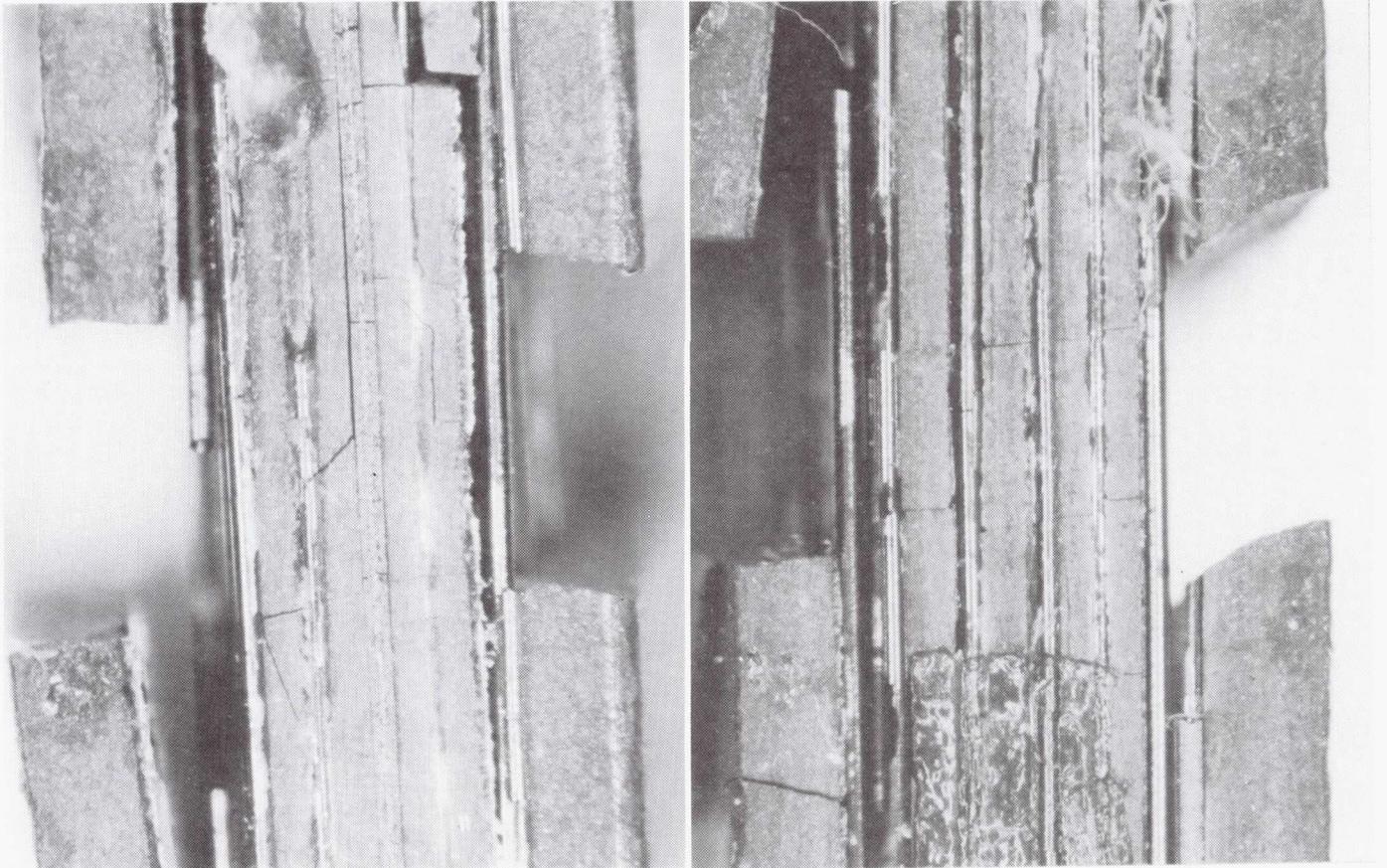
Figure 6.12.—Optical micrographs showing left and right edges of [0]$_5$ SiC/RBSN specimen (same as in figure 6.11) after failure.
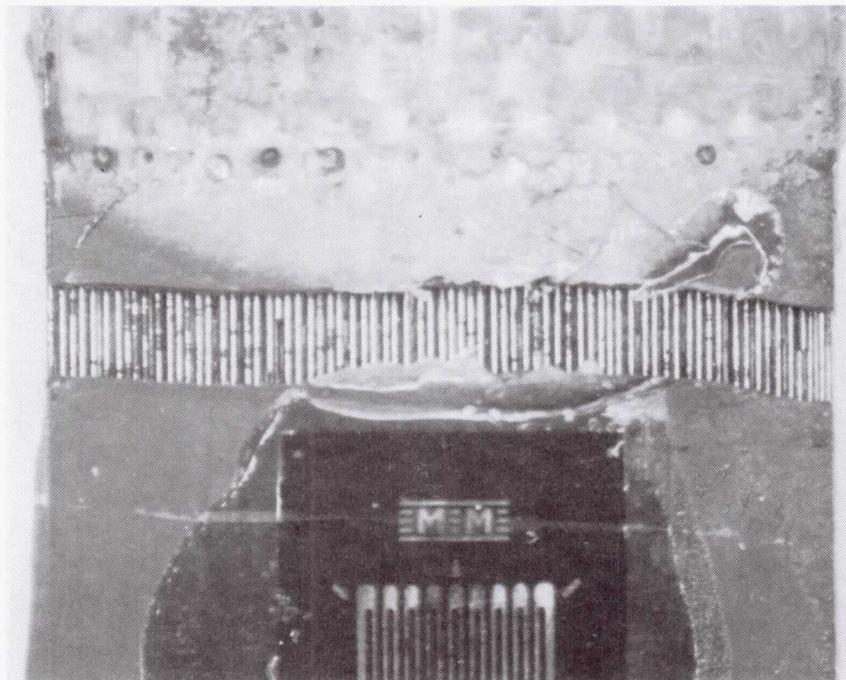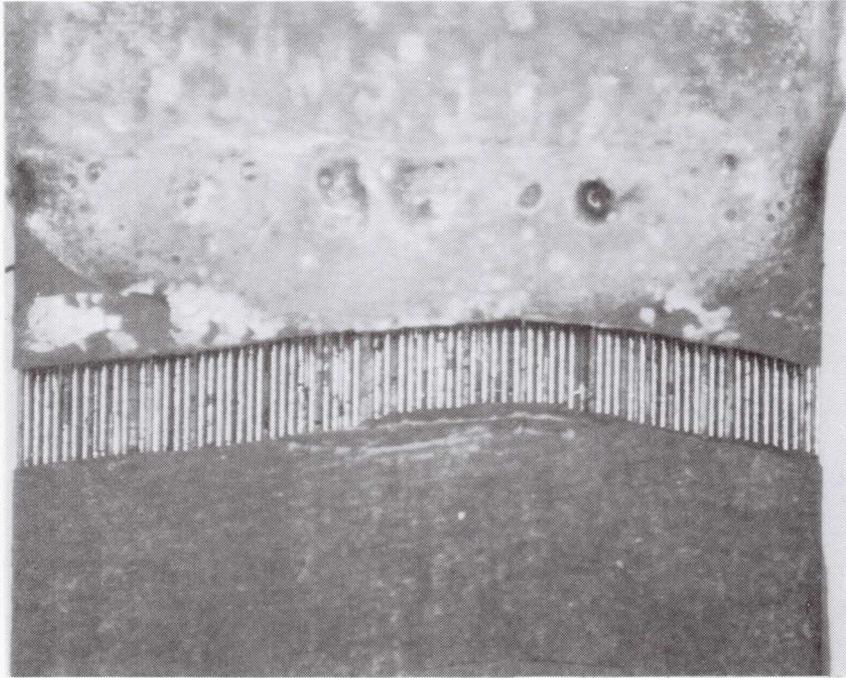
Figure 6.13.—Optical micrographs of front and back faces of $[0]_5$ SiC/RBSN specimen (same specimen as in figures 6.11 and 6.12).
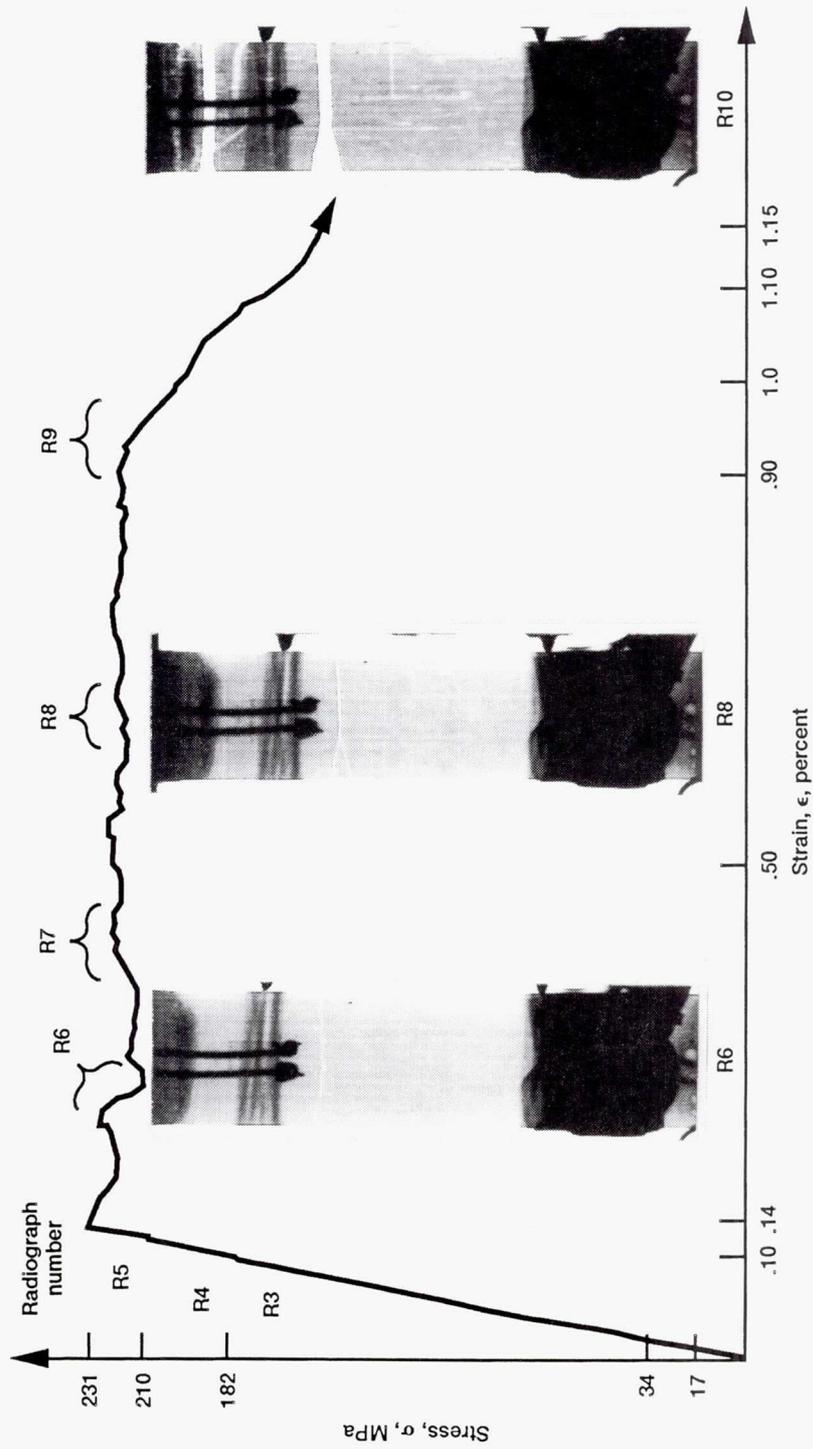
Figure 6.14.—Selected in situ radiographs obtained during tensile loading of $[0]_5$ SiC/RBSN composite ($V_f \simeq 19$ percent).

75
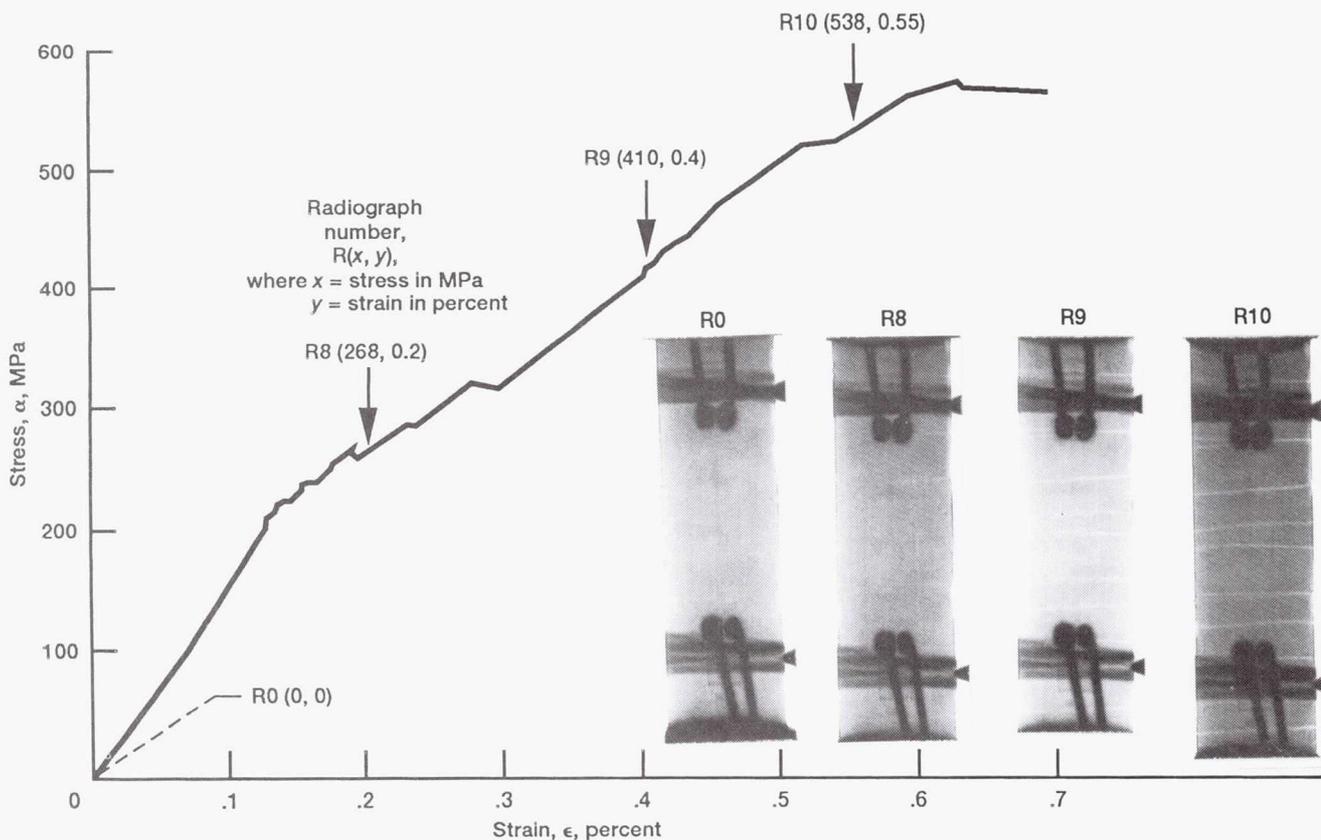
Figure 6.15.—Selected in situ radiographs obtained during tensile loading of [0]₈ SiC/RBSN composite ($V_f \approx$ 24 percent).

tation, that had propagated from right to left and completely through the width of the specimen. Figure 6.16 and table 6.2 summarize the crack development and the corresponding crack spacing imaged in R8. Radiographs R9 and R10 in figure 6.15 show 10 through-the-thickness and through-the-width matrix cracks at 410 and 538 MPa, respectively.

Figure 6.17 is a schematic of the matrix crack spacing method for estimating the interfacial shear strength τ_f based on the Aveston, Cooper, and Kelly (ACK) theory (Aveston et al., 1971).

$$\tau_f = \frac{\sigma_c^m D_f}{2.98 \overline{X} V_f (1 + E_f V_f / E_m V_m)} \qquad (6.2)$$

where σ_c^m is the composite stress corresponding to the first matrix crack, $\overline{X}$ is the mean crack spacing, D_f is the fiber diameter, and the rest of the terms are as defined in equation (6.1). The stress σ_c^m was determined from the stress-strain curve data collected from the clip-on gauge extensometer. It was determined by locating the first deviation from the first linear

region of the curve. It was confirmed by the stress-strain data collected from adhesively bonded strain gauges. The mean crack spacing $\overline{X}$ was measured from the radiographs taken between 71 and 93 percent of ultimate engineering strength. For the [0]₈ composite with a 24-percent fiber volume fraction, a 3.56-mm mean crack spacing, a 195-MPa composite stress at first matrix crack, a 390-GPa fiber modulus, and a 110-GPa matrix modulus, the interfacial shear strength was calculated from equation (6.2) to be 5 MPa. This value for interfacial shear strength agrees with previously obtained data from pushout tests (Eldridge et al., 1991) and from the crack spacing method (Bhatt, 1990).

Figures 6.18 to 6.20 display different failure mechanisms between an optimized (fig. 6.18) and an overprocessed (fig. 6.19) composite. In the optimized case, fibers bridged the cracks and prevented a catastrophic failure. In the overprocessed case, random fiber pullout is evident throughout the gauge length. Some fibers were broken even before testing by overprocessing (high tensile residual stress in fibers) as depicted in figure 6.19. Apparently, overprocessing degraded the fiber coating (fig. 6.20) and weakened or disrupted the interface.
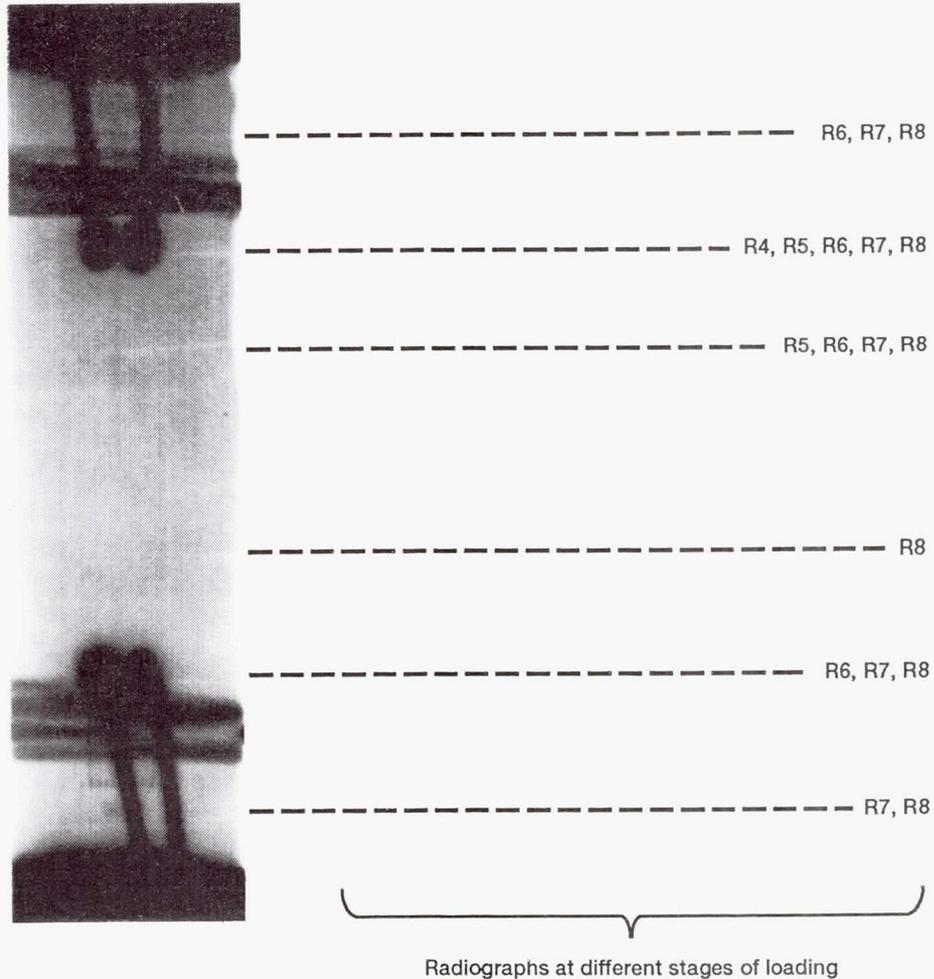
Figure 6.16.—Summary of resulting crack density as presented on radiograph number R8 (fig. 6.15) at 268 MPa and 0.2-percent strain.

TABLE 6.2. – VARIATION OF CRACK DENSITY WITH LOAD FOR
SiC/RBSN $[0]_8$ COMPOSITE ($V_f \approx 24$ PERCENT)

Radiograph number	Stress, MPa	Strain, percent	Percent of ultimate stress (576 MPa)	Number of cracks detected by x rays	Mean crack spacing, $\bar{X}$, mm
R4	219	0.14	38	[a]1	-----
R5	226	.15	39	[a]2	-----
R6	----	----	---	[a]3	8.56
R7	258	.18	45	[a]5	8.02
R8	268	.20	47	[a]6	6.42
R9	410	.40	71	[b]10	3.56
R10	538	.55	93	[b]10	3.56
R12	(c)	(c)	(c)	[b]11	3.47

[a]Not across-width cracks.

[b]Across-width and through-thickness cracks.

[c]After failure.
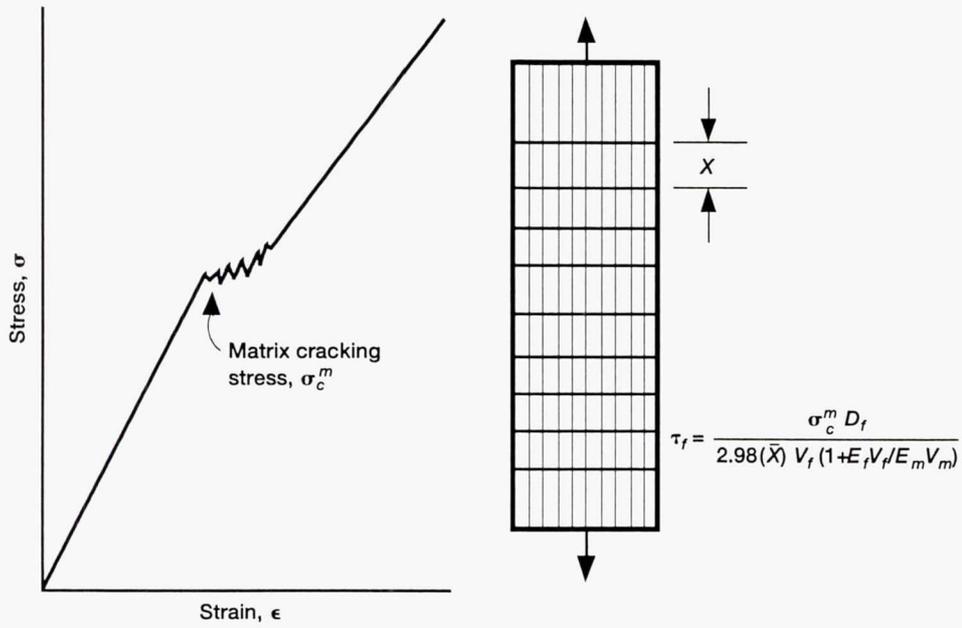
Figure 6.17.—Schematic of matrix crack spacing (Aveston, Cooper, and Kelly) method.

$$\tau_f = \frac{\sigma_c^m \, D_f}{2.98(\bar{X}) \, V_f \, (1 + E_f V_f / E_m V_m)}$$
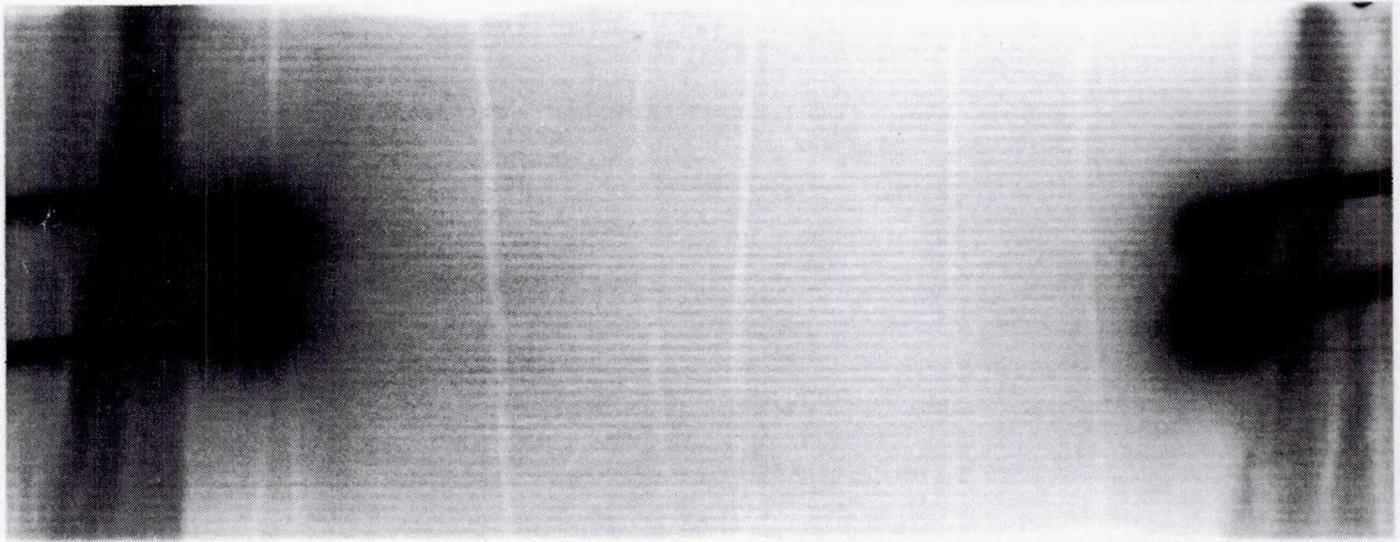
Figure 6.18.—Magnified R9 showing crack bridging in optimized SiC/RBSN composites.

1 mm
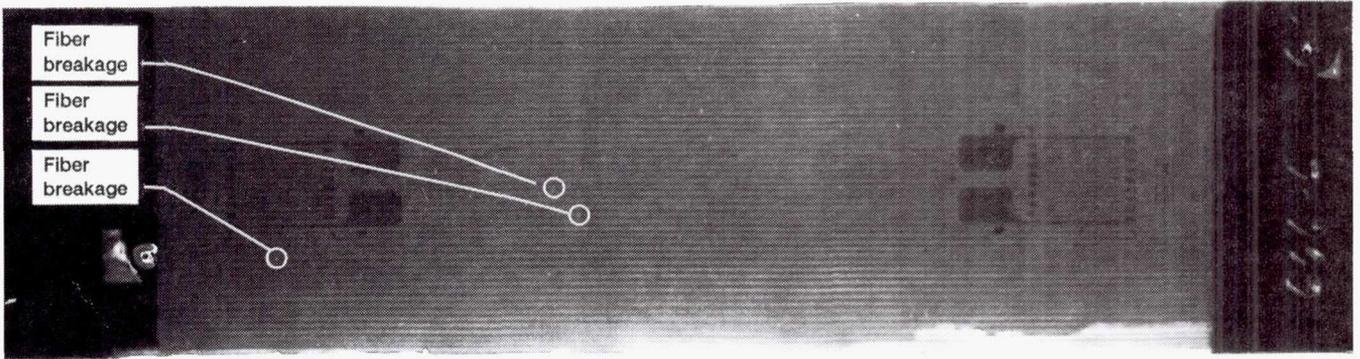
(a) Before testing.

2 mm
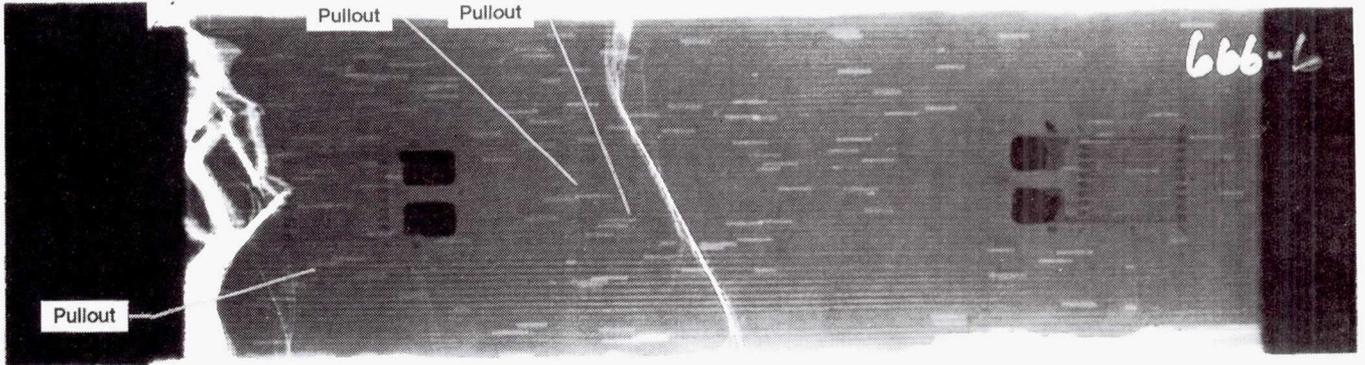
(b) After failure.

2 mm

Figure 6.19.—Overprocessed eight-ply SiC/RBSN composite.

100 μm

(a) 1200 °C in N_2 for 40 hr.
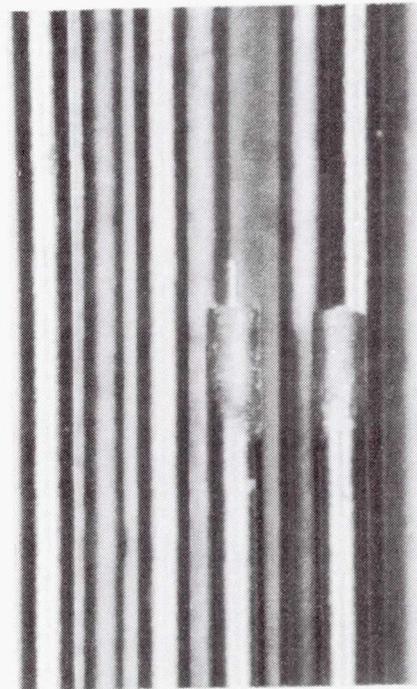
(b) 1350 °C in N_2 + 4% H_2 for 80 hr.

Figure 6.20.—Fractured SCS–6 fibers in eight-ply SiC/RBSN composites.

6.4 Discussion

6.4.1 Significance of Radiographic Characterization

Radiography of silicon powder cloths and SiC/RBSN panels helped to identify the presence and type of impurities and the local density variations within each panel and between panels. This information presented options for designing the tensile specimens. Specimens that contained large volumetric flaws could be monitored and compared with specimens that were free of these flaws. Specimens that contained excessive local density variations could be compared with specimens that had minor local density variations. Consequently, on the basis of whether or not impurities and local density variations are affecting the fracture behavior of the composite, materials engineers can modify powder processing or composite fabrication in order to free the composite from detrimental defects.

This study found that a 0.5- by 1.0-mm high-density region affected the fracture behavior of the $[0]_1$ composite (fig. 6.6) because it behaved like a monolithic ceramic (fig. 6.5). Conversely, isolated and randomly distributed high-density inclusions smaller than 150 μm in diameter did not directly affect the fracture behavior of the $[0]_1$ and $[0]_3$ specimens. Similarly, high-density inclusions up to 225 μm in diameter did not appear to affect the fracture behavior of the $[0]_5$ composites. Local density variations within the tensile specimens also did not seem to affect fracture behavior. These preliminary conclusions were based on the limited number of samples available for this study.

Microfocus radiography of failed specimens proved useful in detecting fiber pullout, cracks, and crack branching. This study demonstrated the need for and advantages of microfocus over conventional radiography in studying and explaining the fracture behavior of composites.

6.4.2 Mechanical Properties

The primary modulus before first matrix cracking of the composite E_{pc} was about the same (within 12 percent) for all the $[0]_1$, $[0]_3$, $[0]_5$, and $[0]_8$ composite specimens. These primary moduli corresponded to within 1 to 12 percent of the rule-of-mixtures composite modulus $E_{(rom)c}$ defined in equation (6.1). Overestimates on the order of 12 percent can be explained by the fact that the one-ply and three-ply materials were thinner and hence denser than the normal RBSN matrix with a modulus of about 110 MPa. Close agreement between E_{pc} and $E_{(rom)c}$ is indicative of an adequate load transfer between fibers and matrix (Bhatt, 1990).

The first matrix cracking strains and stresses of the $[0]_1$ and $[0]_3$ specimens were also the strains to failure and the ultimate strengths of these specimens, respectively. In contrast, first matrix stress and strain for $[0]_5$ (19-percent volume fraction) were close to those of $[0]_8$ (24-percent volume frac-

tion), where the strain to failure showed great enhancement over the one-ply, three-ply, and the five-ply composite specimens.

The ultimate tensile strength increased with the fiber volume fraction for all composite specimens because it is primarily controlled by the bundle strength of the fibers (Bhatt, 1990).

6.4.3 Significance of In Situ Radiography

For $[0]_1$ and $[0]_3$ composites, in situ radiography imaged cracks and fiber pullouts after ultimate failure. This was only achieved by testing samples in the displacement control mode. Under the load control mode sudden catastrophic failure occurred at ultimate strength and precluded making the x-ray exposure. In situ radiography during failure and in situ and microfocus radiography after failure helped to identify the presence and location of matrix cracks on the ply level, fiber pullout, and fiber-matrix debonding. Fiber pullouts and matrix cracks, which were opaque for optical evaluation, required imaging by radiography.

Failure sequences for $[0]_5$ composites were radiographically imaged in the nonlinear region and within and after the fiber pullout region (fig. 6.14). Fiber breakages could not be imaged until fibers started pulling apart. Preexisting microcracks could not be imaged because of the resolution limitations of the x-ray system. The first matrix crack was imaged after the stress-strain curve indicated that matrix cracking had occurred. Thereafter, multiple cracks were imaged as the specimen was strained and fibers started to pull out. Matrix cracks would tend to close until the final failure of the composite. At this point fiber pullout, fiber-matrix debonding, and fiber breakage were readily imaged. Optical examination after failure demonstrated that matrix cracks had propagated within lamina across the width of the sample but not through the thickness.

For $[0]_8$ composites, in situ radiography was able to image matrix crack development throughout the tensile loading history as shown in figures 6.15 and 6.16 and as summarized in table 6.2. In situ radiography enabled the use of the mean crack spacing method to determine the interfacial shear strength as defined in equation (6.2) and also verified the experimental procedure (Bhatt, 1985) used to determine interfacial shear stress. From table 6.2 and figure 6.15 it is apparent that the number of major matrix cracks and corresponding spacings did not change between 71 and 93 percent of ultimate strength. This verified that unloading the sample at about 75 percent (Bhatt, 1985) of ultimate load to perform the crack spacing measurements was done in the proper loading region. The x-ray monitoring technique is preferable to optical methods (Bhatt, 1985) for the following reasons: First, stopping the test and unloading is not practical. Second, estimating the presence of cracks that have already closed due to unloading leads to an overestimate of interfacial shear stress. Third, the ultimate strength is real and not estimated

from other similar samples. And fourth, if the sample shatters into fragments after failure or fails earlier than expected, the cracks have already been imaged and spacings can be measured from the x-ray film. Furthermore, even in situ optical monitoring will not deliver this information in a reasonable time because the high magnification needed to monitor the cracks reduces the imaging field and the working focal length. In addition, in situ optical monitoring will miss hidden cracks in subplies.

6.5 Conclusions

In situ radiography during room-temperature tensile testing of SCS–6 silicon-carbide-fiber-reinforced, reaction-bonded silicon nitride (SiC/RBSN) composite specimens is a reliable method for monitoring damage accumulation, for determining the interfacial shear strength between the SiC fiber and the RBSN matrix by the matrix crack spacing method, and for identifying different failure mechanisms. Matrix cracking, fiber-matrix debonding, and fiber pullout are imaged throughout the tensile loading of the specimens. Radiographic evaluation before, after, and during loading provides data on the effect of preexisting volume flaws (e.g., high-density inclusions) and on the effect of local density variations on the fracture behavior of composites. In situ radiography can provide a basis for identifying important failure mechanisms, validating analytical models, verifying experimental procedures, and optimizing fabrication processes through timely feedback of useful information.

Page intentionally left blank

Chapter 7

General Discussion, Conclusions, and Future Research

7.1 General Discussion

Point-scan digital radiography (PSDR) provides several unique capabilities: precise measurement of x-ray attenuation, scan imaging with high spatial resolution on the order of 100 μm, x-ray beam profiling, and investigation of the stability of different x-ray sources. The PSDR system is limited by long scan times and photon starvation for thick monolithic specimens and composite constituents of comparable total mass attenuation coefficient. Opportunities exist for improving the system's contrast sensitivity and penetration power by using higher voltage x-ray tubes, microfocus tubes, array detectors (preferably area detectors), and multichannel analyzers and energy filters. The PSDR of this study nevertheless proved instrumental in making precise x-ray attenuation measurements and in characterizing thin monolithic materials.

Physical density was correlated with CT number, giving a calibration curve for monolithic ceramic materials. This curve reduced interpretational ambiguities associated with the indirectness of nondestructive measurements. Multiparametric probing and signal analysis are essential for removing ambiguities in collecting complementary and corroborative data. This conclusion is stressed in chapter 4, where film radiography and acoustic microscopy were used to substantiate XCT findings.

X-ray computed tomography (XCT) density information described in chapter 5 proved helpful in identifying fabrication-related problems and comparing different processing methods (e.g., consolidation of cylindrical rods versus annular rings). XCT helped avoid cutting through fibers during final machining of the rod samples. XCT is now routinely used to guide machining of components to final dimensions.

XCT density information was shown to be an important guide in structural design and modeling of composite components. Distortions in structural constituents, which may cause nonuniform material responses at high temperatures and under different loading conditions, were detected by XCT. Nondestructive evaluations coupled with destructive verifications will certainly improve and accelerate the development of advanced composite components.

Three-dimensional volumetric density variations in composite components were readily imaged by XCT and can guide geometric modeling of composite constituents. Moreover, XCT can help determine composite spatial variations of stiffnesses if CT artifacts are minimized. Engineering tomography, which incorporates XCT density information in finite element modeling, can significantly help in predicting the life and serviceability of composite components.

Predicting the life of components cannot be based on coupon test results because the mechanical behavior of components is mainly affected by fabrication processes that are unique to the component. In addition, the nature of loading, mean residual stresses, the multiaxial state of stress, and size effects are distinctive characteristics of components. Thus, XCT specifically and often nondestructive evaluation (NDE) modalities generally can help to reduce engineering approximation approaches, to improve statistical interpretation (imaging modalities are the source of a large data base) of life and deterministic life prediction analyses, and to ameliorate and accelerate damage tolerance assessment.

Noninvasive in situ monitoring using the in situ x-ray and materials testing system described in chapter 6 demonstrated many benefits in understanding the mechanical behavior of emerging advanced composite material systems. Specifically, for the particular material systems examined in this work, a 0.5- by 1.0-mm high-density region can affect the fracture behavior of the $[0]_1$ ceramic matrix composite. Comparatively isolated and randomly distributed high-density inclusions less than 150 μm in diameter did not adversely affect the fracture behavior of the $[0]_1$ and $[0]_3$ ceramic matrix composite specimens tested. Similarly, high-density inclusions greater than 225 μm in diameter did not affect the fracture behavior of the $[0]_5$ ceramic matrix composite speci-

mens. Finally, local density variations within the composite tensile specimens had little effect on their fracture behavior.

The first matrix cracking strains and stresses of $[0]_1$ and $[0]_3$ specimens were also the strains to failure and ultimate strengths, respectively, of these specimens. In contrast, first matrix stress and strain for $[0]_5$ specimens (19-percent volume fraction) were close to those of $[0]_8$ specimens (24-percent volume fraction), where the strain to failure showed great improvement over the one-ply, three-ply, and five-ply composite specimens. A fiber volume fraction of over 19 percent assured rule-of-mixtures-predicted composite behavior. Ultimate tensile strength increased with the fiber volume fraction for all composite specimens tested because it is primarily controlled by the bundle strength of the fibers.

Microcracks that may have existed in the linear region could not be imaged because of limitations in the resolution and detection capabilities of the x-ray system used. But newly formed matrix cracks were readily imaged after loading beyond the linear region. Multiple cracks were imaged as the specimen was further strained. When fibers started to pull out, the matrix cracks closed until the final failure of the composite. Fiber pullout, fiber-matrix debonding, and fiber breakage were imaged at this stage.

In situ radiography of a $[0]_8$ ceramic matrix composite imaged the matrix crack development throughout the tensile loading history. This enabled the mean crack spacing method to be used to determine the interfacial shear strength and verified the experimental procedure used for determining interfacial shear stress.

X-ray monitoring of the fracture process was preferred over optical methods because optical methods are invasive, using a crack enhancer agent, and because they miss hidden cracks and anomalies located below the surface.

Microfocus radiography of failed specimens proved useful in detecting fiber pullout. Cracks and crack branchings that did not close after failure were imaged, clearly showing the advantage of microfocus over conventional radiography in studying and explaining the behavior of composites under load. Using a microfocus source may enhance the imaging capabilities of the in situ system.

7.2 Conclusions

This report has described the development and application of x-ray attenuation measurement systems capable of (1) characterizing density variations in monolithic ceramics and in ceramic and intermetallic matrix composites and (2) noninvasively monitoring damage accumulation and failure sequences during tensile testing of ceramic matrix composites at room temperature. Volumetric density characterizations were performed on laboratory samples and on subscale engine components. In situ monitoring of damage accumulation was only performed on tensile specimens.

A point-scan digital radiography system and an in situ x-ray material testing system were developed. The former was used to characterize density variations in monolithic ceramics and ceramic composites, and the latter was used to image the failure behavior of silicon-carbide-fiber-reinforced, reaction-bonded silicon nitride matrix composites. In order to extend the work to nondestructive evaluation of components, state-of-the-art x-ray computed tomography was investigated to determine its capabilities and limitations in characterizing the density variations of a silicon carbide rotor, a silicon nitride blade, and a silicon-carbide-fiber-reinforced beta titanium matrix rod, rotor, and ring. Microfocus radiography, conventional radiography, scanning acoustic microscopy, and metallography were used to corroborate x-ray computed tomography findings.

Point-scan digital radiography was found to be a viable technique for characterizing density variations in monolithic ceramic specimens. But it was limited and time consuming in characterizing ceramic matrix composites. Precise x-ray attenuation measurements, reflecting minute density variations, were achieved by photon counting and by using microcollimators at both the source and the detector.

X-ray computed tomography was found to be a viable attenuation technique for measuring cross-sectional volumetric density variations in monolithic ceramics and metal matrix composites. The capabilities and limitations of x-ray computed tomography for characterizing monolithic ceramics were established. X-ray computed tomography was successfully applied to characterizing a variety of subscale components with relatively simple geometric shapes. Tomographic data provide the information needed to deduce material densities on a spatially defined basis. Tomographic findings were corroborated by radiographic, ultrasonic, and optical microscopic data. The capabilities and limitations of x-ray computed tomography for characterizing metal matrix composite subscale engine components were defined. X-ray computed tomography provides spatial density information that can be incorporated in finite element modeling of composite spatial stiffnesses and in geometric modeling of structural constituents. It can accelerate the development of composite components. X-ray computed tomographic imaging identifies problems associated with manufacturing processes, guides machining of components to final dimensions, and can lead structural design engineers to evolve realistic failure and life-prediction models.

In situ radiography during room-temperature tensile testing of SCS–6 silicon-carbide-fiber-reinforced, reaction-bonded silicon nitride (SiC/RBSN) composite specimens was found useful and reliable for monitoring damage accumulation, for determining the interfacial shear strength between the SiC fiber and the RBSN matrix by the matrix crack spacing method, and for identifying principal failure mechanisms. Matrix cracking, fiber-matrix debonding, and fiber pullout were imaged during tensile loading of ceramic matrix

composite specimens. Radiographic evaluation before, after, and during loading provided data on the effect of preexisting flaws (e.g., high-density inclusions) and on the effect of local density variations on the fracture behavior of composites. This approach can provide a basis for identifying different failure mechanisms, validating analytical models, verifying experimental procedures, and optimizing fabrication processes through proper feedback.

Results from such in situ monitoring of coupon testing coupled with materials characterization of related subscale components can immensely improve component structural modeling and life prediction. This modeling and prediction would otherwise be nonattainable because of the enormous cost attached to modeling that is based on direct testing of subscale components.

7.3 Future Research

Potentials were identified for extending the research activities in several areas: point-scan digital radiography (chapter 3) can be improved by using a relatively high-voltage microfocus source and a multichannel analyzer for selective energy analysis, and by enlarging the collimation at the detector. These improvements will enhance precision x-ray attenuation measurements for discerning minute material density or composition variations, for distinguishing thickness variations, and for detecting defects and differentiating between their chemical compositions.

Further work in high-resolution and high-energy x-ray tomography (chapters 4 and 5) is needed to extend the calibration density and CT number data, to allow the characterization of thin and complex-shaped ceramics and thick and relatively dense metal matrix composites, to eliminate the photon starvation problem in complex-shaped ceramic parts, and to reduce the scanning time. Furthermore, research in revolutionizing the XCT scanning geometry by placing the x-ray source inside the ring or rotor and the detector on the outside would call for simultaneous modification of existing reconstruction algorithms. This scanning geometry will permit the use of microfocus tubes at lower voltages than their conventional counterparts because the x-ray path is reduced within the material under evaluation. In addition, engineering tomography will be pursued more aggressively to help in life prediction for real components.

Research should be extended to real-time microfocus radiography and/or near-real-time digital radiography (chapter 6) with an advanced area detector in order to monitor the mechanical behavior of emerging ceramic matrix and metal matrix composites with fibers (10 to 70 µm in diameter) much smaller than the 142-µm-diameter SCS–6 fiber. Also scatter radiation rejection techniques (mechanical and/or electronic) need to be developed to better discriminate between fibers and matrices of similar densities and comparable x-ray mass attenuation coefficients. Furthermore, in situ work similar to that in chapter 6 should be extended to braided and woven composites for better understanding of their damage tolerances and failure mechanisms. In addition, the research in chapter 6 can be extended to study pullout in order to characterize the fiber-matrix interface more closely.

Cone beam tomography and laminography need to be developed concurrently with high-resolution and sizable-area sensors to provide cross-sectional information on the ply level of laminated braided and woven composites.

Standards must be established by comparative characterization of composite samples that are fabricated differently or treated in different environments for varying times, temperatures, and pressures. A set of reference samples would then be available from which degradation assessments can be made during the life of the components.

Page intentionally left blank

Appendix A
Slurry Pressing of Nitrides

Slurry pressing was used because it can produce a more homogeneous and dense microstructure with smaller critical flaws (Freedman and Millard, 1986). Figure A.1 shows the slurry-processing flow chart; table A.1 shows the slurry sieved characteristics. Agglomerates were removed from the ethanol slurry of silicon nitride powder before vacuum drying. After milling for 100 hr, agglomerates and milling debris greater than 10 μm were removed. Ammonium hydroxide

(NH$_4$OH) was added for pH slurry adjustments during another 100-hr grinding. Then the slurry was compacted between filter paper disks sandwiched between porous stainless steel disks. The solid was contained between the filter papers, and the liquid escaped through the porous steel disks. The nitride disks were dried and sealed in evacuated thin-wall plastic tubing for cold isostatic pressing under 414-MPa pressure.

```
                    ┌──────────────────────┐
                    │ 100-g mill charges   │
                    │ (Si₃N₄, 20-μm sieved │
                    │ SiO₂ and Y₂O₃)       │
                    └──────────┬───────────┘
                               │
  ┌──────────────┐      ┌──────▼───────┐      ┌──────────────┐
  │ SiC/RBSN mill,│─────▶│  Grinding    │◀─────│   Ethanol    │
  │ hot-pressed   │      │  (100 hr)    │      │              │
  │ Si₃N₄ media   │      └──────┬───────┘      └──────────────┘
  └──────────────┘             │
                    ┌──────────▼───────────┐
                    │ Slurry batches       │
                    │ (100-g solids)       │
                    └──────────┬───────────┘
                               │
                    ┌──────────▼───────────┐
                    │ Slurry batches       │
                    │ blended and          │
                    │ 10 μm sieved         │
                    └──────────┬───────────┘
                               │
                    ┌──────────▼───────────┐
                    │ Slurry adjustments   │
                    │ (100-hr grind)       │
                    └──────────┬───────────┘
                               │
                    ┌──────────▼───────────┐
                    │ Slurry press disks   │
                    └──────────┬───────────┘
                               │
                    ┌──────────▼───────────┐
                    │ Isostatic press      │
                    └──────────────────────┘
```
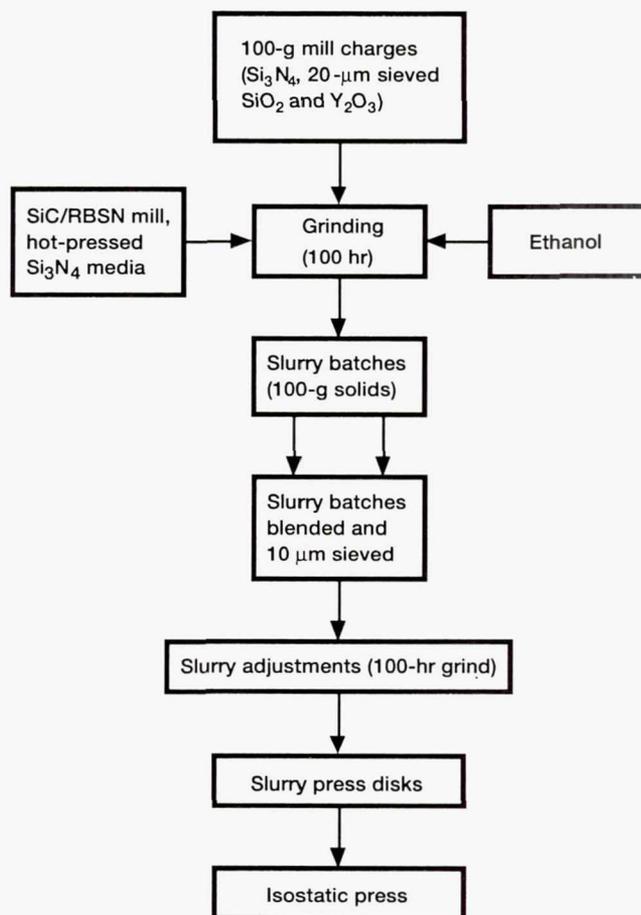
Figure A.1.—Processing of Si$_3$N$_4$-SiO$_2$-Y$_2$O$_3$ slurry. Modified from Sanders et al. (1989).

TABLE A.1 – CHARACTERIZATION OF SILICON NITRIDE, SILICON OXIDE, YTTRIUM OXIDE, AND SLURRY
[From Sanders et al. (1989).]

Material	Source	Manufacturer's designation	Purity, percent	Specific surface area, m^2/g	X-ray diffraction analysis, percent			Chemical analysis, wt%		Spectrographic analysis, ppm
					α	β	Free Si	Oxygen	Carbon	
Si_3N_4	Advanced Materials Engineering, Ltd.	High purity	99.5	3.72	82.9	16.4	0.7	0.71	0.08	930 Al, 110 Ca, 1900 Fe, 500 Mo, 220 Ni, 210 Pb, 170 Ti, 470V
SiO_2	Apache Chemical	6846	99.99	166	-----	-----	-----	-----	.16	220 Al, 150 Ca, 30 Cr, 50 Cu, 50 Fe, 130 Mg, 90 Mn, 340 Na, 40 Ti
Y_2O_3	Molycorp	5600	99.9	7.5	-----	-----	-----	-----	.11	60 Cu, 60 Mg, 40 rare earth oxides
Slurry[a] (100-hr grind)	------------------------	------	--------	25.1	-----	-----	-----	4.76	.11	1240 Al, 90 Ca, 1970 Fe, 510 Mo, 450 Ni, 120 Ti, 290 V, 5.5 wt % Y
Slurry (300-hr grind)	------------------------	------	--------	22.6	-----	-----	-----	-----	------	------------------------------

[a]Ground slurry composition, 87.8 Si_3N_4-5.8SiO_2-6.4Y_2O_3, by weight percent; 83.4 Si_3N_4-12.8SiO_2-3.8Y_2O_3, by mole percent.

Appendix B

Sintering of Nitrides

Sintering is technically the densification of a green ceramic compact. During sintering the volume of pores is reduced by the growth of adjacent particles, grain size and shape changes occur, and pore size and shape are modified. Detailed information on ceramic sintering mechanisms can be found in Kingery et al. (1976).

The isostatically pressed nitride disks were sintered in a tungsten cup inside a water-cooled, double-wall furnace. Sintering temperatures were monitored and controlled with tungsten-5 percent rhenium/tungsten-26 percent rhenium thermocouples. Disks were sintered at 2140 °C for 3 hr. Heating from room temperature to 2140 °C was done at a linear rate lasting 45 min. A nitrogen overpressure of 5 MPa was used.

Page intentionally left blank

Appendix C

Fabrication of Injection-Molded, Sintered Silicon Nitride Blade

Ceramic powder

Organic binder

Rheometer compounding unit

Deairing and pelletizing

Injection molding

Thermal binder removal
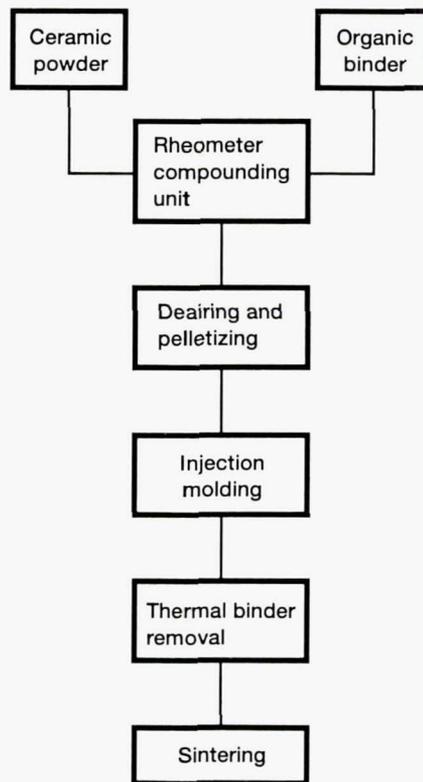
Sintering

Figure C.1.—Fabrication of injection-molded sintered silicon nitride turbine blade. From CATE (1981).

Page intentionally left blank

Appendix D

Fabrication of SCS–6-Fiber-Reinforced MMC Rod, Ring, and Rotor

The MMC rod, ring, and rotor are Pratt & Whitney hardware. Their fabrication procedures are schematically represented in figures D.1 to D.3.

Bundle
of ribbon-
wrapped
fibers

Inserted
into
alloy C
tube

Machined
into
rod

Capped and
HIP consolidated
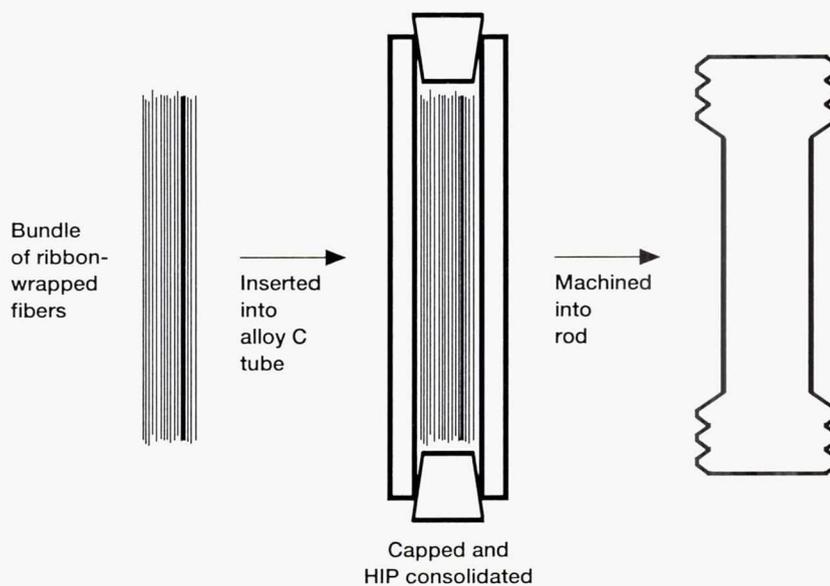
Figure D.1.—Fabrication of fiber-reinforced MMC rod.
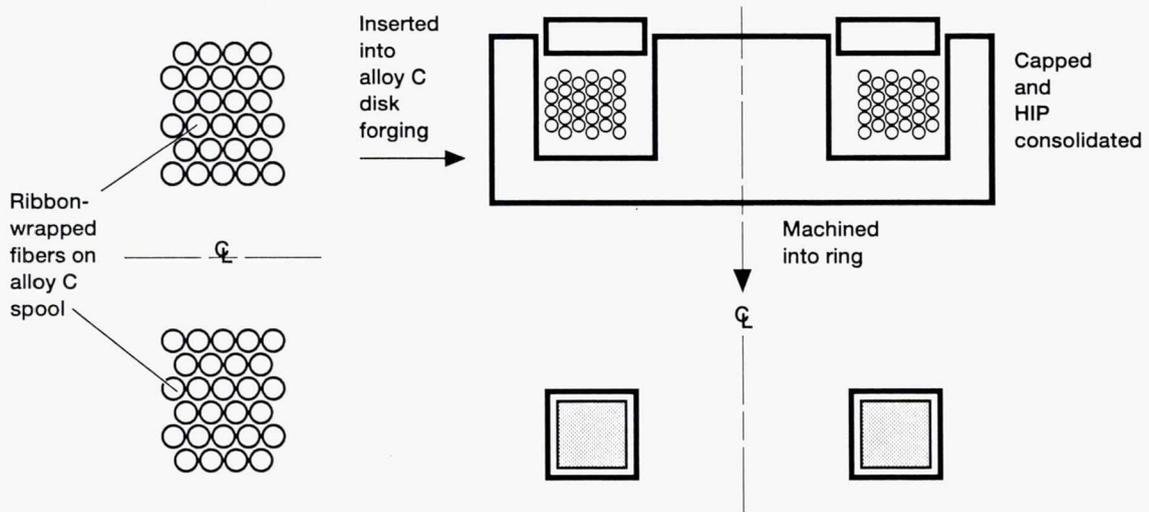
Figure D.2.—Fabrication of fiber-reinforced MMC ring.
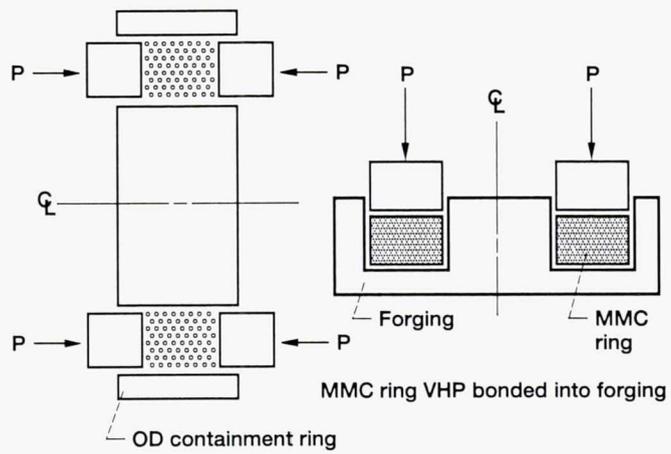
Figure D.3.—Fabrication of integrally bladed MMC rotor.

Appendix E

X-Ray-Radiography-Related Topics

Table E.1 shows the electromagnetic spectrum. Table E.2 lists the computed total mass attenuation coefficients for Si_3N_4, SiC, and Ti_3Al. Table E.3 lists the total mass attenuation coefficients for tungsten, Si_3N_4, SiC, and air.

TABLE E.1. – ELECTROMAGNETIC SPECTRUM
[From Kemp and Oliver (1970).]

Radiation type	Wavelength	Frequency (cycles per sec)
Long- and medium-wave radio	30 000–100 m	10^4–3×10^6
Short-wave radio	100–1 m	3×10^6–3×10^8
Radar and microwave radio	1 m–1 mm or less	3×10^8–3×10^{11}
Infrared (heat) radiation	100 μm–8000 Å	3×10^{12}–3.75×10^{14}
Visible light	8000–4000 Å	3.75×10^{14}–7.5×10^{14}
Ultraviolet radiation	4000–1000 Å	7.5×10^{14}–3×10^{15}
Grenz rays (very-long-wavelength x rays)	10–0.5 Å	3×10^{17}–6×10^{18}
Superficial (and diagnostic) x rays	0.5–0.1 Å	6×10^{18}–3×10^{19}
Deep-therapy x rays	0.1–0.03 Å (100–30 X units)	3×10^{19}–10^{20}
Gamma rays	0.1–0.006 Å (100–6 X units)	3×10^{19}–5×10^{20}
Megavoltage x rays	0.03–0.0001 Å (300–0.1 X units)	10^{20}–3×10^{22}
Some cosmic rays	Down to about 0.2 X units	Up to about 15×10^{22}

TABLE E.2. – COMPUTED TOTAL MASS ATTENUATION COEFFICIENTS
FOR Si_3N_4, SiC, AND Ti_3Al

$[(\mu/\rho)_{SiC} = 0.7005 \, (\mu/\rho)_{Si} + 0.2996 \, (\mu/\rho)_C; \, (\mu/\rho)_{Si_3N_4} = 0.6006 \, (\mu/\rho)_{Si} + 0.3994 \, (\mu/\rho)_N;$
$(\mu/\rho)_{Ti_3Al} = 0.8419 \, (\mu/\rho)_{Ti} + 0.1581 \, (\mu/\rho)_{Al}.]$

Voltage, keV	Si^a	C^a	N^a	Ti^a	Al^a	SiC	Si_3N_4	Ti_3Al
	Total mass attenuation coefficient, cm^2/g							
10	33.3900	2.2980	3.7790	109.500	25.8200	24.0764	21.5640	96.2718
15	10.1900	.7869	1.2070	35.510	7.8360	7.3733	6.6024	31.1352
20	4.4040	.4340	.6063	15.700	3.2920	3.2148	2.8872	13.7543
30	1.4190	.2541	3.3035	4.926	1.1150	1.0700	.9735	4.3236
40	.6943	.2069	.2276	2.195	.5630	.5483	.5079	1.9370
50	.4351	.1867	.1974	1.204	.3655	.3607	.3401	1.0715
60	.3188	.1751	.1814	.761	.2763	.2758	.2639	.6842
80	.2220	.1609	.1638	.403	.2012	.2037	.1987	.3711
100	.1832	.1513	.1529	.271	.1701	.1736	.1711	.2551
150	.1447	.1347	.1353	.165	.1378	.1417	.1409	.1604
200	.1275	.1229	.1233	.131	.1223	.1261	.1258	.1298
300	.1082	.1066	.1068	.104	.1042	.1077	.1077	.1042
400	.0961	.0955	.0956	.091	.0928	.0959	.0959	.0911
500	.0875	.0871	.0872	.082	.0845	.0874	.0873	.0823

[a]Hubbell (1982).

TABLE E.3. – TOTAL MASS ATTENUATION
COEFFICIENTS FOR TUNGSTEN
Si_3N_4, SiC, AND AIR

Voltage, keV	Air^a	W^a	Si_3N_4	SiC
	Total mass attenuation coefficients, cm^2/g.			
10	5.01600	969.200	21.5640	24.0764
15	1.58100	138.900	6.6024	7.3733
20	.76430	65.730	2.8872	3.2148
30	.35010	22.730	.9735	1.0700
40	.24710	10.670	.5079	.5483
50	.20730	5.949	.3401	.3607
60	.18710	3.712	.2639	.2758
80	.16610	7.809	.1987	.2037
100	.15410	4.438	.1711	.1736
150	.13560	1.581	.1409	.1417
200	.12340	.784	.1258	.1261
300	.10680	.324	.1077	.1077
400	.09548	.193	.0959	.0959
500	.08712	.138	.0873	.0874

[a]Hubbell (1982).

Appendix F
Symbols

A	atomic weight	I	x-ray tube current
A_s	sampling area	K	proportionality constant
a	source-to-object distance	M	magnification
b	object-to-detector distance	N	number of transmitted photons
C	radiographic image contrast	N_A	Avogadro's number
C_{res}	resultant radiographic contrast	N_{eff}	effective number of photons
C_{sub}	subject radiographic contrast	N_p	number of primary photons
c	velocity of light	N_s	number of scattered photons
D	thickness of defect (fig. 2.1)	N_0	number of incident photons
D_f	diameter of fiber	n	number of atoms per cubic centimeter; quantum efficiency of detector or screen
DQE	detection quantum efficiency		
E	modulus	R	geometric resolution
E_e	energy of electromagnetic field	R_f	Rayleigh scattering photon deflected in forward direction
E_{max}	maximum tube energy	r	coefficient of correlation
E_{pc}	primary modulus of composite	S	focal spot size
$E_{(rom)c}$	rule-of-mixtures composite modulus	SNR	signal-to-noise ratio
e	charge on electron	SNR_{id}	ideal SNR
f_e	frequency of electromagnetic field	SPR	ratio of scattered radiation to primary radiation
G	film gradient	s	total cross-section atomic attenuation coefficient
h	Planck's constant	T	total attenuation (fig. 2.4); sample thickness (fig. 2.1)

U	geometric unsharpness	μ_2	total attenuation coefficient of defect
V	x-ray tube voltage	μ/ρ	total mass attenuation coefficient
W_i	proportion by weight of ith constituent	$(\mu/\rho)_c$	total mass attenuation coefficient of compound
X	crack spacing	ρ	material density
ΔX	dimension of defect in direction of x-ray beam	σ	stress
$\bar{X}$	mean crack spacing	σ_c^m	composite stress at first matrix cracking
X_m	matrix spacing	$\sigma(x)$	quantum noise
x	material thickness	τ_f	interfacial shear stress
Z	atomic number	ψ	energy flux density
ε	axial strain	Subscripts:	
λ	x-ray wavelength	f	fiber
μ	total linear attenuation coefficient	m	matrix
μ_1	total attenuation coefficient of matrix	min	minimum

Appendix G
Glossary

ACK   Aveston, Cooper, Kelly

A/D   analog to digital

AGT   Advanced Gas Turbine Technology Project

ASDR   area-scan digital radiography

ASTM   American Society for Testing and Materials

ATTAP   Advanced Turbine Technology Applications Project

BSE   backscattered electron

CATE   Ceramic Application in Turbine Engines

CMC   ceramic matrix composite

CT   computed tomography

CTE   coefficient of thermal expansion

EDAX   energy-dispersive analysis x ray

GPIB   general-purpose interface bus

HIP   hot isostatic pressing

HITEMP   NASA High Temperature Materials Program

IMC   intermetallic matrix composite

IXMTS   in situ x-ray and materials testing system

LAM/DE   laminography/dual energy

LSDR   line-scan digital radiography

MMC   metal matrix composite

MOR   modulus of rupture

NDE   nondestructive evaluation

PC   personal computer

PSDR   point-scan digital radiography

RBSN   reaction-bonded silicon nitride

SAM   scanning acoustic microscopy

SC   silicon carbide

SCS–6   silicon nitride

VHP   vacuum hot press

XCT   x-ray computed tomography

$[0]_1$ one-ply unidirectional composite

$[0]_3$ three-ply unidirectional composite

$[0]_5$ five-ply unidirectional composite

$[0]_8$ eight-ply unidirectional composite

Page intentionally left blank

References

Ackerman, J.L., et al., 1987, "The Use of NMR Imaging to Measure Porosity and Binder Distributions in Green-State and Partially Sintered Ceramics," *Nondestructive Testing of High Performance Ceramics*, A. Vary, and J. Snyder, eds., American Ceramics Society, Westerville, OH, pp. 88–113.

"Advanced Turbine Technology Applications Project (ATTAP)," 1990, NASA CR–185240.

Agarwal, B.D., and Broutman, L.J., 1979, *Analysis and Performance of Fiber Composites*, John Wiley & Sons, New York, Chapter 2.

"AGT (Advanced Gas Turbine) Technology Project," 1988, NASA CR–182127.

Armistead, R.A., 1988, "CT: Quantitative 3–D Inspection," *Advanced Materials & Processes*, Vol. 133, No. 3, pp. 42–43, 46–48.

Arnold, B.A., et al., 1981, "Digital Radiography: An Overview," *Application of Optical Instrumentation in Medicine X, SPIE Proceedings*, Vol. 273, J.E. Gray, et al., eds., SPIE, Billingham, WA, pp. 215–226.

Arnold, B.A., 1982, "Digital Radiography: A Technology Overview," *Application of Optical Instrumentation in Medicine X, SPIE Proceedings*, Vol. 347, G.D. Fullerton, et al., eds., SPIE, Billingham, WA, pp. 347.

Aveston, J., Cooper, G.A., and Kelly, A., 1971, "Single and Multiple Fracture," *The Properties of Fibre Composites*, IPC Science and Technology Press Ltd., Surrey, England, pp. 15–26.

Azevedo, S.G., 1988, "Model Based Computed Tomography for Nondestructive Evaluation; An Overview and Proposal," UCID–21380, Lawrence Livermore National Laboratory, CA.

Baaklini, G.Y., and Roth D.J., 1986a, "Probability of Detection of Internal Voids in Structural Ceramics Using Microfocus Radiography," *Journal of Material Research*, Vol. 1, No. 3, pp. 457–467.

Baaklini, G.Y, Kiser, J.D., and Roth, D.J., 1986b, "Radiographic Detectability Limits for Seeded Voids in Sintered Silicon Carbide and Silicon Nitride," *Advanced Ceramic Materials*, Vol. 1, No. 1, pp. 43–49.

Baaklini, G.Y., 1987, "NDE Reliability and Process Control for Structural Ceramics," *Journal of Engineering for Gas Turbines and Power*, Vol. 109, No. 3, pp. 263–266.

Baaklini, G.Y., Generazio, E.R., and Kiser, J.D., 1989, "High Frequency Ultrasonic Characterization of Sintered Silicon Carbide," *Journal of the American Ceramics Society*, Vol. 72, No. 3, pp. 383–387.

Bellian, J.G., and Dayton, R.R., 1974, "NaI(Tl) Scintillation Detectors," BICRON Corp.

Berland L.L., 1987, "Practical CT: Technology and Techniques," Raven Press Books, New York.

Bhatt, R.T., 1985, "Mechanical Properties of SiC Fiber-Reinforced Reaction-Bonded Si_3N_4 Composites," NASA TM–87085.

Bhatt, R.T., 1987, "Method of Preparing Fiber-Reinforced Ceramic Materials," U.S. Patent No. 4,689,188.

Bhatt, R.T., and Phillips, R.E., 1988a, "Laminate Behavior for SiC Fiber-Reinforced Reaction-Bonded Silicon Nitride Matrix Composites," NASA TM–101350.

Bhatt, R.T., 1988b, "The Properties of Silicon Carbide Fiber-Reinforced Silicon Nitride Composites," *Whisker- and Fiber-Toughened Ceramics*, R.A. Bradly, et al., eds., ASM International, Metals Park, OH, pp. 199–208.

Bhatt, R.T., 1990, "Influence of Interfacial Shear Strength on the Mechanical Properties of SiC Fiber Reinforced Reaction-Bonded Silicon Nitride Matrix Composites," NASA TM–102462.

Birks, A.S., Green, R.E., Jr., and McIntire, P., eds., 1991, *Nondestructive Testing Handbook*, Vol. 7: *Ultrasonic Testing*, American Society for Nondestructive Testing, Inc., Columbus, OH, pp. 258–266.

Bowman, C.C., and Batchelor, B.G., 1985, "Automated Visual Inspection," *Research Techniques in Nondestructive Testing*, Vol. 8, R.S. Sharpe, ed., Academic Press, New York, pp. 361–444.

Byrd, J.A, Janovicz, M.A., and Thrasher, S.R., 1981, "CATE, Ceramic Applications in Turbine Engines," NASA CR–165994.

Cappellini, V., Constantinides, A.G., and Emiliani, P., 1978, *Digital Filters and Their Applications*, Academic Press, New York.

Cappellini, V., and Constantinides, A.G., eds., 1980, *Digital Signal Processing*, Academic Press, New York.

Cormack, A.M., 1963, "Representation of a Function by Its Line of Integrals, With Some Radiological Applications," *Journal of Applied Physics*, Vol. 34, No. 9, pp. 2722–2727.

Cormack, A.M., 1964, "Representation of a Function by Its Line Integrals, With Some Radiological Applications. II," *Journal of Applied Physics*, Vol. 35, No. 10, pp. 2908–2913.

Eldridge, J.I., Bhatt, R.T., and Kiser, J.D., 1991, "Investigation of Interfacial Shear Strength in SiC/Si_3N_4 Composites," NASA TM–103739.

Ellingson, W.A., et al., 1987a, "Characterization of Porosity in Green-State and Partially Densified Al_2O_3 by Nuclear Magnetic Resonance Imaging," *Ceramic Engineering Science Proceedings*, Vol. 8, pp. 503–512.

Ellingson, W.A., Hentea, T., and Kriz, R.J., 1987b, "Inspection of Advanced Ceramics With a Conventional Film-Based Tomography System: Preliminary Results," *Nondestructive Testing of High Performance Ceramics*, A. Vary, and J. Snyder, eds., American Ceramics Society, Westerville, OH, pp. 132–147.

Ellingson, W.A., and Vannier, M.W., 1988, "X-ray Computed Tomography for Nondestructive Evaluation of Advanced Structural Ceramics," ANL–87–52, Argonne National Laboratory, IL.

Ellingson, W.A., et al., 1989, "Magnetic Resonance Imaging: A New Characterization Technique for Advanced Ceramics," *American Ceramic Society Bulletin*, Vol. 68, pp. 1180–1186.

Evans, A.G., et al., 1977, "Failure Prediction in Structural Ceramics," *Materials Evaluation*, Vol. 35, No. 4, pp. 85–96.

Evans, A.G., 1984, "Aspects of the Reliability of Ceramics," *Defect Properties and Processing of High Technology Nonmetallic Materials*, J.H. Crawford, et al., eds., North-Holland, New York, pp. 63–80.

Evans, A.G., and Marshall, D.B., 1989, "The Mechanical Behavior of Ceramic Matrix Composites," *Acta Metallurgica*. Vol. 37, No. 10, pp. 2567–2583.

Feldkamp, L.A., and Jesion, G., 1986, "3-D X-Ray Computed Tomography," *Review of Progress in Quantitative Nondestructive Evaluation*, Vol. 5A, D.O. Thompson and D.E. Chimenti, eds., Plenum Press, New York, pp. 555–566.

Freedman, M.R., and Millard,M.L., 1986, "Improved Consolidation of Silicon Carbide," NASA TM–87243.

Friedman, W.D., et al., 1987, "Characterization of Green Ceramics With X-ray Tomography and Ultrasonics, *Nondestructive Testing of High Performance Ceramics*, A. Vary and J. Snyder, eds., American Ceramics Society, Westerville, OH, pp. 128–131.

Gardner, R.P., and Ely, R.L., Jr., 1967, *Radioisotope Measurement Applications in Engineering*, Reinhold Publishing Corp., New York.

Generazio, E.R., 1985, "The Role of the Reflection Coefficient in Precision Measurement of Ultrasonic Attenuation," *Materials Evaluation*, Vol. 43, No. 7, pp. 995–1004.

Generazio, E.R., Roth, D.J., and Baaklini, G.Y., 1988, "Acoustic Imaging of Subtle Porosity Variations in Ceramics," *Materials Evaluation*, Vol. 46, No. 10, pp. 1338–1343.

Goebbels, K., 1980, "Structure Analysis by Scattered Ultrasonic Radiation," *Research Techniques in Nondestructive Testing*, Vol. 4, R.S., Sharpe, ed., Academic Press, New York, pp. 87–157.

Gonzalez, R.C., and Wintz, P., 1977, *Digital Image Processing*, Addison-Wesley Publishing Co., Reading, MA.

Gopalsami, N., et al., 1990, "Nuclear Magnetic Resonance Imaging of Green State Ceramics," ANL–90/27, Argonne National Laboratory, IL.

Halmshaw, R., 1982, *Industrial Radiology: Theory and Practice*, Applied Science Publishers, Englewood, NJ.

Harper, J.E., 1983, "ARPA/NAVAIR Ceramic Gas Turbine Engine Demonstration Program," *Ceramics for High Performance Applications III: Reliability*, E.M. Lenoe, R.N. Katz, and J.J. Burke, eds., Plenum, Press, New York, pp. 645–664.

Helms, H.E., et al., "CATE, Ceramic Applications in Turbine Engines," NASA CR–174715.

Hemann, J.H., and Baaklini, G.Y., 1986, "Effect of Stress on Ultrasonic Pulses in Fiber Reinforced Composites," *SAMPE Journal*, Vol. 22, No. 4, pp. 9–13.

Heraud, L., and Spriet, P., 1988, "High Toughness C-SiC and SiC-SiC Composites in Heat Engines," *Whisker- and Fiber-Toughened Ceramics*, R.A. Bradly, ed., ASM International, Metals Park, OH, pp. 217–224.

Herman, G.T., 1981, "Principles of Reconstruction Algorithms, Section II: Advanced Principles of Reconstruction Algorithms," *Radiology of the Skull and Brain: Technical Aspects of Computed Tomography*, Vol. 5, T.H. Newton and D.G. Potts, eds., The C.V. Mosby Co., St. Louis, MO, pp. 3888–3917.

Hounsfield, G.N., 1973, "Computerized Transverse Axial Scanning (Tomography). I. Description of System," *British Journal of Radiology*, Vol. 46, No. 552, pp. 1016–1022.

Hubbell, J.H., 1969, "Photon Cross-Sections, Attenuation Coefficients, and Mass Energy Absorption Coefficients From 10 keV to 100 GeV," NSRDS–NBS 29, National Bureau of Standards.

Hubbell, J.H., 1982, "Photon Mass Attenuation and Mass Energy-Absorption Coefficients from 1 keV to 20 MeV," *International Journal of Applied Radiation and Isotopes*, Vol. 33, No. 11, pp.1269–1290.

Iwasaki, H., and Isumi, M., 1981, "Acoustic Characterization of Si_3N_4 Ceramics," *Journal of Society of Materials Science, Japan*, Vol. 30, No. 337, pp. 1044–1050.

Joseph, P.M., 1981, "Artifacts in Computed Tomography," *Radiography of the Scull and Brain: Technical Aspects of Computed Tomography*, Vol. 5, T.H. Newton, and D.G. Potts, eds., The C.V. Mosby Co., St. Louis, MO, pp. 3956–3992.

Kak, A.C., and Slaney, M., 1988, *Principles of Computerized Tomographic Imaging*, IEEE, New York.

Kautz, H.E., and Bhatt, R.T., 1991, "Ultrasonic Velocity Technique for Monitoring Property Changes in Fiber-Reinforced Ceramic Matrix Composites," *Ceramic Engineering and Science Proceedings*, Vol. 12, No. 7–8, pp. 1139–1151.

Kautz, H.E., and Lerch, B.A., 1991, "Preliminary Investigation of Acousto-Ultrasonic Evaluation of Metal-Matrix Composite Specimens," *Materials Evaluation*, Vol. 49, No. 5, pp. 607–612.

Kemp, L.A.W., and Oliver, R., 1970, *Basic Physics in Radiology*, Second Edition, Blackwell Scientific Publications, Oxford, England, pp. 215–232.

Kerans, R.J., et al., 1989, "The Role of the Fiber-Matrix Interface in Ceramic Composites," *American Ceramic Society Bulletin*, Vol. 68, No. 2, pp. 429–442.

Kereiakes, J.G., Thomas, S.R., and Ortron, C.G., eds., 1986, *Digital Radiography Selected Topics*. Plenum Press, New York.

Kessler, L.W., and Yuhas, D.E., 1978, "High Resolution Real Time Acoustic Microscopy," *Proceedings of the ARPA/AFML Review of Progress in Quantitative Nondestructive Evaluation*, D.O. Thompson, ed., AFML–TR–78–55, pp. 241–244.

Khandelwal, P.K., 1987, "Detection of Failure Controlling Flaws by Photoacoustic Microscopy (PAM) in Silicon Nitride," *Nondestructive Testing of High Performance Ceramics*, A. Vary and J. Snyder, eds., American Ceramics Society, Westerville, OH, pp. 183–197.

Khuri-Yakub, B.T., Kino, G.S., and Evans, A.G., 1980, "Acoustic Surface Wave Measurements of Surface Cracks in Ceramics," *Journal of American Ceramics Society*, Vol. 63, No. 1–2, pp. 65–71.

Khuri-Yakub, B.T., et al., 1982, "Nondestructive Evaluation of Ceramics," *Review of Progress in Quantitative Nondestructive Evaluation*, Vol. 1, D.O. Thompson and D.E. Chimenti, eds., Plenum Press, New York, pp. 601–606.

Khuri-Yakub, B.T., et al., 1985, "Nondestructive Evaluation of Composite Materials Using Acoustic Microscopy," *Review of Progress in Quantitative Nondestructive Evaluation*, Vol. 5B., D.O.Thompson and D.E. Chimenti, eds., Plenum Press, New York, pp. 1093–1098.

Kingery, W.D., Bowen, H.K., and Uhlmann, D.R., 1976, *Introduction to Ceramics*, Second Edition, John Wiley & Sons, New York.

Kinney, J.H., et al., 1990, "Nondestructive Imaging of Materials Microstructures Using X-ray Tomographic Microscopy," *Advanced Tomographic Imaging Methods for the Analysis of Materials, MRS Symposium Proceedings*, Vol. 217, J.L. Ackerman and W.A. Ellingson, eds., Materials Research Society, pp. 81–95.

Kinney, J.H., et al., 1991, "X-ray Tomographic Microscopy for Nondestructive Characterization of Composites," *Review of Progress in Quantitative Nondestructive Evaluation*, Vol. 10A, D.O.Thompson and D.E. Chimenti, eds., Plenum Press, New York, pp. 427–433.

Klima, S.J., Baaklini, G.Y., and Abel, P.B., 1986, "Nondestructive Evaluation of Structural Ceramics," NASA TM–88978.

Klima, S.J., et al., 1981, "Ultrasonic Velocity for Estimating Density of Structural Ceramics," NASA TM–82765.

Kress, J.W., and Feldkamp, L.A., 1983, "X-ray Tomography Applied to NDE of Ceramics," ASME Paper 83–GT–206.

Kropas, C.V., Moran, T.J., and Yancey, R.N., 1991, "Effect of Composition on Density Measurement by X-ray Computed Tomography," *Materials Evaluation*, Vol. 49, No. 4, pp. 487–490.

Lemons, P., and Quate, C., 1979, "The Acoustic Microscope," *Physical Acoustics: Principles and Methods*, Vol. XIV, W. Mason, ed., Academic Press, New York, pp. 1–92.

London, B., Yancey, R.N., and Smith, J.A., 1990, "High-Resolution X-ray Computed Tomography of Composite Materials," *Materials Evaluation*, Vol. 48, No. 5, pp. 604–608, 628.

Macovsky, A., 1983, *Medical Imaging Systems*, Prentice-Hall, Inc., Englewood Cliffs, NJ.

Mah, T., et al., 1987, "Recent Developments in Fiber-Reinforced High-Temperature Ceramic Composites," *American Ceramic Society Bulletin*, Vol. 66, No. 2, pp. 304–308, 317.

McCauley, J.W., 1987, "Materials Testing in the 21st Century," *Nondestructive Testing of High-Performance Ceramics*, A. Vary and J. Snyder, eds., American Ceramic Society, Westerville, OH, pp.1–18.

Newton, T.H., and Potts, D.G., eds., 1987, *Radiology of the Skull and Brain: Technical Espects of Computed Tomography*, Vol. 5, The C.V. Mosby Co., St. Louis, MO, 1987.

Nikoonahad, M., 1987, "Reflection Acoustic Microscopy for Industrial NDE," *Research Techniques in Nondestructive Testing*, Vol. 7, R.S. Sharpe, ed., Academic Press, London, England, pp. 217–257.

Nishida, K., 1983, "Silicon Nitride: The Development of Structural Fine Ceramics in Japan," *Japan Industrials and Technological Bulletin*, Vol. 11, pp. 21–24.

Nondestructive Testing Handbook, 1985, Vol. 3, *Radiography and Radiation Testing*, American Society for Nondestructive Testing, pp. 836–878.

Oppenheim, A.V., and Schafer, R.W., 1975, *Digital Signal Processing*, Prentice-Hall, Inc., Englewood Cliffs, NJ.

Parish, R.W, 1979, "High Resolution Radiography in the Aero-Engine Industry," *Nondestructive Inspection Methods for Propulsion Systems and Components*, Report AGARD–LS–L03, Advisory Group for Aerospace Research and Development, Neuilly-sur-Seine, France, 38 p. (Available NTIS AD–A069901.)

Pfeiler, M., Marhoff, P., and Koch, R., 1985, "Effects of X-Ray Physics and Technology in Digital Radiography" *Electromedica*, Vol. 53, No. 2, pp. 50–67.

Pratt, W.K., 1978, *Digital Image Processing*, John Wiley & Sons, New York.

Pullan, B.R., Ritchings, R.T., and Isherwood, I., 1981, "High-Resolution X-ray Computed Tomography Attenuation Values," *Radiography of the Skull and Brain: Technical Aspects of Computed Tomography*, Vol. 5, T.H. Newton and D.G. Potts, eds., The C.V. Mosby Co., St. Louis, MO, pp. 3904–3917.

Radiological Health Handbook, 1970, Bureau of Radiological Health and the Training Institute, Environmental Control Administration, U.S. Government Printing Office, Washington, DC.

Radon, J., 1917, "On the Determination of Functions From Their Integrals Along Certain Manifolds," *Mathematik fuer Physiker*, Vol. 69, pp. 262–267.

Rice, R.W., Freiman, S.W., and Mecholsky, J.J., Jr., 1977, "Fractography of Si_3N_4 and SiC," *Ceramics for High Performance Applications II*, J.J. Burke, E.N. Lenoe, and R.N. Katz, eds., Brook Hill Publishing, Chestnut Hill, MA, pp. 669–687.

Richerson, D.W., 1982, *Modern Ceramic Engineering: Properties, Processing, and Use in Design*, Marcel Dekker Inc., New York.

Riederer, S.J., 1985, "Digital Radiography," *CRC Critical Reviews in Bioengineering*, Vol. 12, No. 2, pp.163–200.

Rosencwaig, A., 1982, "Thermal Wave Imaging," *Science*, Vol. 218, No. 4569, pp. 223–228.

Roth, D.J., et al., 1986, "Reliability of Void Detection in Structural Ceramics by Use of Scanning Laser Acoustic Microscopy," *Materials Evaluation*, Vol. 44, No. 6, pp. 761–769.

Roth, D.J., Generazio, E.R., and Baaklini, G.Y., 1987, "Quantitative Void Characterization in Structural Ceramics by Use of Scanning Laser Acoustic Microscopy," *Materials Evaluation*, Vol. 45, No. 9, pp. 958–966.

Rzeszotarski, M., and Sones, R., 1989, Class Notes in '*Fundamentals of Medical Imaging*', EBME 410, Case Western University, Cleveland, OH.

Sanders, W.A., and Baaklini, G.Y., 1988, "Correlation of Processing and Sintering Variables With the Strength and Radiography of Silicon Nitride," *Advanced Ceramic Materials*, Vol. 3, No. 1, pp. 88–94.

Sanders, W.A., Kiser, J.D., and Freedman, M.R., 1989, "Slurry-Pressing Consolidation of Silicon Nitride," *American Ceramic Society Bulletin*, Vol. 68, No. 10, pp. 1836–1841.

Sawicka, B.D., and Palmer, B.J.F., 1986, "Density Gradients in Ceramic Pellets Measured by Computed Tomography," Report AECL–9261, Chalk River Nuclear Laboratories, Chalk River, Ontario, Canada.

Sawicka, B.D., and Ellingson, W.A., 1987, "Photon CT Scanning of Advanced Ceramic Materials," Report AECL–9384, Chalk River Nuclear Laboratories, Chalk River, Ontario, Canada.

Simon, J.C., Haralick, R.M., and Reidel, D., 1980, *Digital Image Processing*, Klumer Publishing Co., Boston, MA.

Singh, J.P., 1988, "Effect of Flaws on the Fracture Behavior of Structural Ceramics: A Review," *Advanced Ceramic Matererials*, Vol. 3, No. 1, pp. 18–27.

Smathers, R.L., and Brody, W.R., 1985, "Digital Radiography: Current and Future Trends," *British Journal of Radiology*, Vol. 58, No. 688, pp. 285–307.

"Structural Ceramics," 1986, NASA CP–2427.

Tapiovaara, M.J., and Wagner, R.F., 1985, "SNR and DQE Analysis of Broad Spectrum X-ray Imaging," *Physics in Medicine and Biology*, Vol. 30, No. 6, pp. 519–529.

Tittmann, B.R., et al., 1980, "Surface Wave Scattering From Elliptical Cracks for Failure Prediction," *Journal of Applied Physics*, Vol. 51, No. 1, pp. 142–150.

Vary, A., 1978, "Correlations Among Ultrasonic Propagation Factors and Fracture Toughness Properties of Metallic Materials," *Materials Evaluation*, Vol. 36, No. 7, pp. 55–64.

Vary, A., 1988, "Concepts for Interralating Ultrasonic Attenuation, Microstructure, and Fracture Toughness in Polycrystalline Solids," *Materials Evaluation*, Vol. 46, No. 5, pp. 642–649.

Vary, A., 1991, "NDE Standards for High-Temperature Materials," NASA TM–103761.

Vary, A., and Klima, S.J., 1991, "NDE of Ceramics and Ceramic Composites," NASA TM–104520.

Yancey, R.N., Klima, S.J., and Smith, J.A., 1990, "High Resolution Computed Tomography of Modern Ceramics," *Proceedings of the Topical Conference on Nondestructive Evaluation of Modern Ceramics*, American Ceramic Society, Columbus, OH, pp. 126–130.

Yancey, R.N., Baaklini, G.Y., and Klima, S.J., 1991, "NDE of Advanced Turbine Engine Components and Materials by Computed Tomography," ASME Paper 91–GT–287.

Yuhas, D.E., McGraw, T.E., and Kessler, L.W., 1979, "Scanning Laser Acoustic Microscope Visualization of Solid Inclusions in Silicon Nitride," *Proceedings of the DARPA/AFML Review of Progress in Quantitative Nondestructive Evaluation*, D.O. Thompson and R.B. Thompson, eds., AFWAL–TR–80–4078, pp. 683–690.

Zatz, L.M., 1981, "Basic Principles of Computed Tomography Scanning," *Radiology of the Skull and Brain: Technical Aspects of Computed Tomography*, T.H. Newton and D.G. Potts, eds., Vol. 5, The C.V. Mosby Co., St. Louis, MÓ, pp. 3853–3876.

Page intentionally left blank

Bibliography

"Aeropropulsion 1991," 1991, NASA CP-10063.

Andrews, H.C., and Hunt, B.R., 1977, *Digital Image Restoration*, Prentice-Hall, Inc., Englewood Cliffs, NJ.

ASTM Standards, 1991, *Metals Test Methods and Analytical Procedures*, Vol. 3.03: *Nondestructive Testing*, ASTM.

Baaklini, G.Y., and Abel, P.B., 1988, "Radiographic and Ultrasonic Characterizations of Sintered Silicon Carbide," *Materials Evaluation*, Vol. 46, No. 11, pp. 1477–1483.

Bederson, B., and Fite, W.L., eds., 1989, *Atomic and Electron Physics*, Academic Press, New York.

Bendat, J.S., and Piersol, A.G., 1980, *Engineering Applications of Correlation and Spectral Analysis*, John Wiley & Sons, New York.

Berthelot, A., 1958, *Radiations and Matter*, (English translation by F.R. Paulsen), Leonard Hill Limited, London, pp. 150–175.

Hubbell, J.H., 1977, "Photon Mass Attenuation and Mass Energy-Absorption Coefficients for H, C, N, O, Ar, and Seven Mixtures From 0.1 keV to 20 MeV," *Radiation Research*, Vol. 70, No. 1, pp. 58–81.

Johnson, D.R., 1991, "Ceramic Technology for Advanced Heat Engines Project," ORNL/TM-11859, Oak Ridge National Laboratory, TN.

Krestel, E., ed., 1990, *Imaging Systems for Medical Diagnostics*. Siemens Aktiengesellschaft Co., Berlin, Germany.

Lapp, R.E., and Andrews, H.L., 1963, *Nuclear Radiation Physics*, Third Edition Prentice-Hall, Inc., Englewood Cliffs, NJ.

McIntire, P., and Bryant, L.E., eds., 1985, *Nondestructive Testing Handbook*, Vol. 3: Second Edition, *Radiography and Radiation Testing*," American Society for Nondestructive Testing, Columbus, OH.

McIntire, P., Birks, A.S., and Green, R.E., Jr., eds., 1991, *Nondestructive Testing Handbook*, Vol. 7: Second Edition, *Ultrasonic Testing*, American Society for Nondestructive Testing, Columbus, OH, 1991.

Ruud, C.O., and Green, R.E., Jr., 1983, *Nondestructive Methods for Material Property Determination*, Plenum Press, New York.

Shepp, L.A., 1983, *Computed Tomography*, American Mathematical Society, Providence, RI.

Snell, A.H., ed., 1962, *Nuclear Instruments and Their Uses*, Vol. 1, John Wiley & Sons, Inc., New York.

Storm, E., and Israel, H.I., 1970, "Photon Cross Sections From 1 keV to 100 MeV for Elements $Z=1$ to $Z=100$," *Nuclear Data Tables* Sect. A7, pp. 565–681.

Vary, A., and Klima, S.J., 1986, "Nondestructive Techniques for Characterizing Mechanical Properties of Structural Materials—An Overview," ASME Paper 86–GT–75. (Also, NASA TM–87203.)

Page intentionally left blank

Acknowledgments

REPORT DOCUMENTATION PAGE

Public reporting burden for this collection of information is estimated to average 1 hour per response, including the time for reviewing instructions, searching existing data sources, gathering and maintaining the data needed, and completing and reviewing the collection of information. Send comments regarding this burden estimate or any other aspect of this collection of information, including suggestions for reducing this burden, to Washington Headquarters Services, Directorate for Information Operations and Reports, 1215 Jefferson Davis Highway, Suite 1204, Arlington, VA 22202-4302, and to the Office of Management and Budget, Paperwork Reduction Project (0704-0188), Washington, DC 20503.

1. AGENCY USE ONLY (Leave blank)	2. REPORT DATE	3. REPORT TYPE AND DATES COVERED
	October 1993	Technical Paper

4. TITLE AND SUBTITLE

Engine Materials Characterization and Damage Monitoring by Using X-Ray Technologies

5. FUNDING NUMBERS

WU–510–01–50

6. AUTHOR(S)

George Y. Baaklini

7. PERFORMING ORGANIZATION NAME(S) AND ADDRESS(ES)

National Aeronautics and Space Administration
Lewis Research Center
Cleveland, Ohio 44135–3191

8. PERFORMING ORGANIZATION REPORT NUMBER

E–7549

9. SPONSORING/MONITORING AGENCY NAME(S) AND ADDRESS(ES)

National Aeronautics and Space Administration
Washington, D.C. 20546–0001

10. SPONSORING/MONITORING AGENCY REPORT NUMBER

NASA TP–3328

11. SUPPLEMENTARY NOTES

Report is an extended version of NASA TM–105557, with material added in chapter 5 (section 5.3.3). Responsible person, George Y. Baaklini, (216) 433–6016.

12a. DISTRIBUTION/AVAILABILITY STATEMENT

Unclassified - Unlimited
Subject Categories 38 and 24

12b. DISTRIBUTION CODE

13. ABSTRACT (Maximum 200 words)

X-ray attenuation measurement systems that are capable of characterizing density variations in monolithic ceramics and damage due to processing and/or mechanical testing in ceramic and intermetallic matrix composites are developed and applied. Noninvasive monitoring of damage accumulation and failure sequences in ceramic matrix composites is used during room-temperature tensile testing. This work resulted in the development of a point-scan digital radiography system and an in situ x-ray material testing system. The former is used to characterize silicon carbide and silicon nitride specimens, and the latter is used to image the failure behavior of silicon-carbide-fiber-reinforced, reaction-bonded silicon nitride matrix composites. State-of-the-art x-ray computed tomography is investigated to determine its capabilities and limitations in characterizing density variations of subscale engine components (e.g., a silicon carbide rotor, a silicon nitride blade, and a silicon-carbide-fiber-reinforced beta titanium matrix rod, rotor, and ring). Microfocus radiography, conventional radiography, scanning acoustic microscopy, and metallography are used to substantiate the x-ray computed tomography findings. Point-scan digital radiography is a viable technique for characterizing density variations in monolithic ceramic specimens. But it is very limited and time consuming in characterizing ceramic matrix composites. Precise x-ray attenuation measurements, reflecting minute density variations, are achieved by photon counting and by using microcollimators at the source and the detector. X-ray computed tomography is found to be a unique x-ray attenuation measurement technique capable of providing cross-sectional spatial density information in monolithic ceramics and metal matrix composites. X-ray computed tomography is proven to accelerate generic composite component development. Radiographic evaluation before, during, and after loading shows the effect of preexisting volume flaws on the fracture behavior of composites. Results from one-, three-, five-, and eight-ply ceramic composite specimens show that x-ray film radiography can monitor damage accumulation during tensile loading. Matrix cracking, fiber-matrix debonding, fiber bridging, and fiber pullout are imaged throughout the tensile loading of the specimens. In situ film radiography is found to be a practical technique for estimating interfacial shear strength between the silicon carbide fibers and the reaction-bonded silicon nitride matrix. It is concluded that pretest, in situ, and post-test x-ray imaging can provide greater understanding of ceramic matrix composite mechanical behavior.

14. SUBJECT TERMS

X-radiography; NDE; Ultrasonics; X-tomography; In situ monitoring; Damage accumulation; Digital radiography; Composites; Ceramics; CMC; MMC

15. NUMBER OF PAGES

112

16. PRICE CODE

A06

17. SECURITY CLASSIFICATION OF REPORT	18. SECURITY CLASSIFICATION OF THIS PAGE	19. SECURITY CLASSIFICATION OF ABSTRACT	20. LIMITATION OF ABSTRACT
Unclassified	Unclassified	Unclassified	

National Aeronautics and
Space Administration
Code JTT
Washington, D.C.
20546-0001

NASA